UNIVERSITAT POLITÈCNICA
DE CATALUNYA
BARCELONATECH

Computational fluid dynamic (CFD) study of polymer microencapsulation processes

Masooma Qizilbash

ADVERTIMENT La consulta d'aquesta tesi queda condicionada a l'acceptació de les següents condicions d'ús: La difusió d'aquesta tesi per mitjà del repositori institucional UPCommons (http://upcommons.upc.edu/tesis) i el repositori cooperatiu TDX (http://www.tdx.cat/) ha estat autoritzada pels titulars dels drets de propietat intel·lectual **únicament per a usos privats** emmarcats en activitats d'investigació i docència. No s'autoritza la seva reproducció amb finalitats de lucre ni la seva difusió i posada a disposició des d'un lloc aliè al servei UPCommons o TDX. No s'autoritza la presentació del seu contingut en una finestra o marc aliè a UPCommons (*framing*). Aquesta reserva de drets afecta tant al resum de presentació de la tesi com als seus continguts. En la utilització o cita de parts de la tesi és obligat indicar el nom de la persona autora.

ADVERTENCIA La consulta de esta tesis queda condicionada a la aceptación de las siguientes condiciones de uso: La difusión de esta tesis por medio del repositorio institucional UPCommons (http://upcommons.upc.edu/tesis) y el repositorio cooperativo TDR (http://www.tdx.cat/?locale- attribute=es) ha sido autorizada por los titulares de los derechos de propiedad intelectual **únicamente para usos privados enmarcados** en actividades de investigación y docencia. No se autoriza su reproducción con finalidades de lucro ni su difusión y puesta a disposición desde un sitio ajeno al servicio UPCommons No se autoriza la presentación de su contenido en una ventana o marco ajeno a UPCommons (*framing)*. Esta reserva de derechos afecta tanto al resumen de presentación de la tesis como a sus contenidos. En la utilización o cita de partes de la tesis es obligado indicar el nombre de la persona autora.

WARNING On having consulted this thesis you're accepting the following use conditions: Spreading this thesis by the institutional repository UPCommons (http://upcommons.upc.edu/tesis) and the cooperative repository TDX (http://www.tdx.cat/?locale- attribute=en) has been authorized by the titular of the intellectual property rights **only for private uses** placed in investigation and teaching activities. Reproduction with lucrative aims is not authorized neither its spreading nor availability from a site foreign to the UPCommons service. Introducing its content in a window or frame foreign to the UPCommons service is not authorized (framing). These rights affect to the presentation summary of the thesis as well as to its contents. In the using or citation of parts of the thesis it's obliged to indicate the name of the author.

UNIVERSITAT POLITECHNICA DE CATALUNYA
BARCELONA **TECH**
Escola d’Enginyeria de Barcelona Est (EEBE)
Department de Polymers y Biopolymers

Doctor of Philosophy Dissertation

Computational Fluid Dynamic (CFD) Study of Polymer Microencapsulation Processes

Presented by Masooma Qizilbash

Advisors:

Alfredo Guardo Zabaleta

Luis J. del Valle

Department of Polymers and Biopolymers

Polytechnic University of Catalonia

Barcelona, July 2024

Acknowledgement

I would like to express my deepest gratitude to my supervisors, Prof. Alfredo Guardo Zabaleta and Prof. Luis J. Del Valle, for their excellent guidance and support over the past years. Their immense knowledge and expertise in the fields of fluid mechanics and polymers provided the foundation for this research. I am eternally grateful for their patience, encouragement and invaluable feedback throughout the various stages of my PhD. Numerous insightful discussions in their offices helped shape my analytical and critical thinking skills. This accomplishment would not have been possible without their dedicated mentorship.

I also thank all the faculty members at UPC's Fluid Mechanics and Polymers and bio- polymers department of UPC who imparted their wisdom through challenging questions and advice during conferences and seminars. My heartfelt appreciation also extends to the technical staff in both departments.

Finally, I express endless gratitude to my family for their unconditional love and sacrifices that enabled me to pursue this endeavor. To my beloved husband Bilal, and wonderful children Hassan, Hussain and Bali Sakina - thank you for keeping me motivated through difficult time frames and celebrating each milestone with me. This accomplishment is as much yours as it is mine.

Summary

Microencapsulation process of polymers and biopolymer is the most important technique in a polymer industry to make it unique and applicable in various fields of daily life. When it comes to the accuracy of the method only Computational Fluid Dynamic (CFD) simulations or numerical solution provides the authenticity of the method. CFD analysis gives a more schematic approach instead of any other Simulation method.

In this thesis detailed use of governing equations of CFD is used to predict the accuracy of the microencapsulation method. The experimentation was done in the laboratory of the department of polymers and biopolymers under the supervision of Prof Luis J. Dell Valle. By using CFD the results are more precise, clear and accurate along with the zero minimum percentage of human error. After representing a literature review for the modeling of microencapsulation process in the first chapter, the methodology about how the process began and what parameters we followed to fulfill the requirement of the project. The effect of impeller speed 5000 rpm, 7500 rpm, 1000 rpm, 12000 rpm and 15000 rpm were determined on the number density functions and particle size reduction in the microencapsulation domain.

Ansys. Fluent R2 2020 was used to model the experimental data. For the purpose of modeling the particle size distribution discrete method of population balance model is used. A total of five bins were selected to perform the size distribution analyze. The reason for selecting this small diameter range is the focus and accuracy of the solver. The bins should be more than enough to cover the distribution range and small enough to save computational time. Realizable k-e, Eulerian framework and appropriate bins initial values are used to predict the multiphase behavior. Under these conditions simulation converges very well and gives good agreement with the validation and experimental data.

List of Abbreviations

μm	Micrometer
BC	Boundary condition
CAD	Computer aided design
CFD	Computational fluid dynamics
CI	Confidence interval
CPI	Chemical process industry
DEM	Discrete element method
DES	Direct eddy simulation
DLS	Dynamic light scattering
DNS	Direct numerical simulation
DPM	Discrete phase model
IQR	Interquartile range
LEB	Lattice Boltzmann equation
LES	Large eddy simulation
m	Meter
MAE	Mean absolute error
MEDA E	Median absolute error
MRF	Multiple reference frames
nm	Nanometer
Nρ	Number density density
PBM	Population balance modeling
PD	Particle diameter
PEI	Polyethylene amine
PS	Particle size
PVA	Polyvinyl alcohol
RANS	Reynolds average Navier Stokes
RMSE	Root mean square error

RPE	Relative percentage error
RPM	Revolutions per minute

List of Appendixes

Appendix 1: Measurement of number density and fractions at different Impeller speeds
Appendix 2: Cumulative probability distribution
Appendix 3: Validation Results
Appendix 4: Error Analysis
Appendix 5: Statistical Analysis

Table of Contents

Acknowledgement 2
Summary 3
List of Abbreviations 4
List of Appendixes 6
Table of Contents 7
List of Figures 10
List of Tables 12
1 Microencapsulation process 14
  1.1 Brief description, Application and modeling 14
  1.2 Building blocks of Microencapsulated Particle 16
    1.2.1 Coating or Shell Material 16
    1.2.2 Inner Core Material 17
  1.3 Need for Microencapsulation 18
    1.3.1 Food Industry 19
    1.3.2 Pharmaceutical industry 20
    1.3.3 Personal Care and Cosmetics 20
    1.3.4 Textiles 20
    1.3.5 Agrochemicals 21
    1.3.6 Energy Storage 21
  1.4 Modeling a Microencapsulation Process 21
    1.4.1 Computational Fluid Dynamics 23
    1.4.2 Advances of CFD 23
    1.4.3 Governing equations of CFD 29
  1.5 Role of CFD in Polymer Microencapsulation 30
  1.6 Scope of Work 36
  1.7 Objectives of Study 38
  1.8 Methodology and Structure 38
References 39
2 Overview 45
  2.1 Apparatus and chemical Essentials 45
  2.2 Experimental Setup 45

2.3 Experimental Procedure 46
2.3.1 Sample Preparation 46
2.3.2 Introducing Phases 46
2.3.3 Impeller Speed Variation 47
2.3.4 Washing and Drying of Capsules 47
2.3.5 Scanning Electron Microscope (SEM) and Dynamic Scattering Light (DSL) images 47
2.4 Description of the Turrax Agitator used in the Rresearch 47
2.5 Description of Fluid Dynamics Created by the Counter Rotating Rotor and Stator 48
2.6 Efficiency of Turrax Agitator 50
2.7 Properties of the Materials 51
2.8 Computational Fluid Dynamics Approach 52
2.8.1 Pre-Processing 52
2.9 Approaches of CFD (Ansys Fluent 2020 R2) used in this Project 55
2.9.1 Turbulent Models 55
2.9.2 Multiphase Model 56
2.9.3 Breakage and aggregation kernel of Discrete PBM 57
2.9.4 Multiple Reference Frame 57
2.9.5 Simulation Settings 58
2.9.6 Adaption 59
2.10 Post-Processing Tool of CFD 60
2.10.1 Key Post-Processing Steps Included 60
2.11 Observation in form of Contours and Vectors 61
2.11.1 Contours 61
2.11.2 Vectors 61
2.11.3 Particle Number Density Function 61
References 61
3 Introduction 65
3.1 Validation Methodology 66
3.1.1 CFD Mathematical Approach 66
3.1.2 Computational Domain 71
References 75
4 Overview 79
4.1 Experimental Results 79

4.1.1 SEM (Scanning Electron Microscopy) Analysis 79
4.1.2 DLS (Dynamic Light Scattering) Analysis 82
4.2 Validation Results and Discussion 86
4.2.1 Effect of Impeller Speed on Turbulent Kinetic Energy 86
4.2.2 Effect of Impeller Speed on the Velocity in Mixing Domain 88
4.3 Qualitative analysis of Validation 90
4.3.1 Effect of Impeller Speed on Particle Size Distribution 90
4.3.2 Prediction of Particle Size Verses Cumulative Size Distribution 93
4.4 Error Analysis 96
4.5 CFD Simulation Analysis 97
4.5.1 Quantitative Analysis of Effect of Impeller Speed on Particle Sizes 98
4.5.2 Quantitative analysis of effect of impeller speed on particle sizes 98
4.5.3 Effect Of Impeller Speed (Rpm) on the Average Number Density of Particle Diameter ... 102
4.6 Qualitative analysis of the results 106
4.7 Effect of Impeller Speed (RPM) on Cumulative Size Distribution 108
4.8 Error Analysis 109
4.9 Calculation of D50 And D90 112
4.10 Statistical Analysis 114
References 116
5 Conclusions and Future Work 122
5.1 Conclusions 122
5.2 Future Work 123
Appendixes 126
Appendix 1 127
Appendix 2 128
Appendix 3 129
Appendix 4 131
Appendix 5 132

List of Figures

Figure 1.1 Microencapsulation process [5] 15
Figure 1.2 Roadmap of CFD-PBM redrawn from [3] 23
Figure 1.3 (a) Geometry creation (b) mesh generation (c) post-processing 25
Figure 1.4 Schematic diagram for meshes involved in CFD redrawn from [37] 26
Figure 2.1 Schematic diagram of experimental setup 46
Figure 2.2 Agitator assembly (a) parts of the dispersion tool, 1) shaft tube, 2) grooved piston, 3) shaft, 4) stator and 5) rotor. (b) Turrax homogenizer. 48
Figure 2.3 Description of phenomenon taking place inside Rotor-stator 49
Figure 2.4 Geometry of the system sketched on design modular of ANSYS fluent 2020 R2 53
Figure 2.5 Geometry of the rotor and stator part of the agitator sketched on design modular of ANSYS fluent 2020 R2 53
Figure 2.6 Tetrahedral mesh of (a) stator and (b) rotor 54
Figure 2.7 Mesh Quality of stator 55
Figure 3.1 Schematic diagram of emulsion cell geometry and its dimensions 71
Figure 3.2 Geometry constructed in the design modular tool of Ansys fluent 2020 R2 (a) Impeller and (b) Tank 72
Figure 3.3 Mesh of (a) Impeller and (b) Tank 74
Figure 4.1 Representation of the SEM particles with respect to Impeller Speed (a) 5000 rpm, (b) 7500 rpm, (c) 10000 rpm, (d) 12000 rpm, and (e) 15000 rpm. 82
Figure 4.2 Representation of a DLS graph at different impeller speeds. (a) 5000 rpm, (b) 7500 rpm, (c) 10000 rpm, (d) 12000, (e) 15000 rpm. 85
Figure 4.3 Represent the comparison of the contours of Turbulent Kinetic Energy obtained from the simulation by upper images are from Ansys Fluent 2020 R1 while lower images are from [1] Fathi Roudsari et al. 2012 at (a) 300 rpm, (b) 400 rpm and (c) 600 rpm 87
Figure 4.4 Comparison of contours of volume fraction at 600 rpm of Conroe oil and water 15% (a) Fathi Roudsari, (b) Simulation by Ansys Fluent 2020 R1 88
Figure 4.5 Velocity contours at cross-sectional plane of the tank at 88
Figure 4.6 Vectors of velocity at cross sectional plane of the tank (a) 300 rpm, (b) 400 rpm and (c) 600 rpm 89
Figure 4.7 Vectors of velocity at impeller within the tank (a) 300 rpm, (b) 400 rpm and (c) 600 rpm 90
Figure 4.8 Effect of (a) 300 rpm, (b) 400 rpm and (c) 600 rpm on the number density of the particles Fathi Roudsari (2012) (blue column) and CFD data (red column) 92
Figure 4.9 Effect of rpm on particle size distribution for data obtained in the current CFD study at 300 rpm, 400 rpm and ....600 rpm and the experimental outcome at 300 rpm, 400 rpm and 600 rpm93
Figure 4.10 Cumulative size distribution at (a) 300 rpm, (b) 400 rpm and (c) 600 rpm 94
Figure 4.11 Cumulative drop size verses droplet diameter at impeller speeds. CFD data at 300 rpm, 400 rpm and 600 rpm. Fathi Roudsari data at 300 rpm, 400 rpm and 600 rpm 95
Figure 4.12 Cumulative drop size verses droplet diameter at impeller speeds Relative Error (%) and Absolute Error (%) 97

Figure 4.13 Trend of number densities of larger and smaller particles at (A) 5000, (b) 10000 rpm and (c) 15000 rpm 102

Figure 4.14 Trend of average number density of particles 0f bin at center, interface and cross-sectional plane of the tank at (a) 10000rpm and (b) 15000 rpm 104

Figure 4.15 Number density obtained at different H/D ratio for larger and smaller particles of the tank at 12000 rpm 106

Figure 4.16 Experimental and simulation comparison of bin fractions verses particle diameters at (a) 5000 rpm, (b) 7500 rpm, (c) 10000 rpm, (d) 12000 rpm and (e) 15000 rpm Experimental data and simulation data 107

Figure 4.17 Comparison of simulation and experimental cumulative size distribution at different impeller speeds for PEI microcapsules exp CSD at5000 rpm, sim CSD at 5000 rpm × exp CSD at 7500 rpm CSD at 7500 rpm, exp CSD at 10000 rpm, sim CSD at 10000 rpm exp CSD at 12000 rpm sim CSD at 12000 rpm, exp CSD at 15000 rpm - sim CSD at 15000 rpm, ... 108

Figure 4.18 Error analysis of particle size distribution at various impeller speeds IQR (Inter quartile range) MAD(mean absolute deviation), MAPE (mean absolute percentage error)× ME(mean error), *RMSE(root mean square error), ... 110

Figure 4.19 Relative error of particle sizes at different impeller speeds, 5000 rpm, 7500 rpm, 10000 rpm, 12000 rpm and 15000 rpm 111

Figure 4.20 Average relative error of particle sizes at different impeller speeds 112

Figure 4.21 D50 Calculation of simulation and experimentation (a) numerical and (b) theoretical sim and Experimental 113

Figure 4.22 Confidence interval 95% of particles diameter at (a) 5000 rpm, (b) 7500 rpm, (c) 10000 rpm, (d) 12000rpm and (e) 15000 rpm sim CLupper bound, sim CI lower bound, exp CI upper bound, exp CI lower bound 115

List of Tables

Table 2.1 Specifications of Turrax 51

Table 2.2 Materials properties used in the solver was mentioned in the table.............................. 52

Table 2.3 Settings of the solver 58

Table 4.1 Average particle diameters obtained at different impeller speeds from SEM............... 82

Table 4.2 Representation of average particle diameter (m) and impeller speeds (rpm) obtained from DLS 83

Chapter 1

Introduction

1 Microencapsulation process

1.1 Brief description, Application and modeling

Microencapsulation involves enveloping solid, liquid, or gaseous materials within a thin polymeric shell, forming microcapsule particles. Specifically, it is a technique used to encapsulate core substances whether solid, liquid, or gas with a protective coating. Microencapsulation provides important benefits such as increasing the solubility of active ingredients that may otherwise have poor solubility characteristics. The microencapsulation process creates miniature capsules or particles on the micrometer scale, with each capsule composed of an outer polymeric coating that surrounds and isolates an inner core material. The core can be composed of a wide variety of substances such as drugs, enzymes, flavors, fragrances, pigments, or any material that requires protection, controlled release, or masking of its properties. The coating layers used for microencapsulation are typically made from natural or synthetic polymers that form a protective barrier around the core material. This allows microencapsulation to increase solubility, bioavailability, and stability of core substances while also enabling controlled or targeted release over time [1].

Microencapsulation systems are classified based on particle size. Microparticles, microcapsules, or microspheres have diameters below 1000 μm, nanoparticles range from 1- 1000 nm, and particles over 1000 μm are considered macro particles [2]. Microencapsulation involves surrounding micro- scaled solid matter, fluid droplets, or gases within an inert external layer, thus providing shielding from external influences and earning the encapsulation descriptor [3]. The particles acquired through this process are denominated as microspheres or microcapsules, enveloped by a wall material distinctly separating them from ambient surroundings [4].

One common technique used for microencapsulation is emulsification as shown in Figure 1.1 whereby a core material is dispersed within an organic solvent containing the wall-forming polymer material. In this process, the core-solvent dispersion is first prepared by dissolving or suspending the active ingredient inside an organic solvent along with the selected coating polymer. This dispersion is then emulsified into a non-miscible liquid, typically water or oil, to which an emulsion stabilizer is added. During emulsification, the organic dispersion is introduced into the aqueous or oily phase and homogenized to form small oil-in-water or water-in- oil droplets. The stabilizer aids in preventing coalescence of these droplets. The organic solvent is then slowly evaporated away, allowing the coating polymer within each droplet to precipitate and deposit around the encapsulated core material. As the solvent dissipates, the wall-forming polymer precipitates and self- assembles into a thin, compact structure enclosing and isolating the core substance. This creates microcapsules with the active ingredient encased within a polymeric shell. Repeated washing can be done to ensure full removal of any residual solvent. The result is a microencapsulated product consisting of micrometer-sized particles, each containing a core protected by a thin, continuous polymeric membrane [5, 6].

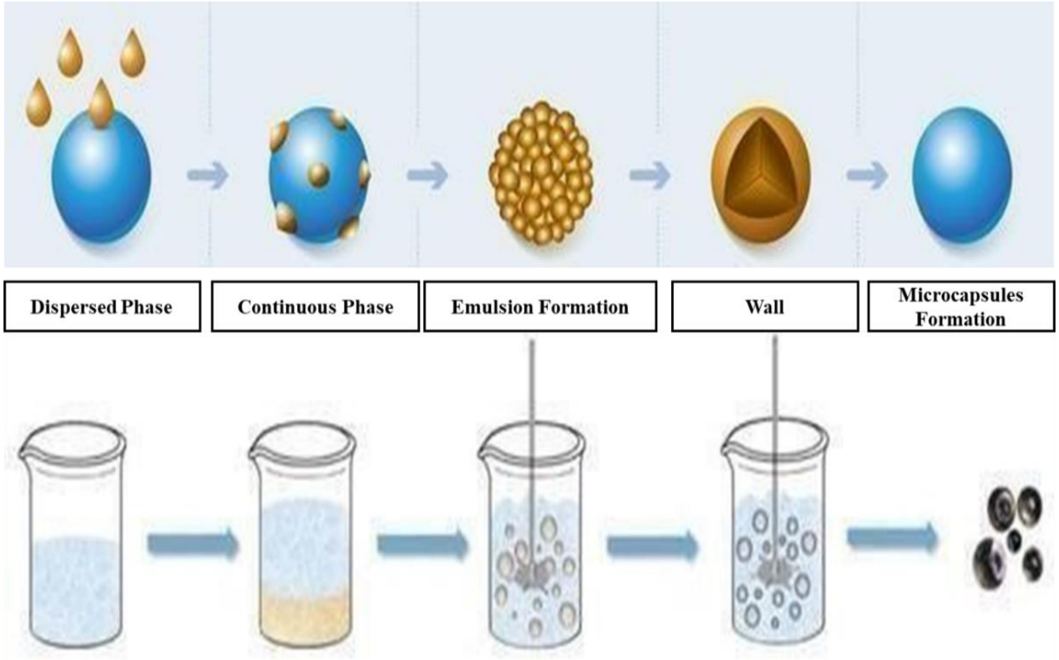

Figure 1.1 Microencapsulation process [5]

Emulsion technology has a long history of applications in the food industry, enabling a wide variety of products such as homogenized milk, creams, dips, dressings, sauces, and desserts through dispersion of liquid ingredients. However, recent advancements in emulsion science are facilitating novel emulsion-based approaches to enhancing food quality and functionality. From one of the advanced emulsion technology, multiple emulsions incorporate droplets that encapsulate even smaller immiscible liquid particles, showing promise for reduced- calorie solutions, encapsulation applications, and controlled release. These advanced emulsion types have the potential to support innovative food and beverage products with enhanced qualities related to nutrition, health, sensory properties, and sustainability compared to traditional emulsions. A better understanding of their formulation and performance could unlock opportunities for application across the food industry [7].

1.2 Building blocks of Microencapsulated Particle

Microcapsules and microspheres are particulate delivery systems that encapsulate or entrap active ingredients. Microcapsules refer to particles consisting of a core material surrounded by a coating membrane or shell, forming a capsule-like structure. They can contain either solid or liquid cores. Microspheres, on the other hand, are matrix particles that encapsulate a substance within a spherical coating matrix without necessarily having a distinct core-shell structure. Microcapsules can have a single core or multiple nuclei, and double or multilayer coatings in some cases. Their shapes and sizes are also quite variable. Achieving ideal microcapsules depends on selecting a liquid core/shell fabrication method prior to solidification. Characterizing the microcapsule membrane and interior physical qualities like porosity and crystallinity quantitatively remains challenging, though some progress has been made using release data, dimensions, densities and core/wall ratios. The effects of size and shape distributions are also areas of ongoing research focus[8].

1.2.1 Coating or Shell Material

A wide variety of coating materials can be used for microencapsulation. Some innovative coating polymers have also been developed for specialized applications, particularly for bio-adhesive and muco-adhesive applications. Additionally, many traditional materials are suitable for use in the gastrointestinal tract, including inert and pH-sensitive polymers containing carboxylate and amino groups that swell or dissolve depending on their cross- linking. When selecting an appropriate coating material from the extensive list of candidates, researchers must consider several criteria: 1) What are the specific product requirements and objectives, such as stabilization, reduced volatility, controlled release properties, and ability to withstand environmental conditions. 2) Which coating material will satisfy both the product goals and functional needs? 3) Finally, which microencapsulation method is best suited to achieve the coated product objectives? The chosen coating polymer significantly impacts the microcapsules' physical and chemical properties. Requirements like stabilization, reduced volatility, release characteristics and environmental stability should guide polymer selection. The polymer must also form a cohesive, non-reactive film with the core material while imparting desired coating attributes such as strength, flexibility, impermeability and stability [9]. Common coating materials used include both hydrophilic and hydrophobic polymers, as well as combinations thereof. Examples that have been effectively used include gelatin, polyvinyl alcohol, ethyl cellulose, and cellulose acetate phthalate and styrene maleic anhydride. Film thickness can be varied based on factors like core surface area and system characteristics. Microcapsules may consist of single or clustered particles. Following isolation and drying, the powdered product is amenable to formulation into various delivery formats [10].

1.2.2 Inner Core Material

The core material refers to the active substance being encapsulated by a coating layer in order to serve a specific purpose. The core can exist as solids, liquid droplets, or dispersions. The makeup of the core material can vary widely, offering flexibility in designing microcapsules with targeted properties. Altering the core composition allows for effective formulation development. There are several reasons why a substance may require microencapsulation. Examples include protecting reactive components from external environmental degradation, safe handling of normally toxic or hazardous materials, taste masking, facilitating controlled or modified release profiles, converting liquids into free- flowing powders, and modifying drug physical properties. Microencapsulation can also enable convenient handling of liquid materials in solid form. Precise dosing, flowability, and stability can be conferred by encapsulating active substances within coating layers. Microencapsulation offers a means for altering material properties in ways that optimize downstream applications and uses [11].

The coating material used determines the appropriate production technique, which in turn influences microcapsule properties such as size, morphology, porosity, hydrophobicity/phobicity, surface tension, and thermal behavior. Understanding these properties is vital for comprehending microcapsule behavior in food systems. The properties also closely relate to the controlled release functionality of encapsulated cores. The core needs adequate protection to release at specific times, improving microencapsulation efficacy and applications. Major factors influencing core release are the core nature, core- coating ratio, coating nature, and their interaction. In several research microencapsulation concepts for food i-e the need, coating/core materials, production techniques, microcapsule properties like physical/mechanical/thermal/functional characteristics, and release mechanisms have been discussed [12].

1.3 Need for Microencapsulation

Microencapsulation has widespread applications across multiple industries due to its ability to provide protection, enable controlled delivery, and enhance product formulations. Early research in the 1980s demonstrated how microencapsulation could be used to achieve prolonged and sustained drug release from tablets, capsules, and injectable by controlling the diffusion of encapsulated drug substances [13]. Enteric coatings that specifically target drug absorption in the intestines over the stomach region were also developed using microencapsulation techniques [14]. Taste masking of bitter compounds was another application explored to improve the palatability of pharmaceutical formulations [15]. Microencapsulation further aided in incorporating oily active ingredients within compressed solid dosage forms like tablets [16]. More broadly, encapsulation provides shielding of actives from environmental hazards such as moisture, oxygen, heat and light [17]. It also enables the separation of incompatible substances that could otherwise undesirably interact upon direct contact [18]. Microcapsules help reduce volatility and allow stable storage of evaporation-prone compounds. Lastly, encapsulation decreases potential dangers from handling toxic or noxious substances after incorporation within the protective barrier.

1.3.1 Food Industry

Microencapsulation in foods provides protection and improved delivery of sensitive components. Many beneficial components like essential oils, microorganisms, and probiotics are vulnerable to oxidation from heat, light and oxygen. Encapsulation offers a solution by shielding these actives. Studies have shown encapsulation increases thermal stability. Encapsulation has been done on garlic oil within β-cyclodextrin for heat protection to maintain antimicrobial effects [19].

Similarly, there is a work which encapsulated Peumus boldus oil using coacervation before incorporating into seeds, protecting against fungi [20]. A work encapsulated probiotic strains within resistant starch and calcium alginate gel via extrusion, improving survival in cheese after 6 months of storage. [21]. One of the research also demonstrated limonene encapsulated within β- cyclodextrin via extrusion effectively protected it from oxidation [22].

Improved delivery ensures complete release of encapsulated components upon controlled release based on shell material selection. In one of the research scientists used soy protein coating for probiotic delivery in the gut, finding it enhanced viability against low pH and digestive enzymes [23]. Controlled release is important where actives are only active at certain locations or times. encapsulated probiotic L. casei in alginate, releasing in coconut water when cell numbers increased enough to burst beads [24]. Similarly work done on trapped garlic flavor in a biopolymer gel, delaying release until later cooking stages [25]. Microencapsulation also masks undesirable flavors and smells, allowing inclusion of components like fish oil and protein hydrolysates [26]. A work showed mussel hydrolysate bitterness was masked using modified starch and maltodextrin encapsulation [27] likewise an article obscured iso-flavone odor and taste using the same carriers.

1.3.2 Pharmaceutical industry

Current research in the field of pharmaceutical microencapsulation is primarily focused on developing new drug delivery systems (DDS) that can meet various requirements for marketable products. These systems aim to minimize adverse reactions and side effects, ensure compatibility with desired administration methods, enable targeted delivery, extend shelf life, enhance patient compliance, and potentially facilitate controlled and sustained release of active compounds [28]. Microencapsulation is considered a promising technological approach to achieve these objectives. Microparticles, consisting of combinations of active pharmaceutical ingredients (APIs) and biomaterials, are often employed in microencapsulation. API molecules can have a short half- life and may undergo rapid hydrolysis or enzymatic degradation in vivo, necessitating frequent administration. Microencapsulation techniques are utilized to protect APIs from degradation, allowing for controlled release and maintaining therapeutic concentrations over an extended period. The properties of the biomaterials used in microencapsulation, particularly whether they are erodibleor non-erodible, determine their fate following administration. Erodible biomaterials may dissolve or degrade over time, while non-erodible materials can persist in the body indefinitely [29].

1.3.3 Personal Care and Cosmetics

Microencapsulation is used in the personal care and cosmetics industry to encapsulate and deliver active ingredients such as vitamins, fragrances, and skin-care agents. Encapsulation enhances stability, protects ingredients from degradation, and enables targeted release for prolonged efficacy. Particle size control ensures uniform application and improved sensory attributes in cosmetic products [30].

1.3.4 Textiles

Microencapsulation has gained importance in the textile industry for the development of functional fabrics. Encapsulating materials such as phase change materials, antimicrobial agents, or fragrances allows for controlled release and improved performance of textiles. Uniform particle size distribution ensures even distribution of encapsulated materials within the fabric, leading to enhanced functionality and durability [31].

1.3.5 Agrochemicals

In agriculture, microencapsulation is used to protect agrochemicals, such as pesticides or fertilizers, from degradation and to provide controlled release for prolonged effectiveness. Encapsulated agrochemicals can be delivered directly to the target site, minimizing environmental impact and maximizing efficacy. Controlling particle size distribution enables uniform coverage and distribution of the encapsulated agrochemicals [32].

1.3.6 Energy Storage

Microencapsulation plays a role in energy storage systems, such as lithium-ion batteries. Encapsulating active materials within microspheres or nanoparticles improves their stability, prevents unwanted reactions, and enhances energy storage performance. Precise control over particle size distribution ensures consistent electrode morphology and optimal electrochemical performance. Overall, microencapsulation and control of particle size distribution are necessary in various areas where protection, controlled release, targeted delivery, and improved performance of encapsulated materials are required. These applications span industries such as pharmaceuticals, food and beverages, personal care, textiles, agriculture, and energy storage.

1.4 Modeling a Microencapsulation Process

The field of emulsion polymerization modeling continues expanding with numerous prospects of scholarly and commercial importance. Models can furnish comprehension and discernment into the intricate mechanistic behavior of emulsion polymerization reactions. Moreover, corroborating models with experimental data has the potential to uncover gaps in existing knowledge warranting further research from both empirical and theoretical perspectives.

Knowledge-driven models that have been validated against specific systems can simulate industrial formulations involving multiple monomers in the presence of assorted emulsifiers and initiators under non-isothermal conditions with diverse feeding methods for reactant inputs. Nonetheless, developing, solving, and corroborating models simulating industrial recipes defined by such a variegated array of compositional and operational intricacies remains a notable challenge. Continued progress elucidating our understanding promises additional opportunities for innovative applications within both the academic and industrial spheres [33]. A roadmap to understand the way to accomplish results from CFD-PBM simulations is illustrated in Figure 1.2. Now here the question is what should be the accomplishment from the polymer simulation? Finding the answer becomes easy when this question is clear. To find a meaningful answer, in a study by [34] some models were discussed for the new as well as for established researchers to understand polymer simulation. These models were atomistic models, coarse- grained models (CG), and hybrid models. Each model has its own specification to implement; for example, if one selects an atomistic model, then the first need is to find a force field and then an initial configuration along with a simulation algorithm. After selecting the model comes the selection of a simulation method and then analyzing the simulation results at the end. From all the above explanations a general roadmap is sketched that leads us to the polymer simulation bydecreasing time and increasing the length scale.

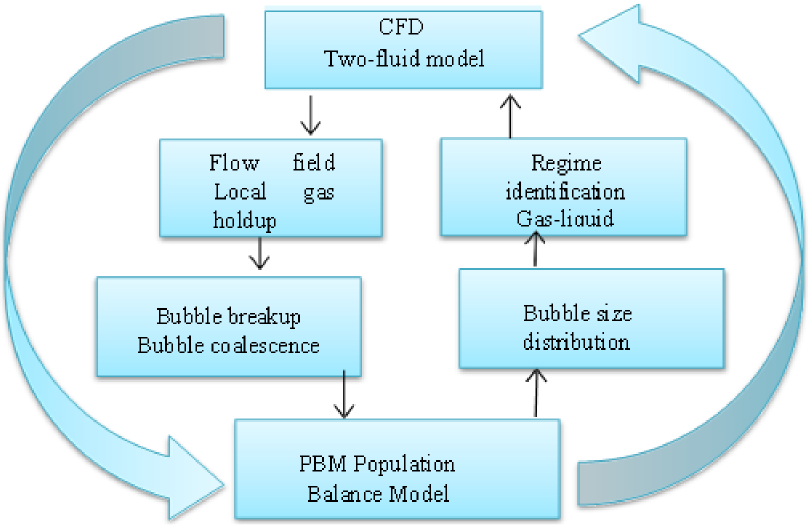

Figure 1.2 Roadmap of CFD-PBM redrawn from [3]

1.4.1 Computational Fluid Dynamics

Computer-based simulation plays a significant role in advancing our understanding of complex processes by enabling the simulation of intricate physics and chemistry, creating validated models, and utilizing them for process scale-up, scale-down, optimization, and control. Given that fluid flow and particles are involved in almost all processes within the Chemical Process Industries (CPIs), this discussion will primarily focus on Computational Fluid Dynamics (CFD) alongwith Population balance modeling. Simulation has a promising future, and individuals with strong computational skills will find numerous opportunities in academia and industry alike.

1.4.2 Advances of CFD

Let's understand the CFD first. Above mentioned scheme in Figure 1.3 is the basic portfolio redrawn [35] to conduct the CFD-PBM simulation. Initially modeling is carried out by scientists Claude- Louis Naiver and George Gabriel Stokes. They developed the Navier- Stokesequation which is one of the important pillars of Computational fluid dynamics. They worked with several numerical equations to solve different problems related to the fluid domain. Generally governing equations that take part in completing the characteristics of CFD are the equation of continuity, Newton´s second Law of motion, and the first Law of thermodynamics. The basics for all CFD problems are the Naiver-Stokes Equation. The first computer used to design a fluid flow using

Navier´s and Stokes Equation was established in Los Alamos National Laboratory with the T3 group. Francis H. Harlow, a laboratory faculty member, worked on Computational fluid dynamics and became a pioneer in his work from 1957 to the late 1960´s. He and his fellows worked on a transient 2- dimensional fluid flow on different numerical methods, particle-in-cell, fluid-in-cell, vorticity stream function, and marker and cell method.

Lewis Fry Richardson was a pioneer, devising fluid flow modeling for weather forecasting applications in 1922. His vision included a forecasting 'factory' populated by 64,000 human computers hypothetically performing calculations by hand - referred to as the 'Fantastic Weather Factory'. Though conceptual, this work proved highly influential for modern simulation capabilities. A recent study [36] provided an overview of various computational fluid dynamics advances over the past years. Areas discussed in his study included improved pressure-coupling methodologies, enhanced numerical schemes and refined element sizes. Parallel computing was also assessed. The authors determined that for problems involving approximately 100,000 elements, a single processor would suffice. However, for problems exceeding 200,000 elements, two or more processes would be necessary. Richardson's early fluid modeling concepts for weathe rprediction laid important groundwork. Later evaluations such as [36] assessed ongoing CFD refinements. Collectively, these advancements continue pushing the boundaries of simulation- based understanding of fluid behavior - building upon Richardson's pioneering vision utilizing computational methods for predicting complex natural phenomena. His imaginative conceptualization of leveraging human 'computers', though theoretical, demonstrated prescience regarding simulation capabilities to come.

1.4.2.1 Stages Involved in CFD

To understand the method of processing CFD certain stages should be considered. The following Figure 1.3 represents the basic steps required to conduct Computational Fluid Dynamics, building the geometry of the project or the body on which the simulation has to be carried out. Meshing is important in work, without it, the path line for the velocity vector will not be estimated. Meshing in the CFD analysis is the part that is unknown to the engineer. The boundary condition needs to be applied so that the simulation knows the defined parameters to work on.

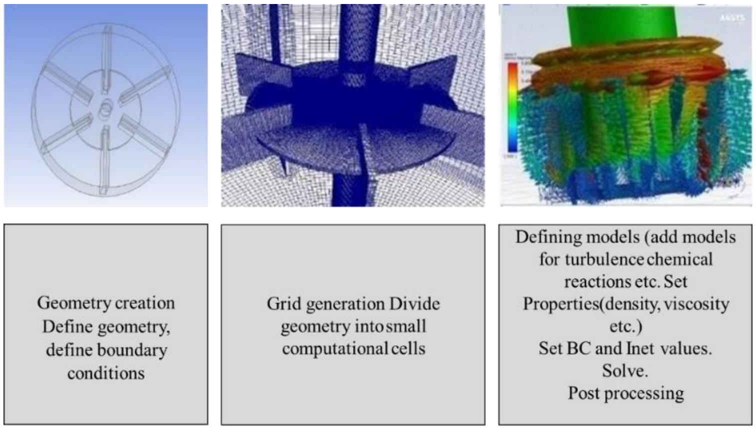

(a) (b) (c)

Figure 1.3 (a) Geometry creation (b) mesh generation (c) post-processing

1.4.2.2 Geometry Generation

Developing geometry is the first fundamental step in setting up a CFD simulation. The process begins with creating a 2D or 3D representation of the physical system being modeled. Commercial CFD software packages typically contain CAD modeling tools to design or modify geometries. However, geometries can also be drawn in external CAD programs and imported. While general- purpose CAD programs allow for detailed designs, they may include features unnecessary or problematic for CFD analysis (e.g. small fasteners). Geometries developed in external software therefore need to be "cleaned" or simplified before meshing. Details beyond the scale of the grid resolution should be removed to focus the geometry on the relevant fluid domain boundaries and surfaces. Additionally, CAD models not designed for simulation sometimes contain anomalies like overlapping faces or non-manifold geometry that prevent mesh generation. Any such issues must be addressed prior to importing into the meshing module of a CFD code. Only cleaned, valid CAD representations of the physical system under examination can successfully be meshed and used to initialize computational fluid dynamics simulations [37].

1.4.2.3 Mesh Generation

There are two approaches to meshing the physical domain as shown in Figure 1.4 structured and unstructured meshes (and a combination of both known as hybrid meshes). The former utilizes blocking, where the physical domain is divided into computational blocks in which the user can control node count, spacing, and growth ratios. The latter utilizes built-in meshing tools, either propriety or otherwise, which work to fill the physical domain with computational cells in several different ways [38].

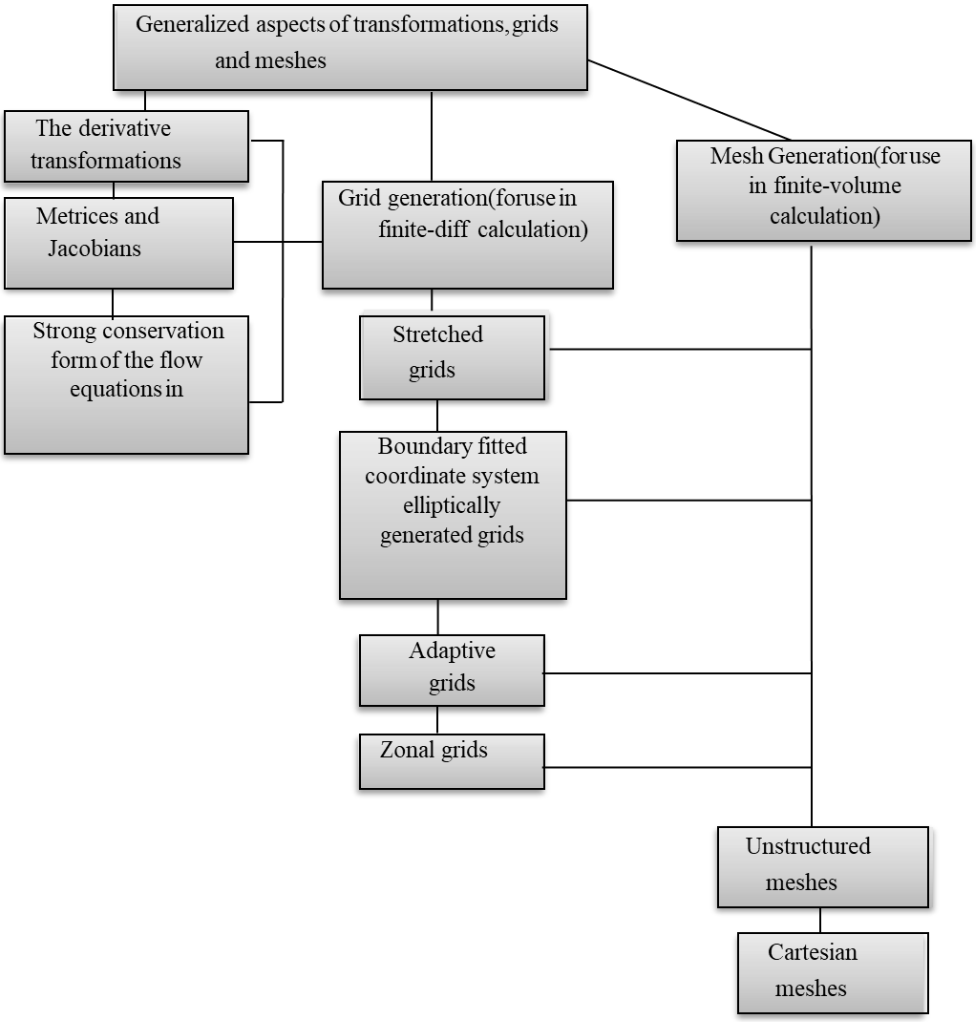

Figure 1.4 Schematic diagram for meshes involved in CFD redrawn from [37]

Before running the simulation, it is important to analyze the mesh quality to ensure an accurate solution. The meshing software contains built-in quality checks that are used to evaluate different aspects of the mesh. Some of the most important quality metrics checked include element quality, aspect ratio, and cell skewness [39]. Element quality refers to the shape of the elements (e.g. triangles/quads in 2D, tetrahedrons/hexahedrons in 3D). A perfect value of 1 indicates a regular shape like a square or cube, while lower values indicate a more irregular shape.

1.4.2.4 Solution setup

Setting up the solver in Fluent is an important phase prior to running the simulation. Proper configuration of various modeling aspects is required [40]. When dealing with multiphase systems, selection of appropriate models to represent the different phases and their interactions needs to be done first. Next, the turbulence model needs to be selected and its constants adjusted based on the physical phenomena under investigation. Turbulence has a significant impact on flow behavior, so the correct model is crucial. Finally, boundary conditions describing the inlet/outlet flow rates, pressure specifications, wall properties etc. must be applied to fully define the problem. Boundary conditions inform the solver of constraints on the domain boundaries and initiate flow movement. Only after completing these key steps of specifying models, turbulence settings, and boundaries is the simulation setup complete and ready for computation. Initialization of the solver and calculation of the flow field can then begin to solve the governing equations subject to the user- defined conditions. Proper configuration at this stage helps ensure the validity and accuracy of results.

1.4.2.5 Turbulence Models

The k-ω turbulence model is a two-equation model that solves transport equations for the turbulence kinetic energy (k) and the specific dissipation rate (ω). This model is known for its ability to accurately predict flow separation under adverse pressure gradients, making it suitable for complex boundary layer flows [41]. In contrast, the k-ε turbulence model is another two-equation model that solves transport equations for the turbulence kinetic energy (k) and the turbulence dissipation rate (ε). Despite its relatively lower computational cost compared to more complex models, the k-ε model is widely used in computational fluid dynamics (CFD) due to its robustness and reasonable accuracy42]. RANS (Reynolds-Averaged Navier-Stokes) turbulence models are a class of models that solve the time-averaged Navier-Stokes equations to model the effects of turbulence. This class of models ranges from simple algebraic formulations to more complex two-equation models, such as the k-ω and k-ε approaches. The choice of the appropriate turbulence model depends on factors like the specific flow problem, the desired level of accuracy, and the available computational resources [43].

1.4.2.6 Eulerian Multiphase model

The Eulerian modeling method is well-suited and extensively used for simulating complex multiphase flows. In the Eulerian framework, each phase is treated mathematically as an interpenetrating continuum Conservation equations are written for each phase independently to model phase interaction effects rigorously. A key advantage of the Eulerian approach is its natural consideration of interphase forces such as drag, lift, virtual mass that dictate multiphase flow behavior. These influential forces are incorporated directly as interaction source terms between phases. This allows for accurate prediction of phase distribution, mixing, and heat/mass transfer effects. Furthermore, the Eulerian method is robust and computationally efficient even for systems involving a large number of discrete phases [44]. It circumvents the challenges of tracking individual particle trajectories as in a Lagrangian method. This facilitates simulation of industrial- scale, polydisperse multiphase processes.

1.4.2.7 Population balance modeling

Although the discrete method of population balance modeling has an increased computational cost in some conditions, it replicates the physical situations more accurately than any other method. In order to understand the hydrodynamics of a multiphase system where particle size distribution determination is the main focus discrete population balance model plays a vital role in the solution. Equation related to the modeling is further described in the following sections.

1.4.3 Governing equations of CFD

CFD is incomplete without considering the basic equation which are the important parameters of the simulation basic information regarding the two fluid model.

1.4.3.1 Equation of Continuity

Some other researchers also talked about the importance of these equations in computational field, which are the pillars of the computational fluid dynamics domain. One of them is the equation of continuity which is the fundamental part of a mass conservation means that the total mass flow rate inside the control volume is equal to the rate of change of mass in a control volume. The general form of an integral equation is as follows:

$$\partial/\partial t = \int cv\,\rho.dv + \int cs\,\rho v.\vec{n}\,dA = 0, \forall\, v \in \mathbb{R} \tag{1.1}$$

$$\rho + \nabla \left(\rho v\right) = 0, \forall\, v \in \mathbb{R} \tag{1.2}$$

1.4.3.2 Naiver Stokes Equation

All the governing equations study was taken by [45] According to his research to define Navier Stokes equation, first need to understand the principle on which it depends and hence it depends upon the Newton's second law of, which says that the rate of change of momentum is equal to the forces applied to the object for movement. The mathematical form of the definition is as follows

$$\sum F = \partial/\partial t \int CV(\rho v).dV + \int CS\rho(vv).n.dA, \forall\, v \in \mathbb{R} \tag{1.3}$$

Equation 1.3 consists of two parts the body force part and the second term is the surface force part

$$\partial/\partial t\,(\rho v) + \nabla.(\rho vv) = \rho g + \nabla.\sigma ij \tag{1.4}$$

$$\partial/\partial t\,(\rho v) + \nabla.(\rho vv) = \rho\,(\partial v/\partial t + (v.\nabla)\,v) = \rho\, Dv/Dt \tag{1.5}$$

$$\rho g + \nabla.\sigma ij = body\, force$$

Equation (14) is also known as LAGRANGIAN and EULERIAN Derivatives

1.4.3.3 Energy Equation

Energy equations consist of kinetic energy term

$$\Delta E = \rho\,(D/Dt)\,(\,e + 1/2(V2) \qquad (1.6)$$

$$W = -\nabla\cdot(Pv) + \partial(rXuX/\partial X + \rho Vg| rX \parallel X \qquad (1.7)$$

where w is the work done on the control volume the fine form of the Cauchy equation is

$$\rho(Dv/Dt) = \rho g - \nabla\ P + f \qquad (1.8)$$

1.5 Role of CFD in Polymer Microencapsulation

The research developed in a study [46] on a laboratory scale mixing tank where author mixed water in Conroe oil and Troika oil at different volume fractions and at different speeds of Rushton turbine impeller. He determined the particle size distribution that occurred due to breakage and coalescence of water droplets at different speeds i-e 300 rpm, 400 rpm and 600 rpm and determined the effect of impeller speed on drop sizes. Computational model Fluent 6.3.26 was used to model the project on mixing water in oil emulsions. This in detail used k-$\mathscr{E}$ model and the Eulerian-Eulerian approach and different methods of computational fluid dynamics like a discrete method of population balance modeling. He used multiple reference frames to model the impeller speed. He concluded that increasing the impeller speed in the case of Conroe oil gives a smaller drop size. Also, it is demonstrated that the turbulent kinetic energy difference between the impeller area and the circulating area is the same whereas for troika oil, this difference is higher. He also developed a comparison between experimental and simulation outcomes and stated satisfactory similarities.

In extension to the work of Farhad Ein Muzzafari, another author in his article used the same parameters described in the research of Farhad Ein Muzzafari but he used the DPM model coupled with the eulerian-eulerian langrangiam approach to see the effect of the trajectory defined in the DPM on the droplet size distribution and he validated that against the experimental data and got good agreement. Mostly parameters we used in our study was similar to the work done by these two researcher but the only difference is that the design of the impeller is and its speed was different we used turaxx agitator which is very common now a days for a homogeneous mixtures. The speed we used was higher than the speed used by the previous researcher and due to which we got smaller diameters which is the essence of every homogeneous mixture and we validated this model against our experimental data which match very well [47]. In an article [48] established the comparison between the experimental data and simulation data. He used a mixing tank having baffles and an agitator and mixed oil (Nexbase oil mixture contains oil 85% by weight and toluene 15% by weight) and brine (prepared by mixing water in 3.5% NaCl) at various speeds. He split the experiments into two parts and, in each part varied the concentration of the mixture. In one part of the experiment, he used 85% of the oil and 15% of water phaIse and changed the speed of the impeller from 3500 RPM for 120 s to develop the breakage to 2000 RPM for 240s to create the coalescence, further decreasing the speed to 1000 RPM for 300 s to establish the equilibrium and then again reversed it to 3500RPM for 120 s. for the 2nd part of the experiment he used surfactant SPAN 80, the pattern of the impeller rotation is same, but the levels are different like 2500 RPM, 1500 RPM, 500 RPM. To examine the particle size distribution experimentally, the researcher added PVM probes at 6 s of frequency, where as to determine the value of drop sizes computationally, he used Fluent 15. In Fluent 15 he used the Euler-Euler approach and a sliding mesh method to determine the particle size distribution and concluded that simulation gives a good collaboration with the experimental results.

Another work on computational fluid dynamics in the prediction of particle size was done by [49] He used a flat cylindrical tank of diameter 101mm, volume 146 ml, equipped with an impeller having a diameter of 89mm and thickness of 6mm to perform the experiments for the evolution of particle size in the oil-in-water system for a water-in-water mixture and removal of the added oil from double emulsification of oil-in- water-in-oil. Ex CFD, STAR simulated this system.CD (a volume code), and PROSTAR was used for pre and post- processing. The calculation was done by K10, k256 GB RAM and IRIS 6.3. The results showed that the system is perfect for the 2-phase flow process, but this system is not justifiable when it comes to a 3-phase flow problem. Also, this system doesn't work for low- volume fraction liquids.

Experiments have been done to objectify the turbulent phenomenon on the droplet breakage for a homogenization unit. The parameters he considered were certain assumptions like minimal coalescence drop and binary drop breakage [50]. Materials used for conducting the experiments were soybean oil of 0.5 wt. % behave as a dispersed phase, 0.1 wt. % nanoionics surfactant, which acts as an emulsifier, pre-emulsion mixture was prepared 100 ml by a rotating device at 13000 rpm. 5ml of this pre-emulsion was forced at 10000 psig and, by varying pressure, created drop breakage 9 units were recycled and the sample was collected to compute the drop size supply by COULTA LS 230 Analyzer. This whole process was visually seen by a 20*40 microscope, viscometers calculated viscosities. The CFD model was used with fluent version 6.2.16 to analyze the flow region; the meshing was done by Gambit V2.2.30. After the convergence, the solution has less than 10-5residuals. Population balance modeling equations were set to develop the particle size in the turbulent regime of a homogeneous system. From all the above experimental detail, the results concluded that in the beginning, the results varied and didn't match with the experimental values after 300 minutes at a high dissipation rate of 0.35 and 0.5 w/kg gives a very accurate prediction of drop size distribution

A work investigated the population balance model for breakage and droplet for the emulsification units. He used the baffled jacketed tank along with a condenser having cooled water for better evaporation of water [51]. The tank was equipped with an agitator known as a TT propeller. The purpose of this paper was to co- relate the work of various authors regarding the prediction of particle droplet distribution, especially in the breakage droplet field. Materials were prepared from ethylene glycol distearate which acts as an oil and water as a water phase, so this was basically oil-in- water emulsification system. The surfactant used in this emulsion was trico ethylene glycol dodecyl ether. The ratio of the oil and surfactant was 2:1. Experimental was done at different concentrations and various rotation speeds and observed by the in situ Video probe. The results were then compared to the simulation results, which showed a good match. Population balance modeling was successfully established using certain transport equations consisting of breakage and aggregation terms. In the beginning, in a few models the results didn't go well with experimental data, but by changing velocity, accuracy between simulation and experimental results increased.

In one study [52] experiment focused on three areas: a rotor, a stator, and a tank in which the mixing element must be inserted for mixing. The flow rate was determined by the velocity of the fluid entering from the base holes present in the rotor of a toothed rotor-stator mixer as a part of geometry. He only studied the diameter of the particles during breakage processes in emulsification mixing by considering Quassi- steady 2D linear flow. To see the effect of the pattern of flow on particle sizes, he used Fluent 15. A square-cell-based method was used in the gradient part, and the PISO scheme was selected under the pressure velocity coupling tab. In this research, he compared the droplet sizes in breakage of a 2D linear flow and 3D lamina flow and calculated the maximum stable size of particles theoretically from the equation

$$\sum F = \partial/\partial t \int CV(\rho v).dV + \int CS\rho(vv).n.dA , \forall\, v \in \mathbb{R} \tag{1.9}$$

Where d_{max} represents the maximum stable diameter, σ is the flow parameter whose values vary, Ca_C is a critical capillary number, and λ is the viscosity ratio. As a conclusion from the experimentation and simulation, it is decided that CFD is the efficient tool that gave quite close results for two models.

In the article by [53] simulation of a baffled mixing tank having a Rushton turbine impeller was done. The paper's objective was to optimize the impeller's inner rotating zone. To achieve this concept, the tank's inner and around the rotating zone was divided into 6 different regions. At every region, simulations have been done by using the finite volume method Ansys Fluent package 14.5. After creating the geometry and mesh selection from the tool present in the software a tetrahedral structured mesh was selected. To model the rotating zone MRF technique of the software was used to determine the mean radial, axial, and tangential velocities at every zone. After the process, predictions were made on velocities, impeller pumping capacity, energy dissipation rate, etc. It was concluded that there is a point known as the optimal point having a height of 0.057 m and a diameter of 0.186 in zone 6 where CFD results showed the maximum accuracy with the experimental data on the comparison. It was also noted that the percentages of power and pumper numbers are different in laminar and turbulent regimes. In turbulent regimes, the power number prediction is 25 %, while the pumping number for laminar flow is less than 12 %.

A study performed the polymerization of styrene thermally on two different models of CSTR laboratory scale pitched blade reactors. Both configurations of the reactor differ in the inlet and outlet locations. The parameters studied were the impeller speed and the resistance time at a constant inlet temperature of 140^{o}C for both configurations. Styrene entered from the inlet of the reactor and reacted to produce polymer inside the reactor, and then from the outlet, polymer and some unreacted styrene left the reactor. The resistance time for the reaction is 48 to 144 minutes, and the speed of the impeller varied from 100 to 1000 rpm. Meshing and geometry creation were done by Mix sim 21(Fluent Inc.) and Gambit (Fluent Inc.). The simulations were carried out using Fluent 6.3; multiple reference frames were used to model the impeller speed. After his study, he concluded that when there is low residence time, the reaction area is homogeneous. However, increasing the residence time makes the reaction media more viscous. Here, the values differ in both CFD and CSTR and CFD values lay above CSTR. It was also concluded that the conversion decreased by increasing impeller speed, and the simulation results were in good agreement with the experimental data. As far as the locations of the outlet and inlet are concerned channeling is the main factor that affected the variation in the location of the outlet and inlet. If the inlet and outlet are in the opposite direction, then more mixing and homogeneity will be obtained. In the literature several studies were found related to the CFD software fluent in the multiphase flow fieldbut very rarely discussed that size distribution function of the mixtures dispersed phase. Similarly there was a work present in literature which is not directly related to size distribution but yet gives some information about coalescence and breakage in liquid- liquid systems [54]. A research determined the breakage and coalescence of drops in liquid-liquid extraction regimes. Venturi meter were used to perform this experiment. A toluene/water system was employed to determine the breakage process, while n-butyl acetate/ water was used for the coalescence process. The study showed that diameters less than 2 mm have a higher probability of coalescence than the larger diameter molecules. In this way, the researcher successfully employed the population balance model to do the hydrodynamics measures of the extraction units. In the field of microencapsulation, there has been substantial research focused on the particle size distribution in water-in-oil emulsions. Similarly, the emulsification industry has extensively studied the particle size distribution. However, the specific effect of the high-speed homogenizer's rotational speed on the number density of the particles has not been thoroughly discussed in the literature [55].

The lack of comprehensive understanding of the relationship between the homogenizer's operational parameters and the resulting particle number density represents an opportunity to contribute to the existing knowledge in the field of microencapsulation and emulsification. By addressing this specific aspect, this research work will provide valuable insights and practical guidance for researchers and engineers working on the numerical modeling and optimization of polymer-based particle formation systems. This research work aims to fill this gap by investigating the impact of the high-speed homogenizer's rotational speed on the number density of the particles. The findings from this study will be particularly helpful for beginners and researchersdealing with the numerical modeling of polymers in particle formation processes.

A review of the literature around modeling particle size distribution revealed opportunities to develop a more precise and up-to-date model capable of advancing this research domain. While prior studies provided a foundation, it was apparent that employing a discrete population balance approach within an Eulerian framework could provide novel insights into how particle size varies. Specifically, this integrated technique held promise for gaining a deeper understanding of the influencing factors. Furthermore, an examination of the historical applications of population balance modeling highlighted specific avenues this current project could pursue. After thoroughly assessing past research utilizing such methods, the following scopes and objectives were identified as priorities for the present study to meaningfully contribute new knowledge.

1.6 Scope of Work

From the above literature, it has been shown that computational fluid dynamics is a powerful tool for optimization. We can use this method in microencapsulation processes for maximum accuracy of the results in emulsion making industry. The main focus of this work is to establish a CFD simulation methodology that could yield to particle size distribution of polymer microencapsulation processes in a multiphase system. The scope of the thesis encompassed various aspects related to the CFD study of polymer microencapsulation processes.

This includes:

Fundamental understanding of particle formation: Simulations provide a platform to study the underlying mechanisms governing particle formation, such as nucleation, growth, aggregation, and breakage. Furthermore, by modeling the evolution of the number density function, researchers can gain insights into the key kinetic processes and how they influence the final particle distribution.

Process optimization and scale-up: The number density function obtained from simulations can be used to optimize process parameters, such as residence time, shear rate, and feed composition, to achieve the desired particle characteristics. This information is crucial for the successful scale-up of particle formation processes from the laboratory to the industrial scale, as it helps maintain control over the particle size and number distribution.

Product quality and consistency: The number density function is closely linked to the overall particle size distribution, which is a critical quality attribute for many products, such as pharmaceuticals, cosmetics, and advanced materials. By simulating the number density function, manufacturers can ensure the consistent production of particles with the required size and number characteristics, leading to improved product quality and performance. *Regulatory compliance:* In certain industries, the number density of particles, especially for nanomaterials, is a key parameter that needs to be monitored and reported for regulatory compliance.

Simulations can provide valuable data on the number density function, which can be used todemonstrate compliance with relevant guidelines and standards.

Formulation and process design: The number density function obtained from simulations can guide the development and optimization of formulations, such as the selection of stabilizers surfactants, or other additives, to achieve the desired particle characteristics.

This information can also be used to design and optimize particle formation processes, such as emulsification, precipitation, or spray drying, to meet the specific requirements of the end-use application.

Theoretical and experimental validation: Simulations of the number density function can be used to validate and refine theoretical models and empirical correlations, improving the predictive capabilities of these tools. Comparing the simulated number density function with experimental data can help identify gaps in the understanding of particle formation mechanisms and guide furtherexperimental investigations.

Multiscale modeling and integration: The number density function obtained from simulations can be integrated into larger-scale models, such as computational fluid dynamics (CFD) or process- scale simulations, to provide a more comprehensive representation of the particle-fluid dynamics and its impact on the overall system performance.

By accurately determining the number density function through simulation, researchers and engineers can unlock a deeper understanding of particle formation processes, optimize process design and scale-up, ensure product quality and consistency, and contribute to the overall advancement of particle-based technologies across various industries.

1.7 Objectives of Study

This study had the following objectives at its outset to accomplish the overall goal

- Conduct an analysis of prior research work and pathways through determining the state-of-the-art via literature reviews.
- Determine the particle size of a Polymer (PEI) at varying impeller rotation speeds recording the numerical responses for comparison with experimental findings.
- Validate the particle size distribution of an oil-in-water system by modifying impeller speeds and material densities through juxtaposing numerical simulation outputs against experimental results, as presented in a 2012 paper by Farhad Ein Mozaffari under specified geometric conditions.
- Develop the model with the ability to predict particle size distributions as realistically reflected in experimentation.
- Compare the numerical outcomes with the experimental results for validating the model developed

The overarching aim was thus to analyze, simulate, validate and model such systems, building upon existing literature to further the current understanding.

1.8 Methodology and Structure

This thesis draws upon various research articles that are synthesized. Full details of all references and sources are provided in the references section.

Chapter 1 introduces polymer microencapsulation processes and the simulation of such processes using computational fluid dynamics (CFD). It also outlines the fundamental governing equations and models employed for simulation purposes.

Chapter 2 explains the methodology and experiments. A comprehensive description is presented of the models and parameters utilized in the current project. Experiments are conducted in the polymers and biopolymers department laboratory at UPC and results are organized effectively through graphs and figures to facilitate verification against computational data.

Chapter 3 involves validating the experimental and computational data from Farhad Ein-Mozaffari's 2012 research on the particle size distribution of oils under varying impeller speeds and water volumes. A thorough discussion is given of the parameters from this reference paper, along with a consideration of the successful results comparison achieved through validation.

Chapter 4 presents the implementation of the numerical modeling aspect of the project. Computational simulation is carried out involving PEI, which is then validated against experimental particle size distribution values for polyethyleimine (PEI).

Chapter 5 gives the final conclusions of the thesis along with some recommendations for the upcoming researchers.

References

[1]. Chaturveidi, P.; Sharma, P. A Review on Microencapsulation as Method of Drug Delivery. *BIO Web of Conferences*, **2024**, 86, 01033.

[2]. Wen, J.; Chen, G.; Alany, R. G. Theories and concepts of nano materials, nano-and microencapsulation. *Nano-and Microencapsulation for Foods*, **2014**, 17.

[3]. Domínguez, R.; Pateiro, M.; Paulo E, Julian, D.; Lorenzo, M. Encapsulation of Bioactive Phytochemicals in Plant- Based Matrices and Application as Additives in Meat and Meat Products. *MPDI, Molecules*, **2021**, 26, 3984.

[4]. Gómez, B.; Barba, F.J.; Domínguez, R.; Putnik, P.; Kovačević, D.; Pateiro, M.; Toldrá, F.; Lorenzo, J.M.; Microencapsulation of Antioxidant Compounds through Innovative Technologies and Its Specific Application in Meat Processing. *Trends Food Sci. Technol,* **2018**, 82, 135-147.

[5]. Gao, Z.; Rao, S.; Zhang, T.; Gao, F.; Xiao, Y.; Shali, L.; Wang, X.; Zheng, Y.; Chen, Y.;

Zong, Y.; Li, W.; Chen, Y. Bioinspired Thermal Runaway Retardant Capsules for Improved Safety and Electrochemical Performance in Lithium-Ion Batteries . *Adv. Sci.*, **2022**, 9, 2103796

[6]. Choudhury, C.; Meghwal, M.; Das, K.. Microencapsulation: An overview on concepts, methods, properties and applications in foods. Food Frontiers, **2021**, 2, 426-442.

[7]. Bai, L.; Huan, S.; Rojas, O.J.; McClements, D.J. Recent Innovations in Emulsion Science and Technology for Food Applications. *Journal of Agricultural and Food Chemistry*, **2021,** 69, 8944-8963.

[8]. Dwivedi, K.; Jaiswal. S.; Tiwari, S.; and Verma, N. Microencapsulation; Application and Recent Advances. A Review. *International Journal of Medical and pharmaceutical* research, **2023**, 4, 2958-3675

[9]. Birnbaum, DT.; and Peppas, L. Microparticle drug delivery systems and Drug delivery systems in cancer therapy. *Humana Press Inc*, **2003,** 117–136.

[10]. Spenlehauer, G.; Veillard, M.; Benoit, JP. Formation and characterization of cisplatin loaded poly (d, dlactide) microspheres for chemoembolization. *J Pharm Sci*, **1986**, 75, 750–755.

[11]. Mi, F.; Lin, Y.; Wu, Y.; Shyu, S.; Tsai, Y. Blend microspheres as a biodegradable drug-delivery system: phase-separation, degradation and release behavior. *Biomaterials*, **2002,** 23, 3257.

[12]. Roberts and Taylor. Flavor Release ACS Symposium Series American Chemical Society: Washington, DC, **2000.**

[13]. Benita, S.; Donbrow, M. Effect of polyisobutylene on ethylcellulose-walled microcapsules: wall structure and thickness of salicylamide and theophylline microcapsules. *J Pharm Sci*, **1982**, 71, 205–210.

[14]. Felt, O.; Buri, P.; Gurny, R. A unique polysaccharide for drug delivery. *Drug Dev Ind Pharm*, **1988**, 24, 979–993.

[15]. Fukushima, S.; Kishimoto, S.; Takeuchi, Y.; Fukushima, M. Preparation and evaluation of o/w type emulsions containing antitumor prostaglandin. *Adv Drug Deliv Rev*, **2000**, 45, 65–7.

[16]. Passerini, N.; Craig, D.Q. Characterization of ciclosporin A loaded poly (D, L lactide-coglycolide) microspheres using modulated temperature differ-ential scanning calorimetry. *J Pharm Pharmacol*, **2002**, 54, 913–919.

[17]. Carrasquillo, KG.; Stanley, AM.; Carro, JC.; De Jesus, P.; Costantino, HR.; Bosques, CJ. Non- aqueous encapsulation of excipient-stabilized spray-freeze dried BSA into poly(lactide-co-glycolide) microspheres results in release of native protein. *J Control Rel,* **2001**, 76, 199–208.

[18]. Chaumeil, JC.; Chemtob, C.; Ndongo, M. Tablets of metronidazole microcapsules: release characterization. *Int J Pharm Sci,* **1986**, 29, 83–92.

[19]. Piletti, R.; Zanettib, M.; Jungb, G.; Dalcantonc, F.; Soaresa, C.; Gracher, H.; Márcio, R.; Fioric, A. Microencapsulation of garlic oil by β-cyclodextrin as a thermal protection method for antibacterial action. *Materials Science & Engineering,* **2019**, 94, 139–149.

[20]. Girardi, NS.; García, D.; Robledo, NS.; Passone, MA.; Nesci, A.; Etcheverry, M. Microencapsulation of Peumus boldus oil by complex coacervation to provide peanut seeds protection against fungal pathogens. *Industrial Crops and Products*, **2016,** 92, 93- 101.

[21]. Mirzaei, H.; Pourjafar, H.; Homayouni, A. Effect of calcium alginate and resistant starch microencapsulation on the survival rate of Lactobacillus acidophilus La5 and sensory properties in Iranian white brined cheese. *Food Chemistry,* **2012**, 132, 1966- 1970.

[22]. Yuliani, J.; Torley, B.; Timothy, N. Extrusion of mixtures of starch and D-limonene encapsulated with β-cyclodextrin. Flavour retention and physical properties. *Food Research International,* **2006**, 39, 318-331.

[23]. Ferrero, J.M.; Irache, C.J.; Navarro, G. Soybean protein-based microparticles for oral delivery of probiotics with improved stability during storage and gut resistance. *Food Chemistry,* **2018**, 239, 879-888.

[24]. Basu, S.; Banerjee, D.; Chowdhury, R.; Bhattacharya, P. Controlled release of microencapsulated probiotics in food matrix. *Journal of Food Engineering,* 2018, 238, 61-69.

[25]. Doi, WT.; McClements, J. Encapsulation and controlled release of hydrophobic flavors using biopolymer-based microgel delivery systems: Sustained release of garlic flavor during simulated cooking. *Food Research International.* 2019, 119, 6-14.

[26]. Breternitz, N.; Bolini, M.; Hubinger, M. Sensory acceptance evaluation of a new food flavoring produced by microencapsulation of a mussel (Perna perna) protein hydrolysate. *Food science and technology*, 2017, 83, 141-149.

[27]. Wyspiańska, D.; Kucharska., A. Effect of microencapsulation on concentration of isoflavones during simulated in vitro digestion of isotonic drink. *Food Science and Nutrition*, **2019,** 7, 805- 816.

[28]. Agnihotri, N.; Mishra, R.; Goda, C.; Arora, M. Microencapsulation – a novel approach in drug delivery: a review. *J. Pharm. Sci*, **2012**, 2, 1-20.

[29]. G, Ma. Microencapsulation of protein drugs for drug delivery: strategy, preparation, and applications. *J. Control. Release*, **2014,** 93, 324-340.

[30]. Senthil, T., & Ramesh, S. Microencapsulation of phase change materials for thermal energy storage: A review. *Renewable and Sustainable Energy Reviews*, **2017**,70, 1053-1071.

[31]. Rangari, V. K., & Jeelani, S. Encapsulation of biocides in textiles for protection againstbio- contamination. *Textile Research Journal,* **2014**, 84, 1, 67-78.

[32]. Vishalakshi, B. Microencapsulation of agrochemicals for controlled release applications: A review. *Journal of Environmental Science and Health, Part B*, **2017,** 52, 5, 348-356.

[33]. Gaur, T.; a nd Sood, A. Particle Size and Particle Size Distribution of Emulsion Polymers. *Journal of Chemical Engineering Research Updates.* **2020,** 7, 16-23.

[34]. Xing, C.; Wang, T.; Wan, J. Experimental study and numerical simulation with a coupled CFD–PBM model of the effect of liquid viscosity in a bubble column. *Chemical Engineering Journal*. **2013**, 95, 313-332.

[35]. Anderco, B.; Andersoson, R.; and Mortensen, M. Computational Fluid Dynamics for Engineers, *Rehman Sudiyo press*, **2012**.

[36]. Rohr, A. A Computational Fluid Dynamics (CFD) analysis of the Aerodynamic effects of the Seams on a two-dimensional Representation Of a soccer Ball. *Polytechnic State University*, **2018.**

[37]. Hong, S.; Asai. A.; and Seo, K. Visualization of Air Flow Around Soccer Ball Using a Particle Image Velocimetry, *Scientific reports,* **2015.**

[38]. Anderson, J. Computational Fluid Dynamics. *International Edition*, 1995 .

[39]. Ansys Fluent **2020**. Theory Guide. *Ansys Inc*.

[40]. Wilcox, D. C. Turbulence Modeling for CFD (4th e d.). *DCW Industries, Inc*, **2021**.

[41]. Versteeg, H. K., & Malalasekera, W. An Introduction to Computational Fluid Dynamics: The Finite Volume Method (3rd ed.). Pearson. **2020**.

[42]. Durbin, P. A., & Reif, B. A. Statistical Theory and Modeling for Turbulent Flows (3rd ed.). John Wiley & Sons. **2021**.

[43]. Roudsari, S.; Experimental and CFD Investigation of the Mixing of MMA Emulsion polymerization in a Stirred Tank Reactor. PhD thesis submitted to Ryerson University, **2015.**

[44]. Guelfi, A.; & Hunt, G. R. An Eulerian modeling approach for multiphase flows. *Annual Review of Fluid Mechanics*, **2018**, 50, 1-27.

[45]. Yen, W.; Asako, Y, & Rui-Zher, G. Governing Equations in Computational Fluid Dynamics: Derivations and A Recent Review. *Progress in Energy and Environment*, **2017,** 1, 1 1 – 19.

[46]. Roudsari, S.; Turcotte, G.; Dhib, R.; and Mozaffari, F. CFD modeling of mixing of water-in-oil emulsions. *Computers and Chemical Engineering*, **2012**, 45, 124-136.

[47]. Roudsari, S.; Experimental and CFD Investigation of the Mixing of MMA Emulsion polymerization in a Stirred Tank Reactor. *PhD thesis submitted to Ryerson University.* **2015**

[48]. Patil, A.; & Johansen, T. Computational and experimental study of oil-water emulsion Flow and stability in a stirred tank. *International conference on CFD in minerals and process industries. CSIRO*, **2015**.

[49]. Agertof, W.G.M.; Vaessen, G.E.J.; Haag, G.A.A.V.; Klahm, J.K.; Janssen J.J.M. Prediction of emulsion particle sizes using a computational fluid dynamics approach. *Colloids and surfaces B: Biointerfaces*, **2003**, 31, 141-148.

[50]. Raikar, N.; Bhatia, S.; Malone, M.; & Henson., M. Experimental studies and population Balance Equation model for breakage prediction of emulsion drop size distributions. *Chemical Engineering Science*, **2009**, 64, 2433-2447.

Chapter 2

Integrating Experimental Methodology and Simulation for Particle size Distribution

2 Overview

This chapter outlines the methodology and experimental work conducted as part of the current research study. A multi-pronged approach was adopted involving both laboratory experiments and numerical simulation. Computational simulations were completed using the Ansys Fluent software package (R2 2020 release).This hybrid methodology leveraged the benefits of experimental and computational work, conducted under the auspices of esteemed faculty in the relevant fields.

2.1 Apparatus and chemical Essentials

The key laboratory equipment and materials involved in the experiments were:

- A Turrax agitator for emulsification and mixing of samples (S18N- 19G, IKA)
- Injecting syringes to withdraw and insert liquids into the reactor
- A SORVALL RC 5B Plus centrifuge to separate phases
- A TELSTAR lycoquest freeze dryer for drying processes
- SEM imaging equipment for particle size detection and analysis
- Beakers for holding or transferring liquids
- Nano sizer model 90 Plus –zeta (Brookhaven, USA) to measure the particlessizes
- Magnetic stirrers and plate shakers for mixing at various intensities
- The primary substances used were: Dispersed phase (Polyethyleneimine (PEI) polymer in 10ml of dichloromethane) and Continuous Phase (Polyvinyl alcohol (PVA) in 90 ml of water).

2.2 Experimental Setup

The experimental setup consisted of a beaker containing a polyvinyl alcohol (PVA) solution with a turrax agitator installed. Polyethyleneimine (PEI) was used as the dispersed phase and was added to the PVA solution from the top of the beaker. Initially, the speed of the impeller was adjusted to stabilize the apparatus. Then, the impeller speed was systematically increased to 5000, 7500, 10000, 12000 and 15000 revolutions per minute (rpm). These different impeller speeds were tested to observe the effect on the particle size distribution of the PEI dispersion within the PVA solution. The goal was to determine how increasing the impeller speed impacted the particle sizes achieved through the emulsification process. Figure 2.1 represents the schematic assembly of the apparatus used in the experimental part of the project.

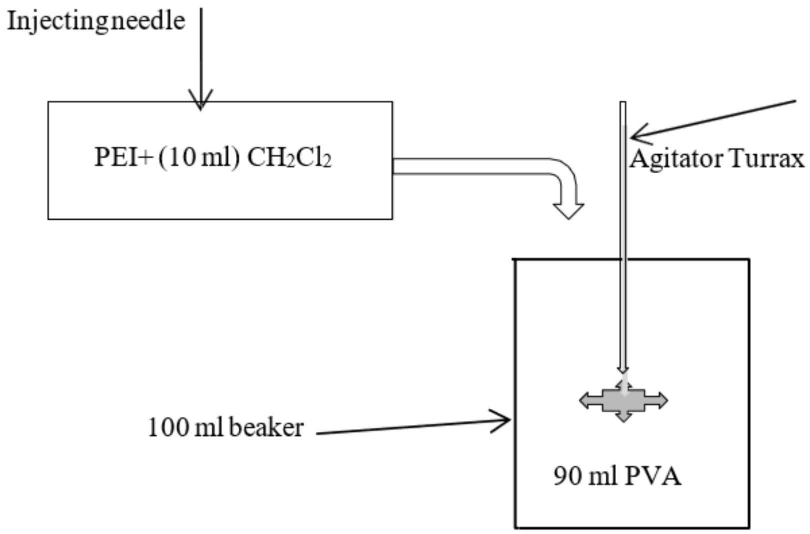

Figure 2.1 Schematic diagram of experimental setup

2.3 Experimental Procedure

2.3.1 Sample Preparation

The experimental procedure began by preparing various samples of dispersed phase (PEI) dissolving in dichloromethane. A 20% w/v PEI sample was prepared by adding 2 gm of PEI in 10 ml of dichloromethane; this prepared solution underwent a 24-hour process of shaking for homogeneous mixing to become suitable for the experiment. Similarly 1% w/v of PVA solution was prepared.

2.3.2 Introducing Phases

Polyvinyl alcohol (PVA) was used as a continuous phase while PEI used as a dispersed phase. The experimental setup started by placing 90 ml of PVA in a beaker installed with a Turrax Agitator and PEI (dispersed) phase was introduced from the top of the beaker through a syringe. To ensure that the PEI do not stuck to the bottom of the beaker, the impeller was started at the lowest allowable speed to induce turbulence in the sample.

2.3.3 Impeller Speed Variation

After achieving the stabilized phase of the mixing domain inside the beaker, the rotational velocity of the impeller was adjusted to 5000 rpm. The flowrate of the dispersed phase was adjusted to 0.33ml/min through an injecting needle to make sure the efficient microencapsulation process. This flowrate took half an hour to complete the dispersion of PEI into the PVA. The microencapsulation process was completed here. Then the impeller speed was varied from 5000 rpm, 7500 rpm, 10000 rpm, 12000 rpm and 15000 rpm and the same procedure was repeated to have the particle size distribution.

2.3.4 Washing and Drying of Capsules

After the microencapsulation process, the solution of PVA and PEI was washed in a SORVALL RC 5B plus centrifuge for 2-3 times. After that a few drops of the processed sample were placed on specimen mounts made of aluminum and then stored in a box. The samples were put at -80 ° C for 24 hours and the frozen sample were dried in freeze dryer using a TELSTAR Lyco Quest apparatus.

2.3.5 Scanning Electron Microscope (SEM) and Dynamic Scattering Light (DSL) images

SEM images were used to take qualitative data on the morphology and size of the prepared particles. DSL technique performed to calculate the sizes of the particles at particular impeller speed. Finally the data was analyzed and plotted and the model was developed as discussed in the next sections.

2.4 Description of the Turrax Agitator used in the Rresearch

As it is explained in the introduction section that the production of microspheres are highly dependent on the agitation speed of the impeller. The impeller used in current study was Agitator Turrax T18, manufactured by a company IKA (Germany). This is one of the best devices used to induce turbulence for creating smaller sized microcapsules. This agitator have rotor and stator mounted in each other rotor is a moving part while stator is stationery. Due to its unique geometry it has become one of the powerful devices to be operated at high speed. This device is very common and also used at a domestic level to produce emulsions and mixture used in daily life. Hence the importance of the rotor stator homogenizer is very clear. This is one of the reasons to use this industrial rotor-stator device in our study to produce as smaller particles as possible in the lab scale equipment. The main purpose of Turrax agitator is to produce as fine particle as possible.When this agitator dips in the mixture for two immiscible phases there created an interface between the fluid of rotor and stator so in this study we will discuss the particle production in the interface of rotor- stator. To understand the behavior of agitation speed of this homogenizer on the microparticle, it should be clear that the turbulence creates shear and thus allow the fluid to move away from the center, thus producing double shear effect on the fluid. Figure 2.2 represents the assembly of the agitator that consists of the arm of an external ring of static blades, referred to as the stator. Within the stator is a central shaft that rotates solidly with the Turrax motor. Affixed to this inner shaft are several mobile blades that make up the rotor.

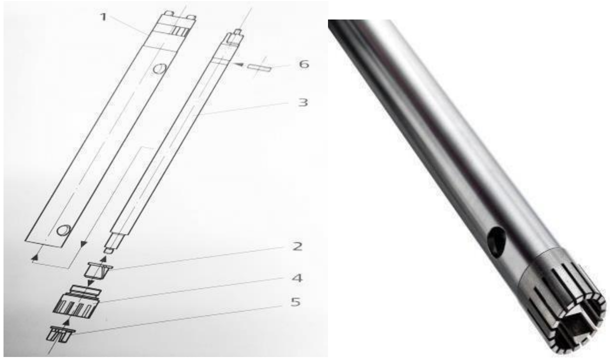

(a) (b)

Figure 2.2 Agitator assembly (a) parts of the dispersion tool, 1) shaft tube, 2) grooved piston, 3) shaft, 4) stator and 5) rotor. (b) Turrax homogenizer.

The design of the agitator arm plays a key role in the success of the microencapsulation experiment. Careful analysis of the arm's configuration is necessary to understand how it will impart shear on the emulsion. In this study, the IKA S18N-19G model agitator was used.

2.5 Description of Fluid Dynamics Created by the Counter Rotating Rotor and Stator

As seen in Figure 2.3, through the rotation, the rotor creates both a fluid flow outward and a primary shearing effect on the emulsion. Once sheared initially, the fluid exits between the rotor and stator blades. At this point, the fluid passes through the fixed stator blades and undergoes shear stress again.

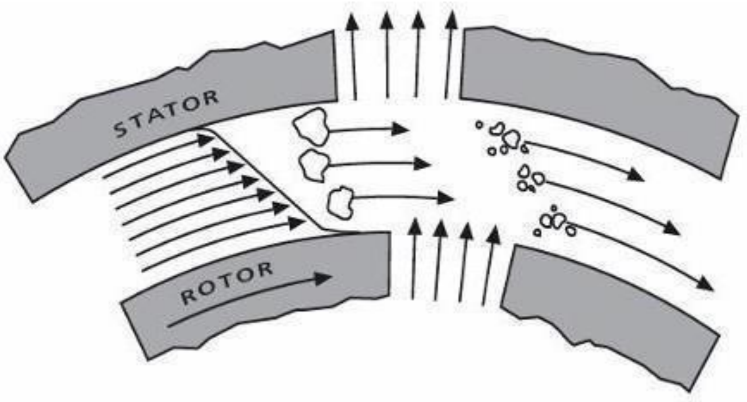

Figure 2.3 Description of phenomenon taking place inside Rotor-stator

Together, the interacting rotor and stator geometries accomplish a double shearing of the fluid flow. First, the rotor blades impart shear as the emulsion is drawn toward the outer edge of the arm. Then, as the fluid is pushed out, the stator blades induce shear in the opposite direction. Beyond the dual shearing action, this agitator arm design also provides a powerful agitation effect, more so than a typical magnetic stir plate and stir bar setup. Dueto its ability to impart both strong agitation and double shear forces, this IKA Turrax model is well-suited for the microencapsulation process. The use of high-pressure homogenization during emulsion formation led to significantly improved microencapsulation results. Emulsions processed with homogenization at pressures up to 500 bar exhibited both smaller particle diameter and higher stability compared to non- homogenized emulsions. Specifically, the average diameter was reduced to 3 μm versus over 10 μm without homogenization [1].

Homogenization also enhanced the encapsulation efficiency and oil retention capacity of the microcapsules. Encapsulation efficiency, which indicates the percentage of core material successfully confined within the coating, was measured to be over 95% with homogenization. In contrast, non- homogenized emulsions showed an efficiency below 80%. Similarly, oil retention after two months of accelerated storage was nearly 90% for homogenized particles but less than 70% for those made without applying high-pressure shear forces. The mechanical stresses induced during homogenization were theorized to facilitate formation of stable, miniaturized emulsion droplets with compact coating layers. This conclusively demonstrated that applying high pressure homogenization results in microencapsulation systems with drastically superior characteristics, including smaller particle sizes, higher encapsulation of the core material, and improved retention of encapsulated contents over time.

2.6 Efficiency of Turrax Agitator

Efficient mixing and dispersion: Turrax agitators are known for their ability to efficiently mix and disperse various substances, including liquids, solids, and powders. They can quickly and effectively break down agglomerates, disperse particles, and create homogeneous mixtures.

Versatility: Turrax agitators are versatile and can be used in a wide range of applications across different industries. They are commonly employed in chemical, pharmaceutical, food, and cosmetic industries for processes such as blending, emulsifying dissolving, and wetting. Time and cost savings: Turrax agitators offer fast and efficient mixing capabilities, allowing for reduced processing times. This can lead to cost savings by increasing productivity and reducing overall production time.

Scalability: Turrax agitators are available in various sizes and configurations, making them suitable for both laboratory-scale and large-scale industrial applications. They can be easily scaled up or down to match the desired production volume.

Process optimization: Turrax agitators enable process optimization by ensuring consistent and repeatable results. By achieving thorough mixing and dispersion, they help improve product quality, increase yield, and enhance overall process efficiency.

Easy operation and maintenance: Turrax agitators are generally user-friendly and require minimal training to operate. They are designed for easy cleaning and maintenance, which helps reduce downtime and ensures reliable performance.

Widely available: Turrax agitators are manufactured by different companies and are readily available in the market. This accessibility makes them a popular choice for industrial applications. Table 2.1 depicts the specification of the Turrax agitator used in the experimentation ofproducing microcapsules.

Table 2.1 Specifications of Turrax

Voltage	200-240 ±10% Vac
Rated Voltage	230 Vac
Hz Frequency	50/60
Powe consumed	500 W
Power supplied	300 W
Velocity range	3.000-25.000
Permissible room temperature	+5...+40 ºC
Dimensions	65x106x271 mm

2.7 Properties of the Materials

Polyetherimide (PEI)

PEI was used as a dispersed phase. It is a semi-crystalline thermoplastics polymer. It has a density of 1.3 g/cm^3. These particles are produced by solvent evaporation.

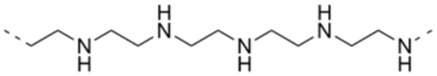

Polyvinyl alcohol (PVA)

PVA is a water-soluble artificial polymer with the chemical formula $(C_2H_4O)_n$. It has a density of 0.998 g/cm^3. The low viscosity of the PVA solution approaches water while providing stabilization of the PEI microparticles in contradiction of aggregation.

$$[-CH_2-CH(OH)-]_n$$

Properties Used in Simulation The above experimentally determined density values for solid PEI and liquid PVA solutionwere directly applied in the computational model. The material properties were assumed constant with respect to operating conditions and particle size effects for initial model validation. Table 2.2 shows the densitie sand viscosities of continuous and dispersed phase defined in the software.

Table 2.2 Materials properties used in the solver was mentioned in the table

Materials	**Density(kg/m^3)**	**Viscosity (kg/m.s)**
PEI	1332.7	0.321
PVA	998	0.00102

2.8 Computational Fluid Dynamics Approach

Ansys Fluent R2 2020 software was used to develop the computational model. Different codes of CFD are available for multiphase modeling. Computational fluid dynamics uses different approaches to achieve the best results. It is based on governing equations operated under methods and model. Some of the basic information regarding governing equations is described in the introduction part of the thesis and these equations are bases for the finite volume formulations in different phenomenon of fluid flow. In this chapter methods and models of CFD are discussed which are responsible for predicting particle size. CFD simulation is based on two basic steps (a) pre-processing and (b) post-processing.

2.8.1 Pre-Processing

Geometry Creation of a System

For the Simulation of particle size distribution in the reactor we used Ansys Fluent Package 2020 R2 and all the transport equations were solved with discrete method in Population balance modeling. The geometries of rotor and stator inside the reactor were generated by design modular tool available in the Ansys Fluent in sketching mode shown in Figure 2.4. The first step in performing the multiphase flow simulations was to define the computational domain and generate the mesh. The dimensions and geometry of the experimental vessel were accurately replicated.

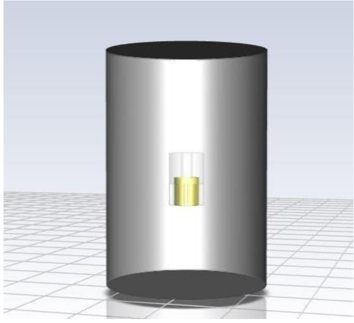

Figure 2.4 Geometry of the system sketched on design modular of ANSYS fluent 2020 R2

Geometry Creation of Turrax Agitator

In Figure 2.5, we can observe the rotor-stator geometries created in ANSYS design Modular, illustrating the arrangement of the rotor (inside) and stator (outside) components for the agitator assembly.

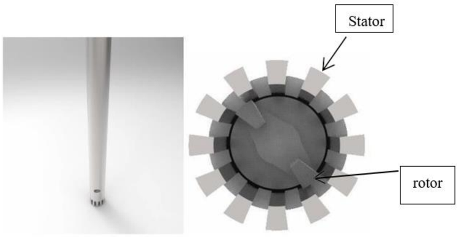

Figure 2.5 Geometry of the rotor and stator part of the agitator sketched on design modular of ANSYS fluent 2020 R2

Mesh Generation

A size function was done by meshing technique present in the Ansys Software. The mesh considered in this study was fine enough between the rotor and stator interface which is the point of interest in this study to capture the size distribution of the droplets properly. Tetrahedral mesh considered for the modeling is shown in the Figure 2.6 (a, b) which gives mesh of the stator and rotor part of the impeller. An unstructured mesh consisting of 16696480 tetrahedral elements was generated to discretize the domain as shown.

Figure 2.6 Tetrahedral mesh of (a) stator and (b) rotor

Mesh Independence Study

Several test simulations were run to validate the CFD setup against experimental observations and ensure mesh-independent solutions. Key output parameters that characterize the flow field were monitored for each mesh, such as velocity magnitudes, pressure drops, mass flowrates, etc. The coarse, standard, and fine meshes were run under identical inlet and boundary conditions. The results from the three grids were compared to assess convergence. The percent difference in maximum velocity between the standard and fine mesh was less than 1%. Based on these results, it was concluded that the solution was grid-independent, as further refinement caused negligible change in flow quantities. The computational expense of the fine mesh was also significantly higher, requiring over 40% more computational time. Therefore, the selected mesh shown in Figure 2.7 balancing accuracy and computational cost was selected for all subsequent production simulations. Mesh independence was verified to ensure any variation in results is due to real physical changes in parameters rather than numerical factors related to grid resolution.

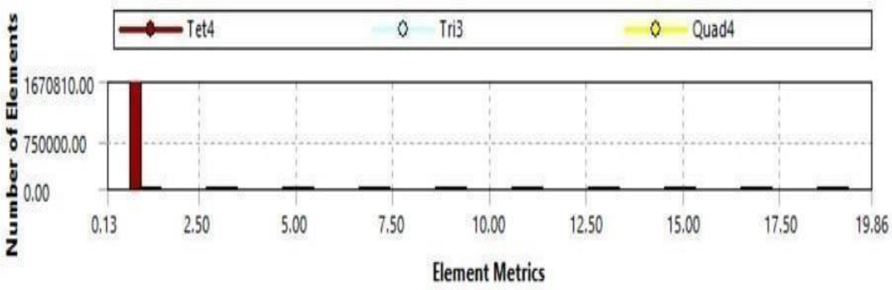

Figure 2.7 Mesh Quality of stator

Boundary Conditions

Boundary conditions were then specified, such as setting the liquid volume fractions to define the dispersed and continuous phases and imposing no-slip conditions on walls. The equations of continuity and momentum were derived based on the VOF framework, along with relevant sub-models for surface tension, interfacial drag, and turbulence by using the k-ε realizable model. The solver was configured to utilize a Second Order Implicit scheme for time-advancement and the geometric reconstruction scheme was chosen to sharpen the interface. Mostly in the boundary conditions we used the rotor and its associated features as a moving parts and stator and its associated interface as a stationary part. All the modeling is based on these boundary conditions.

2.9 Approaches of CFD (Ansys Fluent 2020 R2) used in this Project

2.9.1 Turbulent Models

Turbulence is the result of variations in the flow velocity, if the flow is moving under 2300 rpm then the Reynolds number is laminar and if this value exceeds from 4000 rpm then the flow is considered to be the turbulent flow. To determine the turbulent conditions inside the area of interest is a difficult task [2]. To choose the turbulent model for representing the physical conditions of the experiment is the sensitive action to do [3]. To capture the turbulence inside the microencapsulation domain in our study we used realizable k-e turbulent model. The recent study by [4] discovered that realizable k-e is far better choice for turbulent model than standard k-e and standard k-omega. In another study by [5] discovered that the realizable k-e is the best methods from standard k-e and standard k-omega for characterizing the flow during the process domain.

2.9.2 Multiphase Model

In the current project, the implicit scheme of the Eulerian approach is used due to its high stability concepts of capturing the flow features rather than the explicit approach [6] established an implicit system for Eulerian multiphase equations in ANSYS Fluent. In multiphase models where complexity is involved implicit behavior of Eulerian to solve the equations is more accurate than in explicit so bytaking these factors under consideration and by taking the physics involved in the process into account we decided to use the implicit scheme of the Eulerian model which satisfied the need of experimental results Population Balance model (PBM) Several methods come under population balance model (PBM). We must choose the method according to the problem statement. In this current study discrete method of PBM was used. The particle diameters obtainedin our experimentation resemble the S-shaped curve, so we used the discrete method of Population Balance Model. Generalized form of equation of Population Balance. Modeling by [7].

$$d/dt\int \Omega z(t)dVx \int \Omega r(t)dVr \int (x,r,t) = \int \Omega z(t)dVx\int \Omega r(t)dVr\ h(x,r,Y,t) \tag{2.1}$$

The discrete method of Population Balance Models was used to predict the sizes of particles. We defined 5 numbers of bins to save computational time and it gives the similarity difference of less than 10 % of the number density functions. The multiphase system was modeled by Eulerian approach. There are some forces like surface tension and wall adhesion along the interface which needs to be covered in eulerian framework. Generally surface tension is considered in eulerian model which contains two forces continuum surface force (CSF) and continuum surface stress (CSS). In CSS the force is conservative while in CSF it is not. In the current study eulerian method is used by introducing two phases and set of equations were solved to model the interface. The eulerian multiphase approach tracks the entire particles domain numerically [7].

2.9.3 Breakage and aggregation kernel of Discrete PBM

In our study luo’s model for breakage was used because luo’s predicted the breakage model for separation of particles in the microencapsulation region. [8,9] The breakage term as

$$B(x) = \lambda(x)\, P(x) \tag{2.2}$$

Where λ(x) is breakage frequency function demonstrating collisions and P (x) is the breakageprobability function reliant on particle properties. In the study also suggested values for empirical constant and turbulent kinetic energy as

$$\lambda(x) = kE\lambda \tag{2.3}$$

Where k is empirical constant, E is the turbulent kinetic energy, and λ is an exponent typically 0.5

$$P(x) = 1 - exp\,[-\,(\sigma/\rho x)\hat{}m] \tag{2.4}$$

Where σ is the induced turbulent stress, ρ is particle density, x is size, and m is the Weibull modulus. Turbulent Aggregation Kernel for the Particle aggregation was demonstrated by means of a turbulent velocity gradient kernel [9].

$$K(x,y) = 2\pi(x + y)(\alpha u\, *)f(x,y) \tag{2.5}$$

where α is the gathering competence, u* is the turbulent velocity, and f(x, y) accounts for hydrodynamics. This kernel captures turbulent eddies linear to u*. Transient simulations were carried out in the current project because according to study transient simulations are found to be the better choice for predicting experimental data as compared to steady state simulations [10].

2.9.4 Multiple Reference Frame

The Multiple Reference Frame (MRF) approach was employed to capture the effects of impeller rotation, as it requires less computational resources than other techniques like sliding mesh. MRF is used for the rotating components of the domain in CFD, it yields results in reasonable time compared to expensive methodologies [11]. The simulated velocity values showed close agreement with experimental impeller speed, validating the use of MRF. This model choice depends on fulfilling physical and computational needs.

2.9.5 Simulation Settings

Table 2.3 gives the settings used in the fluent solver to converge the solution faster and accurate all the settings are used by taking into account the limitations available in the literature. Few values are obtained by hit and trial method and under these conditions fluent gave the accurate answer for the defined bins particle sizes. Table 2.3 shows all the necessary information to run the simulation for a faster converged solution. First-order upwind differencing discretized the momentum and continuity equations. An aggregation kernel turbulence model delivered satisfactory accuracy efficiently. Five particle size bins tracked dispersion. The transient simulation utilized 600 and 1000 number of time steps for different cases. The time step size of 0.0098 seconds each was selected in such a way that it gives converged and accurate solution within less time. Simulation was run for 20 and 30 iterations per step for convergence in specific condition. Solutions finalized within 24 hours, closely matching experiments. Stringent convergence criteria and hardware resources ensured quick yet reliable solutions. Overall, the methodology selection balanced accuracy, stability and computational expense to validate the simulation against physical data.

Table 2.3Settings of the solver

Number of time steps	600
Max iterations/time steps	20
Time step size	0.0098
Discretization methods	First order up-winds
Adaption rotor-stator interfaceregion	Cycles 3
PEI bins under-relaxationfactor	0.5
momentum	0.5
TKE (under-relaxation factor)	0.8

TDR (dissipation rate)	0.7
pressure	0.3
Aggregation kernel	Turbulent model
Breakage kernel	Luo model
Multiphase	Eulerian implicit
Population balance model	discrete
No of bins	5
Ratio Exponent	1
Convergence Criteria	0.01
Turbulent Model	Realizable k-e

2.9.6 Adaption

Adaption during the ANSYS Fluent simulation run refers to the process of automatically refining or coarsening the computational mesh based on certain criteria to improve the accuracy and efficiency of the CFD analysis. The implications of adaption and the impact of adaption cycles on the simulation results can be summarized as follows:

Improved Accuracy: Adaption allows the mesh to be refined in regions of the domain where the flow features or gradients are more complex or require higher resolution [12]. By dynamically adapting the mesh, the simulation can capture critical flow phenomena with greater accuracy, leading to more reliable results [13].

Mesh Refinement: mesh refinement only in the areas of interest, rather than using a uniformly fine mesh throughout the domain [14]. This can significantly reduce the overall computational cost of the simulation, as fewer cells are required to achieve the desired level of accuracy [15].

Adaptive Mesh Refinement (AMR): ANSYS Fluent offers various adaption techniques, such as solution-based adaption, where the mesh is refined based on criteria like velocity gradients, pressure gradients, or other flow variables [16].The adaption can be performed either automatically during the simulation or manually by the user, based on the specific requirements of the problem [17].

Adaption Cycles: The number of adaption cycles, or the frequency of mesh updates, can affect the efficiency and accuracy of the simulation results [18]. More frequent adaption can lead to a better representation of the flow features, but it may also increase the computational time and complexity of the simulation [19]. The optimal number of adaption cycles depends on factors such as the complexity of the flow, the required level of accuracy, and the available computational resources [20].

Convergence and Stability: Adaption can impact the convergence and stability of the numerical solution, as the changing mesh can introduce additional sources of error or instability [21]. It is important to monitor the convergence criteria, residuals, and other relevant metrics to ensure that the adaption process does not compromise the overall stability and reliability of the simulation results [22].

2.10 Post-Processing Tool of CFD

Following the completion of pre-processing simulations, post- processing analysis was conducted. The CFD software Tecplot was used to both quantitatively and qualitatively examine simulation results. Phase volume fractions were quantitatively analyzed through contours, allowing observation of interfacial dynamics over time via animation tools. This facilitated close investigation of droplet breakup, coalescence and flow patterns under varying operating parameters.

2.10.1 Key Post-Processing Steps Included

- Computing the number density function to track particle distributions Generating contours of velocity magnitude at different impeller RPMs to visualize flow speed variations
- Plotting velocity vectors to illustrate flow profiles and directions
- Developing contours of number densities at varying RPMs to examine how particle

concentrations changed with agitation intensity, by applying these targeted post-processing techniques, important fluid mechanical and particle dispersion phenomena could be explored and interpreted in detail. The analysis provided valuable insights into how the multiphase system responded to changed experimental conditions.

2.11 Observation in form of Contours and Vectors

A key strength of CFD simulations is the ability to generate insightful visualizations of flow fields through contour plots and vector diagrams. These graphical representations serve to both qualitatively and quantitatively validate the modeling approach. Some notable results visualized in this study include:

2.11.1 Contours

Contours in Cross-sectional views highlighting regions of highest speed emanating from the impeller tip Surface plots depict swirling flow profiles initiated by the impeller blades.

2.11.2 Vectors

Vectors in Blade region illustrations verifying formation of solid body rotation. Top view confirming bulk recirculation patterns within the vessel.

2.11.3 Particle Number Density Function

Spatial distribution of number density plots for varying size fractions at different RPMs Accumulation "hot spots" correlated to high shear locales. Through such post-processing techniques, detailed insights into complex internal flows and dispersion phenomena were attainable. The close match with theoretical expectations served to fundamentally validate the reliability of the CFD framework in modeling this multifaceted system. The informative visuals play a key role in enhancing Comprehension of simulation results.

References

[1]. Manual of agitator, IKA designed for scientists. T 18 digital ULTRA-TURRAX.

[2]. Tajnesaie, M.; Nodoushan, EJ.; Barati, R.; & Moghadam, MA.; Performance comparison of four turbulence models for modeling of secondary flow cells in simple trapezoidal channels. ISH J Hydraul Eng, **2018**. 26, 187-197.

[3]. Kheirkhah Gildeh H. Numerical modelling of thermal/saline discharges in coastal waters. University of Ottawa, Ottawa, Canada. **2013.**

[4]. Shaheed, R.; Mohammadian, A.; Kheirkhah, H. A comparison of standard k–ε and realizable k–ε turbulence models in curved and confluent channels. Environmental Fluid Mechanics, **2019**. 19, 543-568.

[5]. Reza, M.; Tormey, D.; McGranaghan, M. A comparison of RANS models used for CFD prediction of turbulent flow and heat transfer in rough and smooth channels, **2023**. 20, 100399.

[6]. Frank, M.G.; Paul S.R.; Reynolds, A.J. The influence of impeller design on nano emulsion production. Chemical Engineering Science, **2002**. 13 2649-2655

[7]. Ramakrishna, D. Population Balance: Theory and Application to Particulate Systems in Engineering. Academic Press, **2000**.

[8]. Luo. Methodology for characterization of emulsification using impinging jet mixers.*Journal of Colloid and Interface Science*, **1996**. 183, 2, 559-567.

[9]. Smoluchowski, M. Mathematical Theory of the Kinetics of the Coagulation of Colloidal Solutions. Zeitschrift für Physikalische Chemie, **1917**. 129-135

[10]. Tamburini, S. Impact of impeller tip speed on the breakage and coalescence rates in an agitated vessel. Chemical Engineering Science, **2013**. 91, 102-111.

[11]. Yang, F.; Chen, X.; Su, Y.; Shuai, P. & Cheng, P. CFD simulation and experimental validation of flow field characteristics in stirred tank with single Rushton turbine using Multiple Reference Frame approach. Chemical Engineering Research and Design, **2020**. 163, 126-139.

[12]. Blazek, J. Computational fluid dynamics: principles and applications. Butterworth-Heinemann. **2015**.

[13]. Ferziger, J. H., & Perić, M. Computational methods for fluid dynamics. Springer Science & Business Media, **1997**.

[14]. Hirsch, C. Numerical computation of internal and external flows: The fundamentals of computational fluid dynamics. Butterworth-Heinemann. **2007**.

[15]. Issa, R. I. Solution of the implicitly discretised fluid flow equations by operator- splitting. Journal of Computational Physics, **1986**. 62, 1, 40-65.

[16]. Patankar, S. V. Numerical heat transfer and fluid flow. CRC press, **1980.**

[17]. Versteeg, H. K., & Malalasekera, W. An introduction to computational fluid dynamics: the finite volume method. Pearson Education, **2007**.

[18]. Wilcox, D. C. Turbulence modeling for CFD (Vol. 3). DCW industries, **2006**

[19]. Bani Hashemi, H., Ghaemi, S., & Nobes, D. S. Adaptive mesh refinement in ANSYS Fluent for jet impingement heat transfer. International Journal of Thermal Sciences, **2018**. 130, 342-352

[20]. Ozdemir, B., Ozdemir, B. A., & Karaca, F. Adaptive mesh refinement in ANSYS Fluent for the simulation of fluid flow and heat transfer in a porous media. International Journal of Heat and Mass Transfer, **2019**. 137, 1178-1191.

[21]. Koca, R., & Akilli, H. Adaptive mesh refinement in ANSYS Fluent for the numerical simulation of flow and heat transfer around a circular cylinder. Heat Transfer Engineering, **2020**, 41, 19, 1619-1635.

Chapter 3

Empirical Validation and Performance Assessment for Software- Assisted particle size distribution

3 Introduction

The validation of research findings is a crucial step in the successful completion of a PhD thesis, as it ensures the credibility and reliability of the presented work. In this chapter, we focus on validating the computational fluid dynamics (CFD) simulation approach used to model the emulsion making process and determine the particle size distribution of the droplets formed. The CFD simulations were performed using the ANSYS Fluent 6.3.26 software, a widely-recognized computational platform for fluid dynamics analysis. By rigorously validating the accuracy of the CFD model in predicting the droplet size distribution, we can establish confidence in the reliability of the key findings presented in our research. This introductory section sets the stage for the reader, highlighting the importance of validation and providing a concise overview of the specific validation efforts that will be covered in the chapter. It also introduces the simulation tools used, which lays the foundation for the detailed methodology that will follow.

To validate the findings from the CFD simulations, a comparison with experimental work presented in the literature was conducted. Specifically, the study [1] provided relevant data for comparison. Their work experimentally investigated a water-in-oil emulsion consisting of water as the dispersed phase and two different oils as the continuous phase, inside a cylindrical tank equipped with a Rushton turbine impeller. A computational modeling approach was also adopted by Fathi Roudsari et al. (2012) to simulate the system over a range of impeller speeds from 300, 400 and 600 rpm. By directly matching simulation results against this peer- reviewed experimental investigation, which spanned various agitation intensities, validation of the present numerical work could be performed.

In the article the author employed an Eulerian multiphase framework with the standard k-ε turbulence model in ANSYS Fluent version (16.3.26). A discrete population balance model using 7 discrete size bins and Luo breakage-aggregation kernels described the particle size distribution. They reported cumulative size distributions and log of number densities from simulations at different impeller speeds. While Fathi provided useful preliminary validation of the particle size trends, they only presented limited averaged results. To gain deeper insight, contours and vector plots are needed to examine spatial variations in number densities across the domain for each particle size class at varying impeller speeds.

In this chapter, vectors and contour maps are generated from the simulation data and analyzed. This allows visualizing the dynamic phenomena influencing particle size distributions within different regions of the mixing tank under changing hydrodynamic conditions. The approach aims to supplement the prior study with additional spatial information missed previously. Comprehensive comparisons are then made to the available experimental data for rigorous validation. It must be added that results obtain from simulation were observed and compared with the simulation work done by Fathi Roudsari, 2012. at the impeller zones of the mixing domain and got a very good reliability and agreement between a ANSYS Fluent version (16.3.26) and the version (2020 R2).

3.1 Validation Methodology

3.1.1 CFD Mathematical Approach

In the study of article, the Eulerian approach was engaged to model the multiphase flow inside the emulsion cell. This technique resolves a set of continuity and momentum equations [2] for each phase. The continuity equation for phase q is

$$1/\rho q(\partial/\partial t(\acute{\alpha} q\rho q)\ +\ \nabla\cdot(\acute{\alpha} q\rho quq)\ =0 \qquad 1)$$

where ρ_q is density of phase q, ¿q is the volume fraction of phase, and u_q is the velocity of phase q. The momentum equation for phase q is

$$\partial/\partial t\,(\acute{\alpha} q\rho quq)\ +\ \nabla\cdot(\acute{\alpha} q\rho ququq)\ =\ -\acute{\alpha} q\nabla p\ +\ \nabla\cdot \mathrm{T}q\ +\ \acute{\alpha} q\rho qg+\ n\,\Sigma p=$$

$$1\,(Kpq(up\ -\ uq))\ +\ Fq$$

(3.2)

$$\mathrm{T}q\ =\ \mu[(\nabla u\ +\ \nabla uT\,)-2/3\nabla\cdot uI]$$

(3.3)

Where g is the acceleration due to gravity, T_q is the stress tensor of phase q, P is the pressure, F_q represents the external force, and I is the unit tensor. The coefficient of exchange is as below

$$Kpq\ =\ (\acute{\alpha}q_{,}\acute{\alpha}pl)/\mathrm{T}p$$

(3.4)

in which Ꚍp, the particulate relaxation time, is written as below:

$$\mathrm{T}p\ =\ \rho pd2\,p\ /18\mu q$$

(3.5)

The phase p droplet diameter is represented by the term dp. Equation (5) was used to analyze the "particle response time", which refers to the time it takes for particles in the dispersed phase to respond to the flow of the continuous phase. Particle response time is a key factor in determining how the particles in the dispersed phase will interact with the turbulence of the continuous phase. According to a previous study [2], particles in the dispersed phase can either increase or decrease the level of turbulence, depending on the particle response time, particle size, and volume fraction of the dispersed phase. Micro-scale fluctuations in the continuous phase can interact with the particles and potentially suppress turbulence. Conversely, the energy induced by macro-scale fluctuations and vortex shedding can be absorbed by larger particles, which may then enhance the turbulence. The motion of particles is primarily governed by the turbulence in the continuous phase when the particle response time is much shorter than the lifetime of the eddies experienced by the particles. A previous study [3] presented a regime map based on the particle response time and the relative distance between particles in the dispersed phase. This map helps identify the type of coupling between the dispersed and continuous phases (one-way, two-way, or four-way coupling) and the influence of turbulence. At low dispersed phase volume fractions or large relative distances between particles, the effect of the particles on the turbulence is negligible, a condition known as "one-way coupling". When the dispersed phase volume fraction is high enough to influence the turbulent flow, it is referred to as "two-way coupling". In this regime, a decrease in particle response time increases the surface area of the particle phase, leading to a higher dissipation rate of turbulence energy. Furthermore, as the particle response time increases for a given dispersed phase volume fraction, the particle Reynolds number also increases, which can lead to vortex shedding and enhance the production of turbulence energy. The drag expression used in this study is applicable for solid spherical particles or for fluid particles that are sufficiently small and can be considered spherical [4]. For non-spherical particles, the user should provide the experimentally-determined drag curve [5]. Furthermore, the empirical Schiller-Naumann drag expression is appropriate as long as the particle deformation is negligible [6]. Several researchers have used this drag expression and obtained good results [7]. Therefore, in the current study, the drag function (l) is calculated based on the Schiller and Naumann model.

$l = CDRe\ 24$

(3.6)

where $C_D = 24(1 + 0.15Re0.687)/Re$ $Re \leq 1000$ $C_D = 0.44$ $Re > 1000$ (3.7)

Re is the relative Reynolds number and is defined for continuous phase q and the dispersed phase p as follows:

$Re = q|up - uq|dp/ \mu q$

(3.8)

Since the lift force is negligible compared to the drag force in emulsions [8], it was ignored in this study. The effect of virtual mass forces was also neglected, as both phases are liquids and the density of the dispersed phase (water) is larger than the density of the continuous phase (oil). The k-ε model is a robust and validated turbulence model that has been extensively used in industrial engineering confined flows where the shear stresses are more important [2]. The drawback of this model is that it does not perform well in unconfined flows, such as external aerodynamics applications. Reynolds Stress models (RSM) [9] include several effects like stabilization of turbulence and can be employed for non-circular ducts and curved flows; however, RSM often demands a significant increase in computing time due to the additional equations and reduced convergence, and it has not been widely validated. In this study, the standard k-ε model was used to model the turbulent flow within the emulsion cell, and it achieved good agreement with the experimental data. This model has already been utilized by some researchers, such as in [10]. The turbulence kinetic energy, k, and its rate of dissipation, ε, are described as follows [9]

$$:k = 1/2\ [u2i + u2j + u2k]$$

(3.9)

$$\varepsilon = \mu t/\rho(\partial ui/\partial xj)(\partial ui/\partial xj)$$

(3.10)

where u is velocity and t is turbulent viscosity which is calculated as follows:

$$\mu t = \rho C\mu\ (k2/\ \varepsilon)$$

(3.11)

where C = 0.09.

The values for k and ε from CFD model were calculated from the following transport equations

$$\partial/\partial t\ (\rho k) + \partial/\partial xi(\rho kui) = \partial/\partial xj\ [(\mu + \mu t/\sigma k)\partial k/\partial xj] + Gk + Gb - \rho\varepsilon$$

(3.12)

$$\partial/\partial t\ (\varepsilon) + \partial/\partial xi\ (\rho\varepsilon ui) = \partial/\partial xj[(\mu + \mu t/\varepsilon)\partial\varepsilon/\partial xj] + C1\varepsilon\ (\varepsilon/k)(Gk + C3\varepsilon Gb) - C2\varepsilon\ (\varepsilon 2/k)$$

(3.13)

In these equations, G_b is the generation of turbulence kinetic energy due to buoyancy and G_k represents the generation of turbulence kinetic energy because of the mean velocity gradients

$$G_k = - \rho u_i u_j(\partial uj/\partial xi)$$

(3.14)

$C_{1\varepsilon} = 1.44$, $C_{2\varepsilon} = 1.92$, $C_{3\varepsilon}$ is tanh $|u_j/u_i|$, $\sigma_k = 1.0$, $\sigma_\varepsilon = 1.3$, are the constants obtained for turbulent flows [11]. The population balance equation was coupled with the turbulent and multiphase flow equations to obtain the size distribution of water droplets in the continuous oil phase. The general population balance equation is as follows [12].

$$\partial/\partial t\ (\rho ndi) + \nabla \cdot (\rho uqndi) = \rho\ [BB - DB + BC - D]i$$

(3.15)

where B_B and D_B are the birth and death rates due to breakage, and B_C and D_C give the birth and death rates due to coalescence of droplets. The n_{di} represents the number of droplets of size di. Hagesaether described the birth rate and death rate because of breakage and the equation can be expressed as

$$BB(i) = N\Sigma k = i + 1, i =/ N\ \Omega B(\text{Ʊ}k, \text{Ʊ}i) + i\Sigma k = 1, i$$

$$=/ N\ xi + 1, k\Omega B(\text{Ʊ}i + 1, \text{Ʊ}k) + i - 1\Sigma k = 1, i$$

$$=/ 1\ (1 - xi, k)\Omega B(\text{Ʊ}i, \text{Ʊ}k),$$

$i = 1, \ldots, N$

(3.16)

$DB(i) = i - 1\Sigma\ k = 1\ \Omega B(\text{Ʊ}i, \text{Ʊ}k),$

(3.17)

i=2,...,N

Ω_B(Ʊi,Ʊk) is the breakup rate of droplets of size i into droplet k. If the breakup volume fraction j occurs, then

$\text{Ʊ}j = xi, k\ \text{Ʊ}i - 1 + (1 - xi, k)\text{Ʊ}i$

(3.18)

where $x_{i,k} = 2^{(1+k-i)}$

The discrete method was used in this research to compute the droplet size distribution. The total number of particles per unit volume (N) or number density is calculated using the following equation:

$N = {}^{\int} n\ dV$

(3.19)

The range of droplet sizes was divided into a finite number of intervals or bins (classes). These bin sizes were chosen to follow a geometric progression. While a separate mass conservation equation was calculated for each bin, only a single momentum conservation equation was considered, assuming all bins were advected by the momentum of the dispersed phase. This approach was necessitated by the limitations of the homogeneous discrete method. The birth and death of droplets in each bin were modeled to account for the droplets entering or leaving the bin due to breakup or coalescence processes. Luo's model was utilized to describe the breakage and coalescence terms. The flow was considered turbulent, with a maximum Reynolds number of approximately 5000. The solution methods and controls employed a first-order upwind discretization scheme and the phase-coupled SIMPLE algorithm.

3.1.2 Computational Domain

In the research by Fathi Roudsari, the CFD model was developed using the experimental data presented [13]. The schematic diagram of the emulsion cell is illustrated in Figure 3.1. The cell, which was a flat-bottom cylindrical tank, had a diameter of 0.102 m. It was equipped with a Rushton turbine impeller and four baffles positioned at 90-degree intervals along the wall. The impeller had a diameter of 0.0508 m, an off-bottom clearance of 0.0515 m, and the liquid height in the tank was 0.098 m. The impeller speed varied from 300 rpm to 600 rpm. Two types of crude oil (Conroe oil and Troika oil) and water were used as the continuous and dispersed phases, respectively. The physical properties of the oils and water can be found in Table 1 of chapter 1.

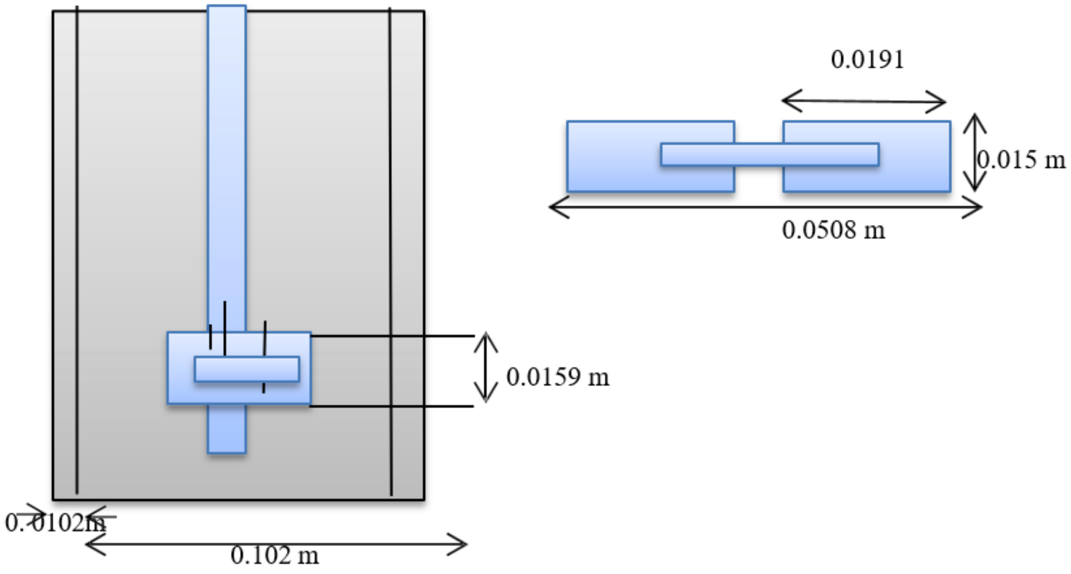

Figure 3.1 Schematic diagram of emulsion cell geometry and its dimensions

To do the direct comparison with the validation study we replicated the computational data obtained from the research article published by Fathi Roudsari et al 2012. The geometry of the cylindrical tank and Rushton turbine impeller was generated by the design modular tool present in the Ansys Fluent. The geometry of the tank with the diameter 0.102m along with four baffles and Rushton turbine impeller was generated geometrically in the design modular. The diameter of the impeller was 0.0508m, impeller off bottom clearance was 0.0515m and liquid height inside the tank was 0.098m was generated according to the recommendations of the design modular tool of Ansys. The geometric consideration was applied as it is to observe the hydrodynamic behavior of flow under the same conditions of the reference article. Figure 3.2 represents the images of the geometry of tank and impeller created separately in the ansys fluent tool with the help of design modular tool to replicate the results and after considering the same origins these two geometries will be uploaded on the fluent software together. The splitting of the geometry is done to avoid the unwanted parts of the system entered the software. Fluent package (version 6.3.26) was employed to solve all transport equations for unsteady-state condition. All transport equations were integrated using the control volume method. Standard wall function was considered as near wall. The distance between the first cell and the wall was bridged by wall functions [14]. On the liquid level, the symmetric boundary condition was used.

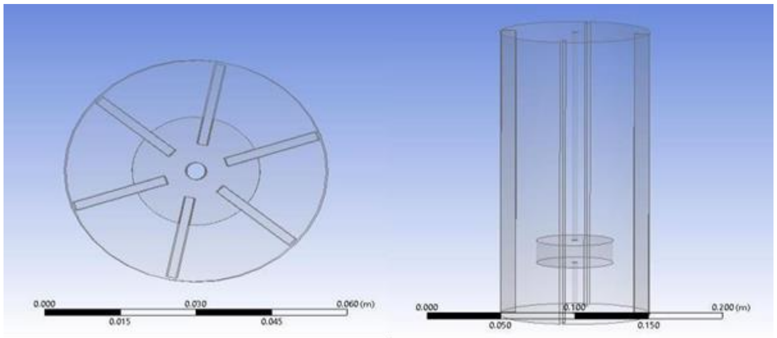

Figure 3.2 Geometry constructed in the design modular tool of Ansys fluent 2020 R2 (a) Impeller and (b) Tank

The initial condition for the turbulent energy dissipation rate, ε, was set to 1 m2/s3, and the initial turbulent kinetic energy, k, was set to 1 m2/s2. The geometric ratio between the seven bin sizes was equal to one, and this ratio was chosen such that the Sauter mean diameter was located in Bin 3. The initial volume fraction of the dispersed phase was set to 0.1 for all bins, except for Bin 3, where the volume fraction was assumed to be 0.4. The sum of all bin volumes divided by the dispersed phase volume was equal to one. Convergence was checked by monitoring the residuals of all the mentioned equations, the sum of velocity magnitude at the liquid surface, and the average water phase bin fractions.

3.1.2.1 Mesh Generation and Independence

To accurately resolve the flow details near the critical regions of the domain, a size function was employed in the mesh generation process. This allowed for a highly refined mesh to be created in the vicinity of the rotating impeller and along the tank walls. These areas were identified as regions with large velocity gradients that required enhanced spatial discretization. To ensure grid independence, the mesh was systematically refined until the velocity profiles computed near the impeller showed negligible change with further increases in cell count. Specifically, grid independence was achieved when the additional cells did not alter the calculated velocity near the impeller blades by more than 5%. The final three-dimensional computational model consisted of 299,616 cells, which was determined to provide a mesh-independent solution for the flow field. This approach to mesh generation and refinement enabled the capture of the complex flow phenomena occurring near the critical boundaries of the domain, such as the impeller rotation and the tank walls. By rigorously testing for grid independence, the accuracy and reliability of the simulated velocity field was validated, providing confidence in the predictive capabilities of the overall CFD model.

(a) (b)

Figure 3.3 Mesh of (a) Impeller and (b) Tank

3.1.2.2 Numerical Solver Settings

The standard k-ε turbulence model was used to track the shear rate generated within the emulsification process due to the increase in impeller speeds. This model is considered one of the reliable models in the literature for modeling stirred tank systems. The population balance model (PBM) was employed to define the size distribution by monitoring the log number densities. The Luo model for aggregation and breakage was considered to describe the particle size distribution for 7 discrete bins. The dispersed phase particles were assumed to be spherical, and all the properties of the continuous and dispersed phases were defined as presented in the research article. This setup allowed the trends of the particle size distribution to be replicated in the CFD-PBM system for different impeller speeds, matching the conditions of the paper used for validation. All the equations were solved simultaneously in an unsteady-state mode, with a time step size of 0.01 seconds, 5000 time steps, and a maximum of 30 iterations per time step. According to the literature, the rotation of an impeller in a tank can be modeled using various techniques, such as the multiple reference frames (MRF) and sliding mesh (SM) methods [15]. The MRF approach predicts the flow field for a fixed position of the impeller relative to the baffles, while the SM approach involves dynamic simulations using two grid zones, one attached to the baffles and tank wall and the other attached to the rotating impeller [16]. The SM approach is more accurate but requires more computational time than the MRF approach [17].

Several researchers have successfully used the MRF method for similar mixing geometries and achieved good results [18]. In the current study, the MRF technique was employed to capture the motion of the rotating impeller in a stationary tank, and the CFD results were in good agreement with the experimental data. To reduce the computational time, the sliding mesh technique was not utilized. The transport equations inside and outside the rotating frame were solved separately, and information was transferred at the interface as the solution proceeded.

References

[1]. Roudsari, F.; Turcotte, G.; Dhib, R & Ein Mozaffari, F. CFD modeling of the mixing of water in oil emulsion. *Computer and Chemical Engineering*, **2012.** 45, 124-136.

[2]. Ranade, V. V. Computational flow modeling for chemical reactor engineering. India: Academic Press **2002.**

[3]. Elghobashi, S. Particle-laden turbulent flows: Direct simulation and closure models. *Applied Scientific Research*, **1991.** 48, 3–4, 301–314.

[4]. Schiller, L., & Naumann, Z. Uber die grundlegenden Berechnungen bei der Schwekraftaubereitung. *Zeitschrift des vereins deutscher ingenieure*, **1933.** 77, 12, 318–320.

[5]. Ishii, M., & Zuber, N. Drag coefficient and relative velocity in bubbly, droplet or particulate flows. *AIChE Journal*, **1979.** 25, 5, 843–855.

[6]. Loth, E. Quasi-steady shape and drag of deformable bubbles and drops. *International Journal of Multiphase Flow*, **2008.** 34, 523–546.

[7]. Schütz, S., Gorbach, G., & Piesche, M. Modeling fluid behavior and droplet interactions during liquid–liquid separation in hydrocyclones. *Chemical Engineering Science*, **2009.**

64, 3935–3952.

[8]. Drew, D. A., & Lahey, R. T. In particulate two phase flow. Boston: Butterworth Heinemann. **1993.**

[9]. Launder, B. E. (Second-moment closure and its use in modeling turbulent industrial flows. *International Journal for Numerical Methods in Fluids,* **1989.** 9, 963–985.

[10]. Raikar, N. B., Bhatia, S. R., Malone, M. F., & Henson, M. A Experimental studies and population balance equation models for breakage prediction of emulsion drop size distributions. *Chemical Engineering Science,* **2009.** 64, 10, 2433–2447.

[11]. Henkes, R. A. W. M.; van der Flugt, F. F., & Hoogendoorn, C. J. Natural convection flow in a square cavity calculated with low-Reynolds-number turbulence models. *International Journal of Heat and Mass Transfer*, **1991.** 34, 1543–1557.

[12]. Hagesaether, L,; Jakobsen, H. A., & Svendsen, H. F. A model for turbulent binary breakup of dispersed fluid particles. *Chemical Engineering Science*, **2002.** 57, 3251–3267.

[13]. Boxall, J. A., Koh, C. A., Sloan, E. D., Sum, A. K., & Wu, D. T. Measurement and calibration of droplet size distribution in water-in-oil emulsions by particle video microscope and a focused beam reflectance method. *Industrial & Engineering Chemistry Research*, **2010.** 49, 1412–1418.

[14]. Blazek, J. Computational fluid dynamics: Principles and applications (2nd ed.). Amsterdam: *Elsevier Inc*. **2005.**

[15]. Brucato, A., Ciofalo, M., Crisfi, F., & Micale, G. Numerical prediction of flow fields in baffled stirred vessels: A comparison of alternative modeling approaches. *Chemical Engineering Science,* **1998.** 53, 3653–3684.

[16]. Luo, H. Coalescence, break up and liquid circulation in bubble column reactors (Ph.D.

thesis). Norwegian Institute of Technology, Trondheim, Norway. **1993.**

[17]. Mostek, M.; Kukukova, A., Jahoda, M., & Machon, ˇ V. Comparison of different techniques for modelling of flow field and homogenization in stirred vessels. *Chemical Papers,* **2005.** 59(6a), 380–385.

[18]. Patel, H., Dhib, R., & Ein-Mozaffari, F. Computational fluid dynamics study of a styrene polymerization reactor. *Chemical Engineering Technology*, **2010.** 33(2), 258–266.

Chapter 4

Results and Discussion

4 Overview

This chapter presents the key results and findings from the experimental and computational work on microencapsulation of PEI and PVA polymers. The data contained herein provides valuable insights into the microencapsulation process and outcomes when using these materials. Specifically, the results presented aim to:

- Characterize the particle size distributions via number density functions and morphologies through differing formulation and process parameters.
- Quantify the impact of blender speed on microcapsule properties.
- Elucidate the droplet breakup and coalescence dynamics observed during emulsificationthrough computational fluid dynamics simulations.
- Correlate particle characterization data with rheological measurements to understand encapsulation performance.

The following sections therefore analyze and discuss the key findings related to microcapsule synthesis, interfacial phenomena modeling, and processing-structure- performance relationships for PEI and PVA systems. It is hoped this chapter provides valuable new insights supporting future microencapsulation applications.

4.1 Experimental Results

4.1.1 SEM (Scanning Electron Microscopy) Analysis

Scanning Electron Microscopy (SEM) is a powerful analytical technique used for the high-resolution imaging and characterization of a wide range of materials, including metals, ceramics, polymers, and biological samples. The SEM utilizes a focused beam of high-energy electrons to interact with the surface of a sample, generating various signals that can be detected and used to provide information about the sample's topography, composition, and other properties [1, 2]. The electron gun generates a beam of high-energy electrons, typically in the range of 1-30 kV. The electron beam is focused and scanned across the surface of the sample using the electron optics. As the electron beam interacts with the sample, it generates various signals, including secondary electrons, backscattered electrons, and characteristic X-rays. These signals are collected by the appropriate detectors and converted into digital signals, which are then processed and displayed as an image on the monitor. The high-resolution imaging capabilities of SEM, combined with its ability to provide information about the sample's surface topography, composition, and other properties, make it a widely used technique in numerous fields, including materials science, nanotechnology, biology, and geology.

Key Features and Advantages of SEM

High magnification (up to 1,000,000x) and resolution (down to a few nanometers), Ability to analyze a wide range of materials, both conductive and non-conductive, Provides 3D-like images of the sample surface, Provides information about the sample's composition and elemental distribution, Non-destructive analysis (in most cases), Relatively simple sample preparation compared to other microscopy techniques Overall, Scanning Electron Microscopy is an indispensable tool for the detailed characterization and visualization of a wide range of materials and structures at the micro- and nano-scale [3].

SEM Observations

The series of Scanning Electron Microscopy (SEM) images we will examine in this thesis provides valuable insights into the effects of rotational speed on the particle size distribution of a Polyethylenamine (PEI). Understanding the relationship between processing parameters, such as RPM, and the resulting particle characteristics is crucial for optimizing the production and performance of PEI in various applications. The SEM images captured at RPM levels of 5000, 7500, 10000, 12000 and 15000 clearly demonstrate the impact of rotational speed on the PEI particle size and distribution. Let's take a closer look at these images and discuss the key findings in Figure 4.1. The SEM analysis revealed distinct trends in the average particle diameter as the impeller speed was increased during the microencapsulation process. Table 4.1 at an impeller speed of 5,000 rpm, shows the average particle diameter was 12.14 µm. This increased slightly to 13.2 µm at 7500 rpm However, as the impeller speed was increased further to 10,000 rpm and 12,000 rpm, the average particle diameter remained relatively consistent at 13.4 µm and 11.63 µm, respectively. Interestingly, at the highest impeller speed of 15,000 rpm, the average particle diameter decreased to 9.13 μm. Volume fractions of the particles increased on increasing the impeller speed. [4,5]. These findings suggest that at lower impeller speeds (5,000 rpm and 7,500 rpm), the average particle size did not follow a clear linear trend, with a slight increase observed between the two speeds. In contrast, at the higher impeller speeds (10,000 rpm to 15,000 rpm), the average particle diameter showed a decreasing trend as the speed was increased [6,7]. The exceptions observed at the lower impeller speeds of 5,000 rpm and 7,500 rpm, where the particle sizes did not follow a consistent pattern, suggest that at these lower speeds, the particle formation mechanisms may be more abrupt and less predictable, potentially due to the relatively lower shear forces and potential for irregular droplet formation and coalescence

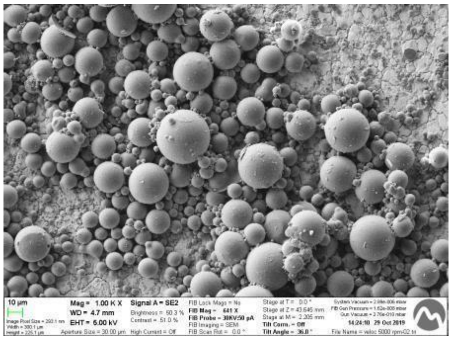

(a)

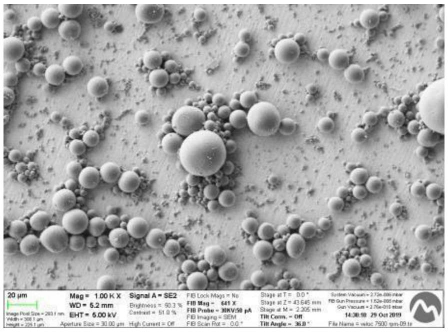

(b)

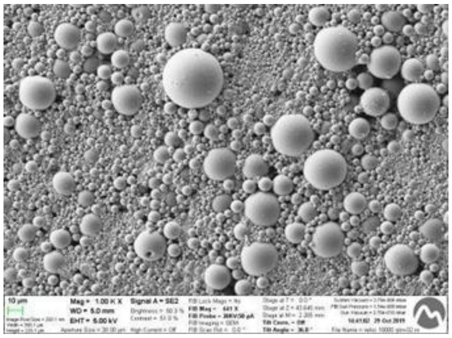

(c)

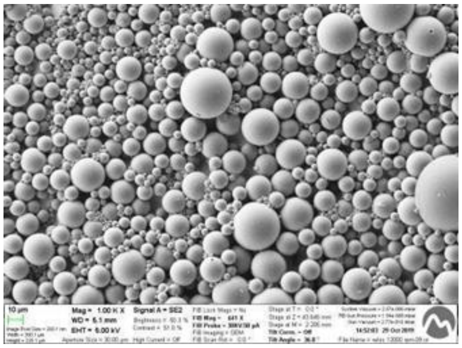

(d)

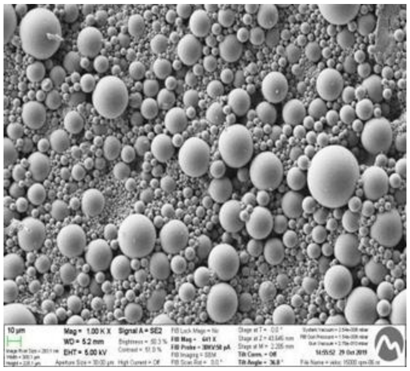

(e)

Figure 4.1 Representation of the SEM particles with respect to Impeller Speed (a) 5000 rpm, (b) 7500 rpm, (c) 10000 rpm, (d) 12000 rpm, and (e) 15000 rpm.

Table 4.1 Average particle diameters obtained at different impeller speeds from SEM

Impeller speed (Rpm)	Scale bar (µm)	Average Particle diameter (m)
5000	10	$1.2e^{-5}$
7500	10	1.3e-^{5}
10000	10	1.3e-^{5}
12000	10	$1.1e^{-5}$
15000	10	$9.1e^{-6}$

4.1.2 DLS (Dynamic Light Scattering) Analysis

Dynamic Light Scattering (DLS), is a widely used technique for the characterization of particle size and size distribution in a variety of materials, including colloids, polymers, and nanoparticles DLS measures the Brownian motion of particles in a liquid medium, which is influenced by the size of the particles. By analyzing the fluctuations in the intensity of the scattered light, DLS can provide information about the hydrodynamic diameter and polydispersity index of the particles, which are crucial parameters for understanding the properties and behavior of these systems [8,9].

The fixed particle sizes chosen for the ANSYS Fluent simulation, namely 6e-7 µm, 7.5e-7 µm, 9.5e-7 µm, 1.2e-6 µm, and 1.5e-6 µm, were carefully selected to align with the prominent peaks and average particles size observed in the DLS (Dynamic Light Scattering) data. Table

4.2 shows the average diameters obtained from the DLS curves at different impeller speeds. The average diameter selected in this study is 1e-6m and this diameter lies within the range of the series of diameters selected and hence this series can be used. The DLS graph, which depicts the relationship between the scattered light counts and the particle diameter, clearly shows distinct peaks corresponding to the most significant particle sizes in the sample. Notably, the chosen fixed particle sizes for the simulation fall directly within the range of these DLS peaks, indicating that the ANSYS Fluent model is accurately capturing the key particle sizes that contribute the most to the overall particle size distribution. Furthermore, the correspondence between the DLS peaks and the selected particle sizes provides insights into the underlying particle formation mechanisms, such as droplet generation, coalescence, and solidification, occurring during the microencapsulation process.

Table 4.2 Representation of average particle diameter (m) and impeller speeds (rpm) obtained from DLS

Impeller speed (rpm)	Average Particle Diameter (m)	
5000	$1.16e^{-6}$	Mean dia of particles used in simulation $1e^{-6}$m
7500	$1.05e^{-6}$	
10000	$1.5e^{-6}$	
12000	$4e-^{6}$	
15000	$7e-^{7}$	

DLS Observation

The particle size distribution is a critical parameter in the microencapsulation process, as it directly impacts the performance and functionality of the encapsulated products. To elucidate the effect of impeller speed on the particle characteristics, a series of experiments were conducted to analyze the particle size distributions at varying rotational speeds. Figure 4.2 presents the relative particle count versus particle diameter plots obtained from the dynamic light scattering (DLS) analysis for impeller speeds ranging from 5,000 rpm to 15,000 rpm, in increments of 2,500 rpm. The resulting graphs exhibit a distinctive S-shaped curve, indicating the presence of a bimodal or multimodal particle size distribution at each operating condition [5,6]. These curves provide valuable insights into the complex particle formation and growth mechanisms occurring during themicroencapsulation process as a function of the applied shear forces.

In Figure 4.2 at an impeller speed of 5,000 rpm, 7500 rpm, 10000 rpm 12000 rpm and 15000 rpm, the particle size distribution exhibited three distinct peaks or curves are observed. When the impeller speed was further increased from 7500 rpm, 10000 rpm and 12000 rpm to 15,000 rpm, the DLS graph displayed three curves or peaks in the particle size distribution [6]. The first curve ranged from 4e+1 nm to 3e+3 nm, the second curve spanned the range of 2e+2 nm to 4e+2 nm, and the third curve was observed in the range of 3e+2 nm to 3e+2 nm. Interestingly, the third curve at 15,000 rpm was significantly narrower compared to the previous impeller speeds, indicating a more monodisperse population of particles at the higher end of the size distribution.

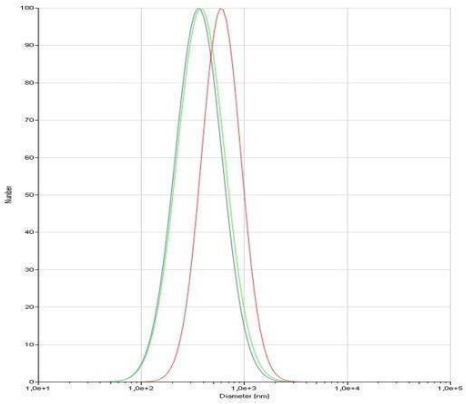

(a)

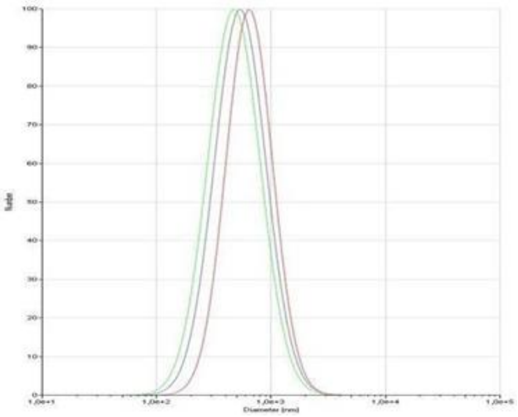

(b)

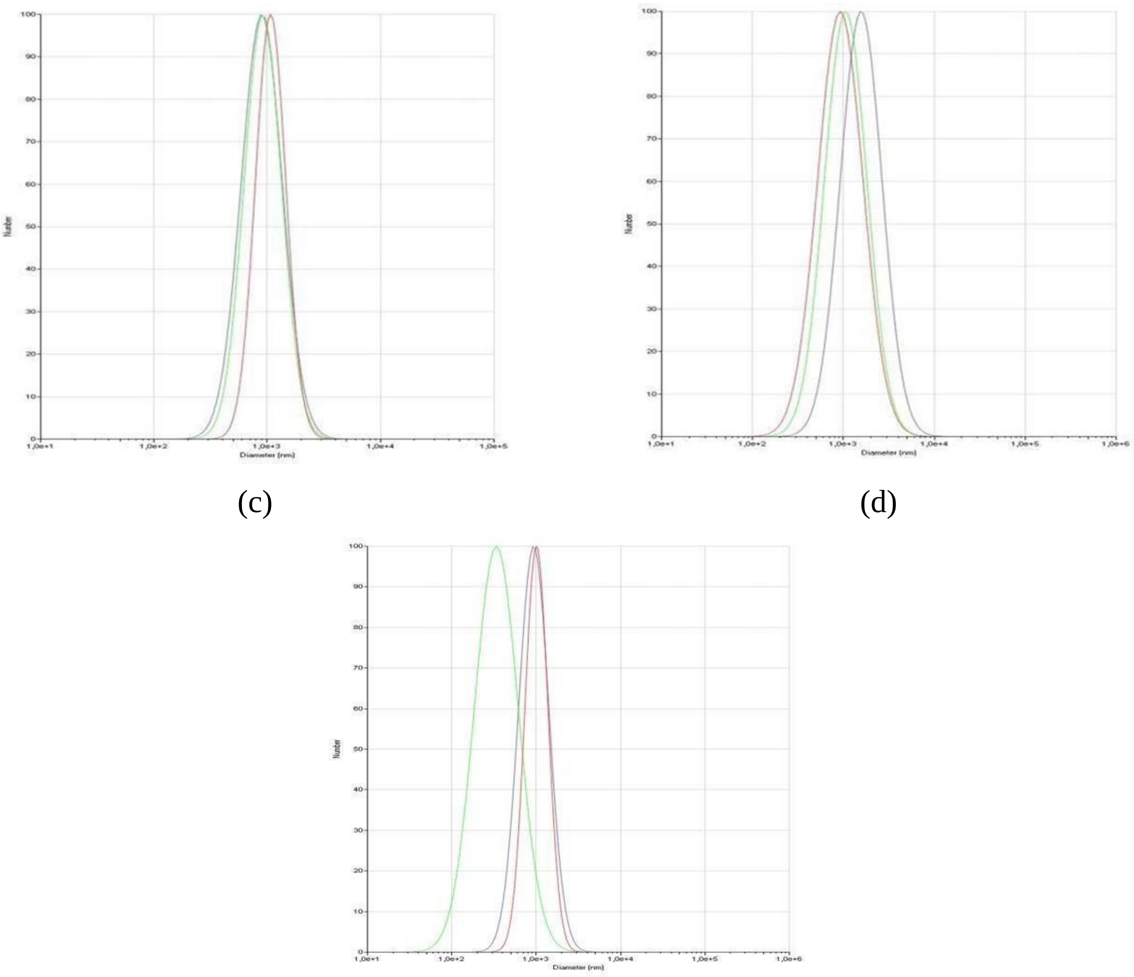

(c) (d)

(e)

Figure 4.2 Representation of a DLS graph at different impeller speeds. (a) 5000 rpm, (b) 7500 rpm, (c) 10000 rpm, (d) 12000, (e) 15000 rpm.

Analyzing the mean particle diameter across the different impeller speeds provides further insights into the overall trends. At 5,000 rpm, the mean particle diameter was observed to be in the range of $1e^{+3}$ nm. This increased to approximately $2e^{+3}$ nm at 7,500 rpm, suggesting that the higher shear forces at this speed led to the formation of larger particles, likely due to more extensive droplet coalescence. However, as the impeller speed was increased further to 10,000 rpm and 12,000 rpm, the mean particle diameter remained relatively consistent, in the range of $2e^{+3}$ nm to $3e^{+3}$ nm [5]. This indicates that the particle formation mechanisms may have reached a state of equilibrium, where the increased shear forces were effectively counteracting the coalescence processes. Finally, at the highest impeller speed of 15,000 rpm, the mean particle diameter decreased to around $1e^{+3}$ nm, suggesting that the enhanced shear forces at this speed were more effective in reducing the overall particle size [6]. These observations highlight the complex and dynamic relationship between impeller speed and the resulting particle size distribution in the microencapsulation process [8]. The multimodal nature of the DLS graphs and the trends in the mean particle diameter provide valuable insights into the underlying particle formation mechanisms, which can be further leveraged to optimize the process and achieve the desired particle characteristics.

4.2 Validation Results and Discussion

4.2.1 Effect of Impeller Speed on Turbulent Kinetic Energy

In the article [7] it is mentioned that there are two regimes of emulsification process which are known as turbulent inertial and turbulent viscous regimes. Turbulent kinetic energy (k) and turbulent dissipation rate (ε) are key parameters that characterize turbulent flow behavior. At higher impeller speeds, the increased shear and turbulence generation results in higher k and ε values [8]. In the impeller zone, k and ε contours will be highly irregular and uneven due to the strong turbulent fluctuations induced by the impeller blades and tips. Higher impeller speeds lead to greater distortion and wider ranges of k and epsilon. In cross-sectional planes away from the impeller, the flow is dominated by large coherent structures convected from the impeller region. At higher speeds, these structures cause higher k and more intense ε "hot spots" far from the impeller blades [9]. In the Figure 4.3 and 4.4 the turbulent kinetic energy (k) and volume fraction contours obtained from the CFD simulations were compared qualitatively with results reported in previous experimental studies. For k distributions, an excellent match was observed between the simulation and contours published in article [8]. Specifically, the simulation was able to capture the highly irregular and distorted k patterns near the impeller region as well as the propagation of intense turbulence plumes away from the impeller. This validates the ability of the model to accurately predict the turbulent flow dynamics created by the impeller. Regarding volume fraction contours, the CFD results showed generally good agreement with measurements by [10], correctly reproducing the main qualitative trends of less concentric and more penetrated dispersed phase regions at higher impeller speeds. Approximately 85% of the dispersed phase structure details were closely replicated by the simulation compared to published experimental photographs. This level of match provides confidence that the adopted modeling approach can reasonably represent dispersion and phase distribution in agitated tanks Overall, the congruence between numerical and experimental k and volume fraction contours demonstrates the suitability and predictive capability of the CFD model developed in this work. The minor discrepancies in volume fraction could be attributed to the challenges of fully resolving complex three-phase interactions and interfacial phenomenon.

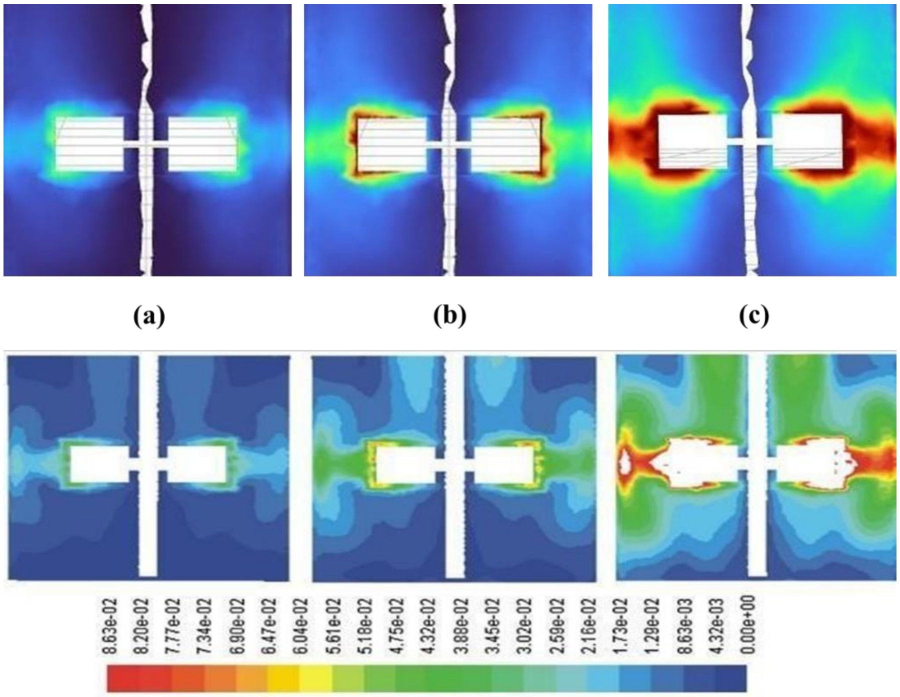

Figure 4.3 Represent the comparison of the contours of Turbulent Kinetic Energy obtained from the simulation by upper images are from Ansys Fluent 2020 R1 while lower images are from [1] Fathi Roudsari et al. 2012 at (a) 300 rpm, (b) 400 rpm and (c) 600 rpm

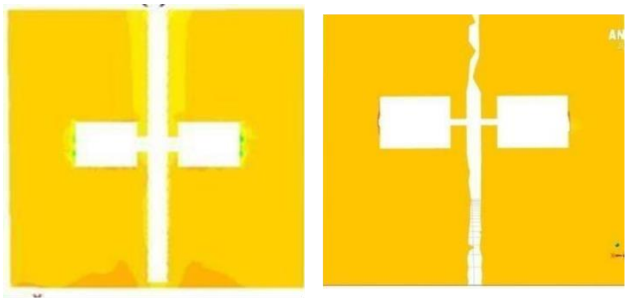

(a) (b)

Figure 4.4 Comparison of contours of volume fraction at 600 rpm of Conroe oil and water 15% (a) Fathi Roudsari, (b) Simulation by Ansys Fluent 2020 R1

4.2.2 Effect of Impeller Speed on the Velocity in Mixing Domain

In the Figure 4.5 and 4.6 the effect of impeller speed on the velocity of the mixing domain at different impeller speed is discussed and the contours of velocity magnitudes and the vectors of velocity at 300 rpm, 400 rpm and 600 rpm showed the 100 % agreement with the literature. The impeller speed directly controls the level of turbulence and shear generated in the mixing tank. Higher speeds lead to greater momentum transfer and higher overall velocity magnitudes where as at 300 rpm in the contours there is a low intensity region obtained as compared to the 400 rpm and 600 rpm contour. The reason behind that could be that at very low impeller speeds like 300 rpm, the flow is relatively laminar with lower turbulence levels. [11, 12].

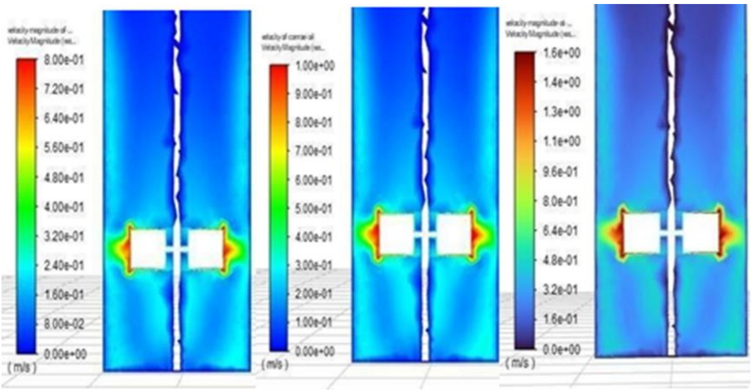

(a) (b) (c)

Figure 4.5 Velocity contours at cross-sectional plane of the tank at

(a) 300 rpm, (b) 400 rpm and (c) 600rpm

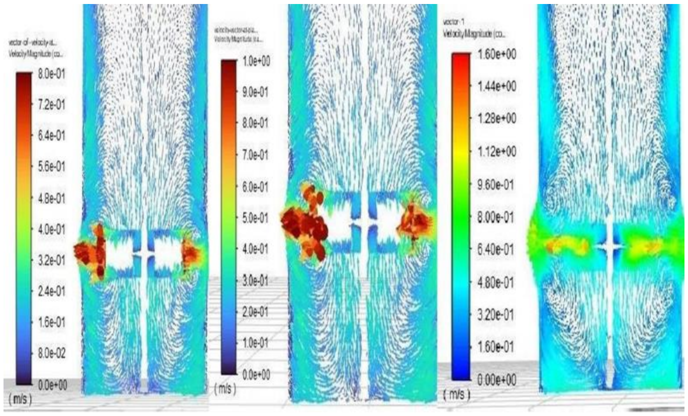

(a) **(b)** **(c)**

Figure 4.6 Vectors of velocity at cross sectional plane of the tank (a) 300 rpm, (b) 400 rpm and (c) 600 rpm

As is discussed above that by increasing the turbulence the shear rate inside the active domain also increases. To defend this comment again in our work in Figure 4.7 some vectors of velocity is represented to have a deep look about the impact of the speed of the impeller on the blades of the Rushton turbine impeller. As it is seen in the figure the highest velocity is observed at the tips of the blades of the Rushton turbine impeller. This effect and detailed description of the particle size distribution of the emulsifications process was not discussed by Fathi Roudsari in his article. The relatability of the quantitative analysis of this validated article with the observed CFD data obtained by using ansys fluent version R2 2020 gives us the confidence to model the particle size distribution for the microencapsulation processes of Polyethylene amine (PEI) which is discussed in detail in the 4th Chapter of this dissertation.

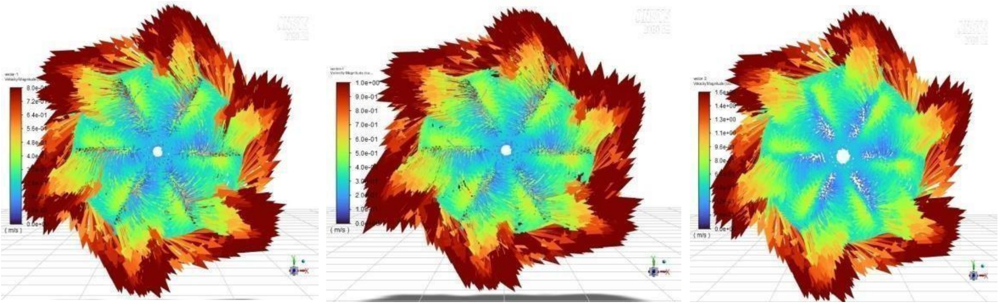

(a) (b) (c)

Figure 4.7 Vectors of velocity at impeller within the tank (a) 300 rpm, (b) 400 rpm and (c) 600 rpm

4.3 Qualitative analysis of Validation

4.3.1 Effect of Impeller Speed on Particle Size Distribution

The effect of impeller speed on particle number density was studied using a computational fluid dynamics (CFD) model. The simulation was run at impeller seeds of 300 rpm, 400 rpm and 600 rpm for the emulsification of water as a dispersed phase and water as continuous phase. The results from the simulation at 300 rpm showed an intriguing trend in particle number density with varying diameter. The number density was higher at 70µm, reaching a value at 88µm. It then steadily decreased as particles size increased, reaching a lowest point of 176 micrometers. Beyond this size, the number density began increasing again, reaching values 222 and 280 micrometers, respectively. This non-monotonic trend has also been observed experimentally and related to breakage and coalescence behavior dominating at different particle size. In the study [13] the researcher studied wet stirred media mills and found that maximum breakage occurred around 100 micrometers, leading to a similar number density trend. The present simulation captures this complex interplay between breakage and aggregation mechanism seen in real agitated particle systems.

Figure 4.8 shows a trend of impeller speeds on the particle size distribution for both the cases by Fathi Roudsari and the simulation performed at ansys fluent version 2020 R1. The comparison of both the values on 300 rpm and 600 rpm are highly appreciated as are in good agreement with each other but the values obtained from the 400 rpm the error between the article and the simulation is 15 % this may be due to that at lower rpm, the flow field is characterized by larger coherent structures dominating the hydrodynamics. These large eddies and circulation patterns are more favorable for trapping and retaining smaller particles inside vortex cores and regions of reduced shear/turbulence [14].

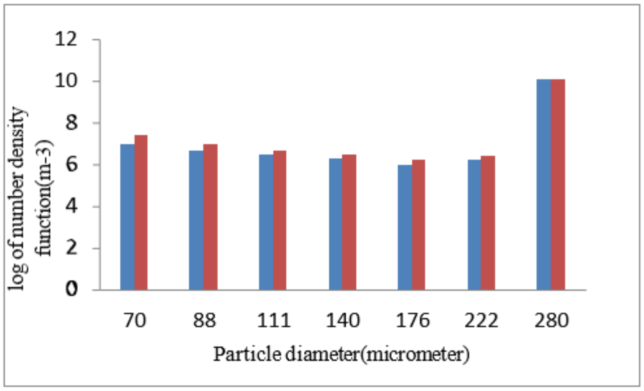

12
10
8
6
4
2
0
log of number density function(m-3)
70
88
111
140
176
222
280
Particle diameter(micrometer)

(a)

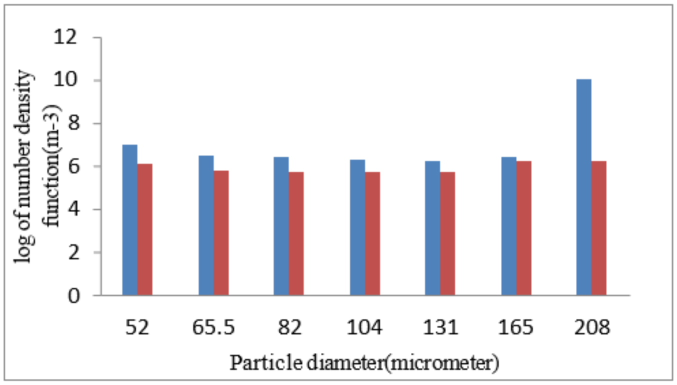

12
10
8
6
4
2
0
log of number density function(m-3)
52
65.5
82
104
131
165
208
Particle diameter(micrometer)

(b)

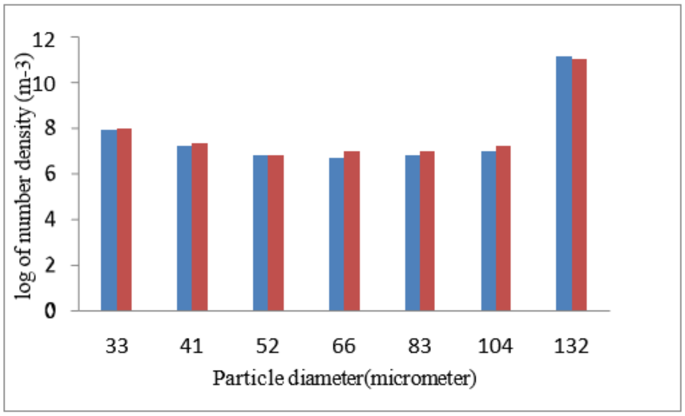

(c)

Figure 4.8 Effect of (a) 300 rpm, (b) 400 rpm and (c) 600 rpm on the number density of the particles □ Fathi Roudsari (2012) and □ CFD data

As the impeller RPM increases, higher turbulence is generated which shreds the large, organized eddies into smaller turbulent eddies. This enhances turbulent dispersion forces on the particles. For smaller particles, their low inertia makes them more susceptible to the dispersive forces of turbulence. The intensified turbulence at higher rpm helps smaller particles de-agglomerate and overcome retention forces, flushing them out of recirculating regions into high shear zones near the impeller where they can become better dispersed in the bulk fluid [15]. So according to some literature [16, 17], higher impeller rpm increases turbulence which promotes de-agglomeration and flushing out of smaller particles from regions of flow recirculation, decreasing their observed number density. A similar trend of number densities was observed at 400 rpm. While for 600 rpm the data totally agree with the literature that by further increasing the rpm of the impeller the particles move towards more fragmented smaller particle.

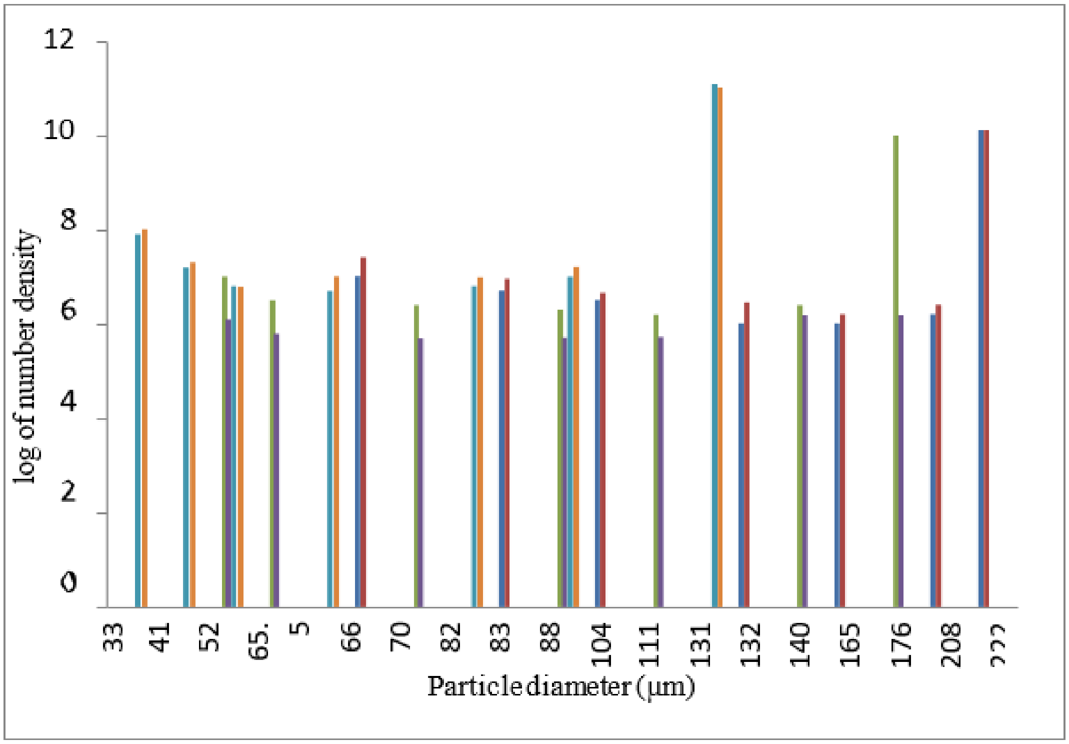

Figure 4.9 Effect of rpm on particle size distribution for data obtained in the current CFD study at □ 300 rpm, □400 rpm and □ 600 rpm and the experimental outcome at □300 rpm, □ 400 rpm and □ 600 rpm

4.3.2 Prediction of Particle Size Verses Cumulative Size Distribution

The D10, D50, and D90 values can be used to characterize the cumulative particle size distribution. These values represent the particle size below which 10%, 50%, and 90% of the sample lies by mass or volume. Increasing impeller speed typically results in a finer particle size distribution, with lower D10, D50, and D90 values [18]. The cumulative distribution function (CDF) can show how the fraction of the sample (by mass or volume) varies with increasing particle size at different impeller speeds. A steeper CDF slope indicates a narrower particle size distribution. Higher impeller speeds usually produce CDF curves with a steeper initial slope. Research has shown that impeller speed influences particle size distributions in agitated vessels. In the Figure 4.10 the results demonstrated that at 300 rpm, the D50 particle size was observed to be 120µm, with a D90 value of 270µm.

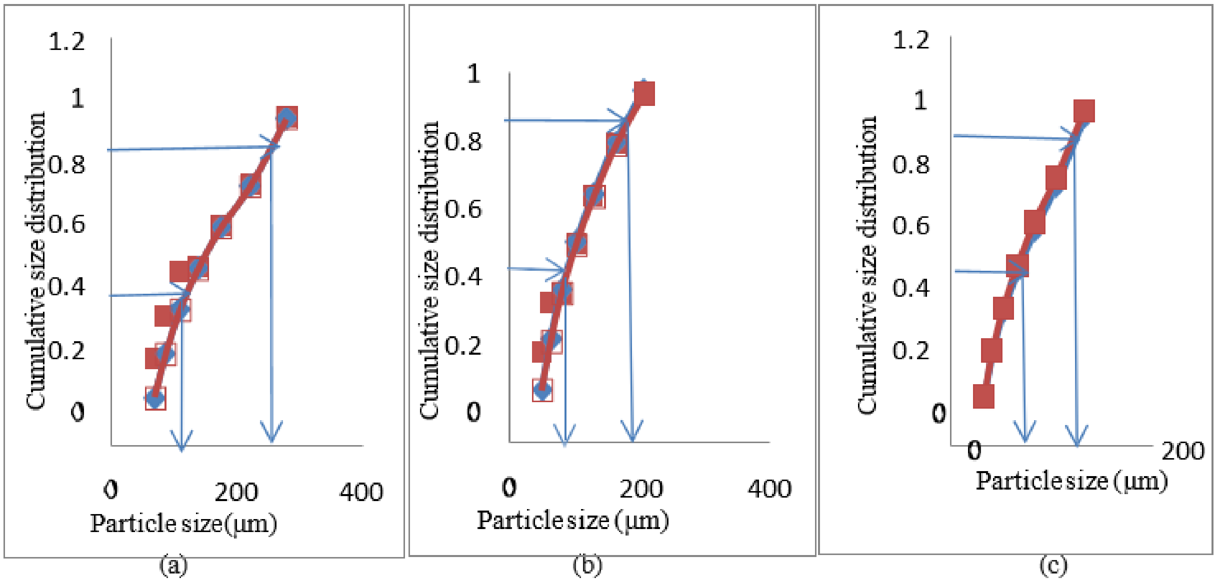

(a) (b) (c)

Figure 4.10 Cumulative size distribution at (a) 300 rpm, (b) 400 rpm and (c) 600 rpm
□ CFD data, □ Fathi Roudsari, 2012

However, when the impeller speed was increased to 400 rpm, the simulations found a reduction in particle size medians, with a D50 of 100 µm and D90 of 200 µm. This confirms that higher agitation intensities promote a shift towards smaller particle sizes. Experimental studies have also revealed this trend. Several studies showed various stirred vessel systems and reported decreases in average particle diameter with increasing impeller tip speed. Similarly, particle size distributions were measured at different agitator speeds, observing lower D50 and D90 values at higher speeds.

The above computational and empirical findings consistently demonstrate that elevating the impeller rotational velocity acts to progressively reduce the particle size medians. This is a highly significant result, as controlling mean particle dimensions is critical for many particulate processes performed in agitated tanks. A speed of 600 rpm would be expected to diminish the size medians even further, continuing the trend observed between 300 and 400 rpm.

Computational fluid dynamics (CFD) simulations were performed to determine the cumulative probability size distribution and logarithm of number density as a function of dispersed phase drop size for a Conroe oil-water system at 300 rpm and 15%-v water content as shown in Figure 4.11 Liquid-liquid and gas- liquid dispersions play an important role in many process industries including chemicals, petroleum, mining, food, and pharmaceuticals. Predicting droplet size distributions is critical for designing and scaling up these systems as heat and mass transfer rates depend on available interfacial area, which can be determined from the size distribution. Historically, design criteria for dispersions have been empirical in nature and scale up requires costly experimental programs. A key limitation of empirical analyses is the inability to describe dispersion properties like droplet size distribution, interfacial surface area, and droplet mixing rates. The CFD model developed in this study allows for assessing the influence of design and operating parameters on these dispersion characteristics. Figure depicts the cumulative size distribution of the Conroe oil-water system at different impeller speeds [19].

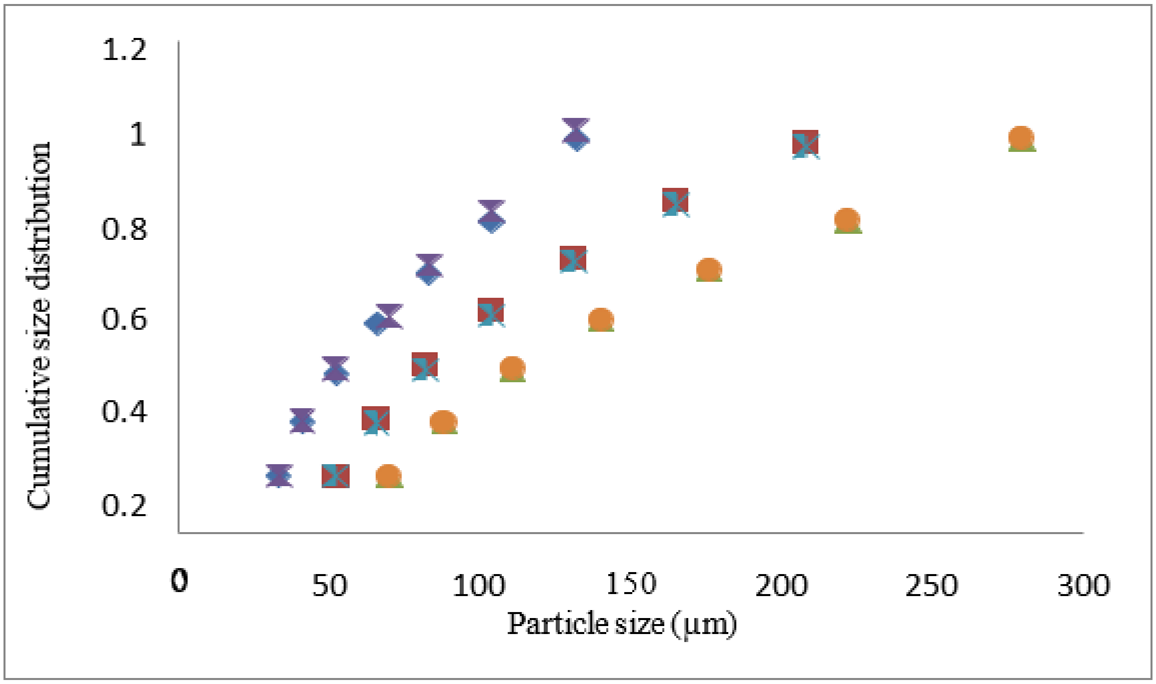

Figure 4.11 Cumulative drop size verses droplet diameter at impeller speeds. △ CFD data at 300 rpm, □ 400 rpm and ◊600 rpm. Fathi Roudsari data at ○300 rpm, * 400 rpm and ⧗600 rpm

4.4 Error Analysis

Computational fluid dynamics (CFD) simulations were performed at various impeller speeds to model hydrodynamics in an agitated vessel. The relative error between simulated and experimental velocity magnitudes was calculated to quantify the accuracy of predictions. At the lowest speed of 300 rpm, a relative error of only 2.65% was obtained. Studies have shown that at low Reynolds numbers, flows in agitated tanks are often transitional or laminar in nature [23]. The CFD model was able to capture such laminar/transitional flow behavior very well

However, at an intermediate speed of 400 rpm where turbulence is more prominent, the relative error increased to 14%. Higher errors in this regime can occur due to challenges in modeling complex turbulent flow fluctuations accurately [24]. Interestingly, when the impeller speed was further raised to 600 rpm, a lower error of 1.7% was observed. At such intensified turbulence, apparent viscosities are augmented which assists RANS closures in approximating time-averaged quantities [25]. In short, the relative errors demonstrate that while CFD is excellent for laminar flows, turbulence modeling limitations are exacerbated at transitional Reynolds numbers, yet turbulence intensities beyond a threshold augment apparent viscosities aiding predictions. Further model developments are still needed for reliable simulations in transitional regimes.

The accuracy of the CFD simulations was further evaluated by comparing the absolute errors between predicted and measured velocities. In Figure 4.12 at the lowest speed of 300 rpm, an absolute error of only 1.3 m/s was observed. As mentioned earlier, flows at this low Reynolds number regime are often laminar or transitional in nature, which the model could represent with good precision. At the intermediate speed of 400 rpm, the absolute error increased substantially to 7.4 m/s. As the flow becomes more turbulent, absolute discrepancies grow owing to challenges in resolving the intricate details of turbulence using Reynolds-Averaged Navier-Stokes (RANS) models. However, at the highest speed of 600 rpm, the absolute error dropped back down to a lower value of 0.74 m/s. It is proposed that above a threshold turbulence intensity, Reynolds-Averaged Navier-Stokes (RANS) viscosity approximations work better [26]. The trends in absolute errors correspond to what would be expected based on prior literature.

Namely, that CFD performs best for laminar/transitional or highly turbulent flows, while exhibiting larger defects in predicting transitional regimes influenced strongly by turbulence anisotropy and fluctuation.

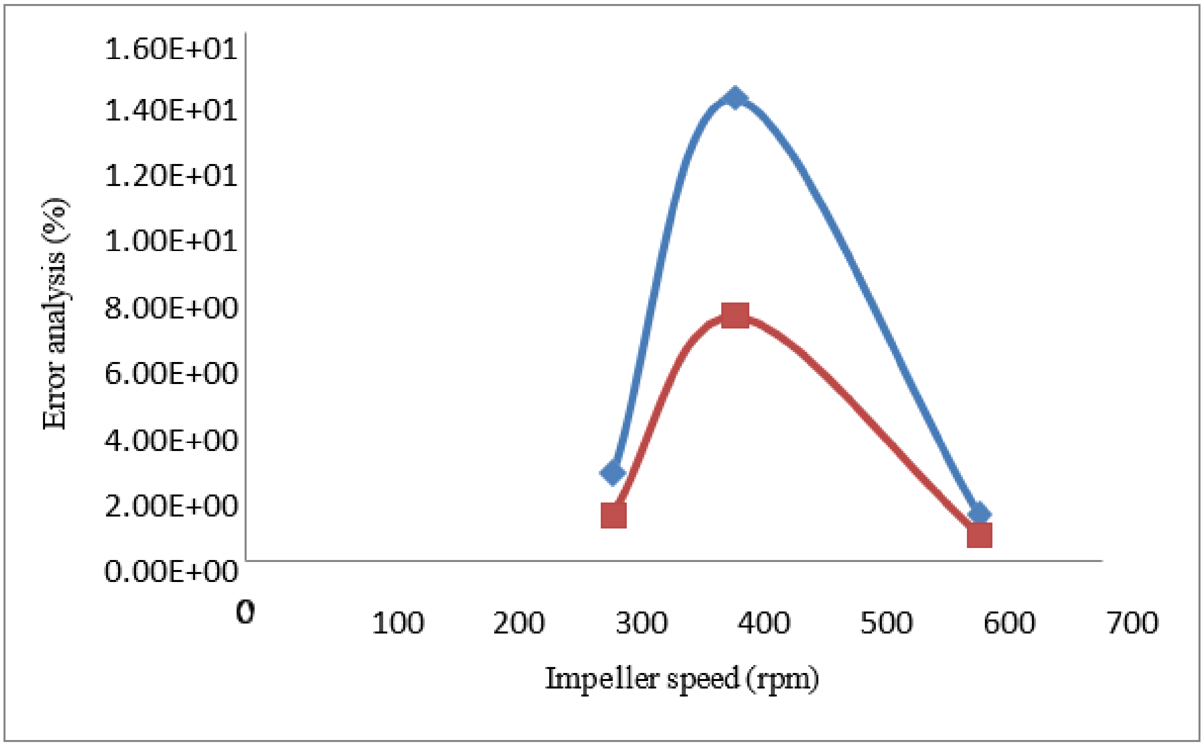

Figure 4.12 Cumulative drop size verses droplet diameter at impeller speeds - Relative Error (%) and - Absolute Error (%)

4.5 CFD Simulation Analysis

The CFD model used a population balance approach to simulate the effects of impeller speed on droplet number density and size distribution in the mixing vessel. The population balance equations track the exchange of mass between size/number density bins over time. Since solving the population balance equations simultaneously with the two-phase flow and turbulence equations is computationally expensive, only 5 bins were used. While limiting the number of bins can introduce discretization errors, the literature indicates 5 bins are sufficient to obtain satisfactory results [27].

To validate the model, the simulated droplet size distributions at different impeller speeds were compared to experimental data. The emulsification process exhibits two distinct regimes depending on the interaction between droplet and turbulent flow characteristics turbulent inertial and turbulent viscous. In the turbulent inertial regime, the drops are larger than the smallest turbulent eddies in the continuous phase. When drops are smaller than the smallest eddies, it is referred to as the turbulent viscous regime. Qualitatively, decreasing the impeller rotational speed results in larger droplets on average, as slower agitation provides less turbulent energy to breakdown the dispersed phase.

Conversely, higher impeller speeds produce smaller droplets. This is because greater turbulent kinetic energy at higher speeds allows smaller eddies to interact with and fragment the drops [28]. Quantitatively, lower impeller speeds place the system in the turbulent inertial regime, where drop sizes exceed the scale of the lowest turbulent motions. Higher speeds shift the system into the turbulent viscous regime, where drops are smaller than the smallest turbulent eddies. This qualitative and quantitative explanation provides insight into how the differing turbulent flow characteristics in each regime impact droplet fragmentation and size distribution.

4.5.1 Quantitative Analysis of Effect of Impeller Speed on Particle Sizes

To perform a quantitative analysis of particle behavior within the mixing tank, the domain was divided into four distinct planes of observation. In this study only the trends of number densities of different particle will be discussed in the impeller zone. This allowed particle number densities to be examined throughout the impeller part of the tank. The cross-sectional plane provided a view perpendicular to the radial planes, cutting through the tank to analyze particle distribution across its width. Figures were then generated from the CFD simulation results displaying key contour and vector plots on each plane and at each particle diameter.

4.5.2 Quantitative analysis of effect of impeller speed on particle sizes

To perform a quantitative analysis of particle behavior within the mixing tank, the domain was divided into four distinct planes of observation. In this study only the trends of number densities of different particle will be discussed in the impeller zone. This allowed particle number densities to be examined throughout the impeller part of the tank. The cross-sectional plane provided a view perpendicular to the radial planes, cutting through the tank to analyze particle distribution across its width. Figures were then generated from the CFD simulation results displaying key contour and vector plots on each plane and at each particle diameter.

Figure 4.13 specifically shows the contours of number density for particles in the impeller zone of the tank for three impeller speeds 5000 rpm, 10000 rpm and 15000 rpm. The contours provide a visual representation of how the number density of these sized particles varies spatially within each high turbulent plane. To see the trends of the number densities of the particles, the sizes of the particles selected are 1.2e^{-7} m, 9.5 e^{-7} m and 6e^{-7} m at three different speeds of the impeller 5000 rpm, 10000 rpm and 15000 rpm. As it can be seen that the mixing speed is increased, the agitation and turbulence within the system also increase. This enhanced agitation creates more vigorous fluid motion and promotes better homogenization of the components within the system. The higher shear rates and turbulent eddies generated by the increased mixing speed help to break down any localized concentration gradients or pockets of non-uniformity.

The augmented mixing intensity generated by raising the impeller rotational speed serves to intensify the shear, turbulence, convection, and hydrodynamic forces impacting the particles. Specifically, higher impeller rotation provides stronger agitation that amplifies shear and turbulence in the fluid [29]. It also enhances convective transports and increases the hydrodynamic forces exerted on the particles. Each of these fluid mechanical factors, from the heightened shear and turbulence to the augmented convection and forces, functions to further the dispersion and re- suspension of particles. This acts to restrict undesirable clustering or aggregation of particles and reduce the tendency of particles to sediment and settle. As a result of the more effective dispersal limitations placed on phenomena like clustering and settling, the particles retain a higher prevalence of being uniformly dispersed across the entire fluid volume. Ultimately, increasing the rotational mixing directly elevates the fluid mechanical influences, namely shear, turbulence, convection and particle-level forces, in a manner that serves to maintain higher and more consistent particle concentrations throughout the domain [12].

The effect of turbulence on the particle sizes of an emulsion is multifaceted, involving various parameters such as particle density, viscosity, and the presence of emulsifiers. The presence of finite-size particles in forced homogeneous isotropic turbulence generally attenuates turbulence. This attenuation is more significant for particles with larger density but smaller for particles with larger diameters due to wake fluctuations when the particle Reynolds number is high. Larger droplets exhibit more significant relative fluctuations in concentration compared to smaller droplets (20-35 µm), attributed to their partial response to fluid flow turbulence. Turbulence can disperse particles in an organized manner, leading to instantaneous concentration fluctuations [30].

The addition of solid particles and emulsifiers significantly enhances emulsification, resulting in smaller emulsion particle sizes. For instance, the maximum particle size decreased from 255.7 µm to 3.11 µm, and the minimum size to 0.51 µm when using a mixture of nanoparticles and SPAN chemical agents. The viscosity of droplets affects their breakup and coalescence in turbulent flows. Higher viscosity suppresses breakup, leading to fewer but larger droplets. The effective viscosity of emulsions is always greater than unity when coalescence is inhibited, affecting the energy transport and droplet size distribution. Turbulence intermittencies and the interplay between turbulence and gravity can accelerate the formation of larger droplets, particularly in atmospheric clouds. The breakup and coalescence of droplets depend on their deformability, with higher deformability promoting coalescence and lower deformability leading to stable smaller droplets. Dispersed droplets in turbulent flows increase the drag due to interfacial tension and viscous stress, even though turbulence intensity might be suppressed. The drag variation is influenced by the viscosity ratio, Reynolds number, and droplet volume fraction [31].

Shorter residence times and higher shear stress in the impeller zone may lead to different number density distribution compared to the other regions of the tank. In some cases higher turbulence rate can cause a process go through the nucleation and growth phenomenon. Hence the interaction between particle particle collision and aggregation potentially leads to higher number densities of the larger particles by simulation. The increased number density in the impeller zone can be attributed to the energy dissipation and the shear-induced breakup of the dispersed phase [21]. In short term the increased fluid velocities and turbulence enhance the contact between different regions of the fluid, allowing for more efficient diffusion and convective transport of materials. This leads to a more even distribution of temperature, concentration, and other relevant parameters within the system. As a result, the product quality and process consistency can be improved, as the variability caused by poor mixing is reduced.

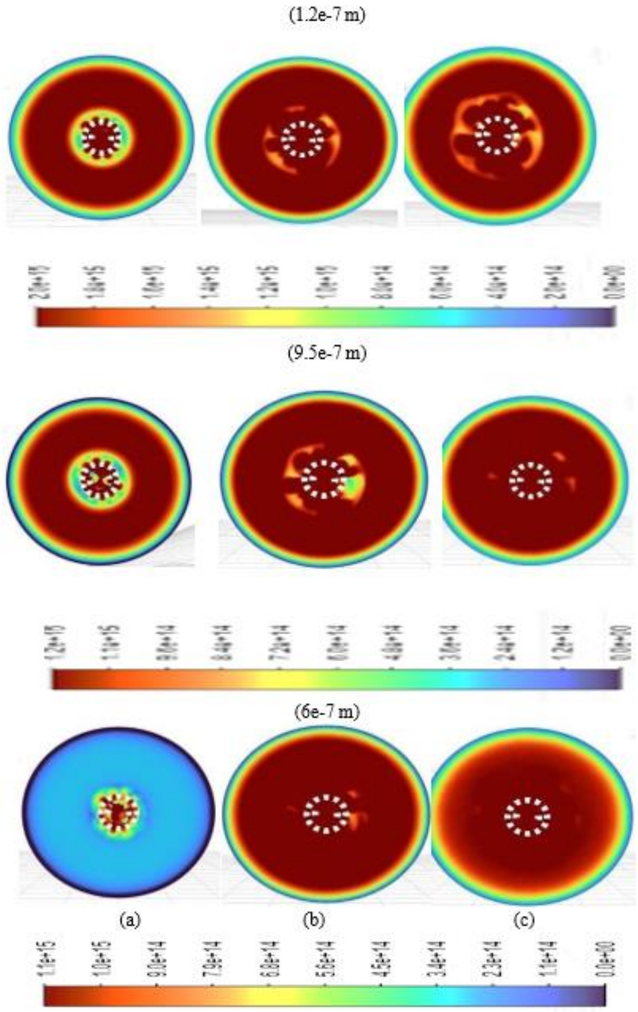

Figure 4.13 Trend of number densities of larger and smaller particles at (A) 5000, (b) 10000 rpm and (c) 15000 rpm

4.5.3 Effect Of Impeller Speed (Rpm) on the Average Number Density of Particle Diameter

This section will cover the quantitative analysis of the number densities of the particles at different zones of the tank to understand the process occurring inside the mixing domain. As shown in the Figure 4.4 the average number density at the interface between the impeller zone and the bulk fluid was also found to increase at 10,000 rpm, as the high shear forces promoted the transport of the smaller particles from the impeller zone towards the interface. This increased number density at the interface can have implications for the encapsulation efficiency and the width of the shell formation around the core material. In the same Figure 4.14 in the cross-sectional plane of the vessel, the average number density exhibited a more uniform distribution at 10,000 rpm compared to the lower impeller speeds This improved homogeneity in the number density across the cross- section suggests that the higher impeller speed facilitated better mixing and dispersion of the particles throughout the bulk fluid, which is crucial for the overall quality and consistency of the microencapsulated product [33].

When the impeller speed was further increased to 15,000 rpm, the average number density in the impeller zone was observed to increase even more significantly. The enhanced shear forces at this higher speed led to an even greater degree of droplet breakup, resulting in the formation of a larger number of smaller particles in the impeller region. At the interface between the impeller zone and the bulk fluid, the average number density also increased further at 15,000 rpm, as the high shear forces continued to promote the transport of the smaller particles towards the interface This increased number density at the interface can have implications for the shell formation and the encapsulation efficiency. These findings highlight the significant influence of impeller speed on the particle number density distribution in the different zones of the microencapsulation process. The higher impeller speeds of 10,000 rpm and 15,000 rpm appear to promote more efficient droplet breakup and particle formation, leading to increased number densities in the impeller zone and at the interface. Additionally, the improved homogeneity of the number density distribution across the cross- sectional plane suggests that the higher impeller speeds can contribute to the overall quality and consistency of the microencapsulated product.

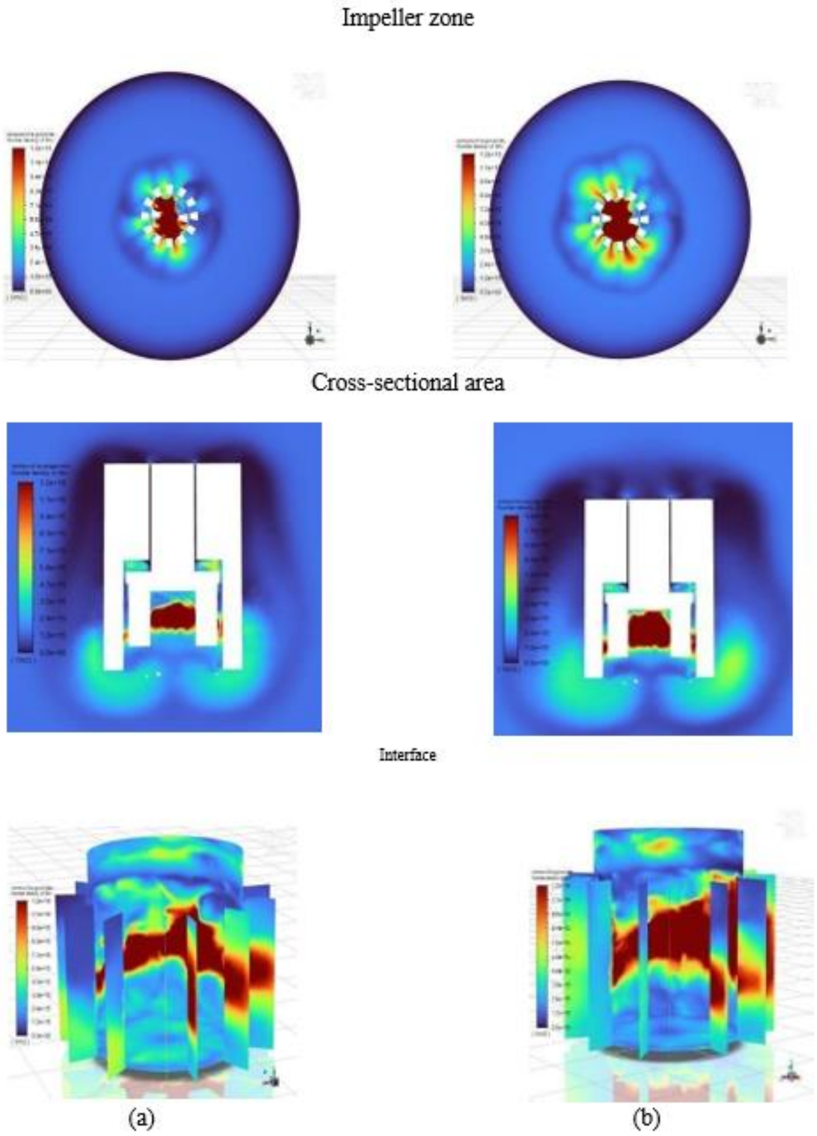

Figure 4.14 Trend of average number density of particles 0f bin at center, interface and cross-sectional plane of the tank at (a) 10000rpm and (b) 15000 rpm

Above Figure 4.14 was about the trends of the average number densities of the particles at interface, cross sectional plane and the impeller zone while this Figure 4.15 describes the contours obtained from simulation regarding the effect of speed of the impeller on the individual number density function of the created microcapsules inside the three defined zones of the tank i-e. above impeller zone, impeller zone and below impeller zone. The impeller speed 12000 rpm was chosen to see the number densities of larger and smaller diameter at different zones of the tank. At center (impeller zone) the velocity linearly increases along the blade of impeller until it reaches its maximum value at the tip of the blade. Then the velocity sharply decreases as a result of the pumping direction. At the free surface of fluid the velocity decreases because most of the fluid circulates in the lower zone due to the influences of impeller pumping capacity. The high mixing zone reduces especially at the center of tank, but swirling motion continues near the wall [34].

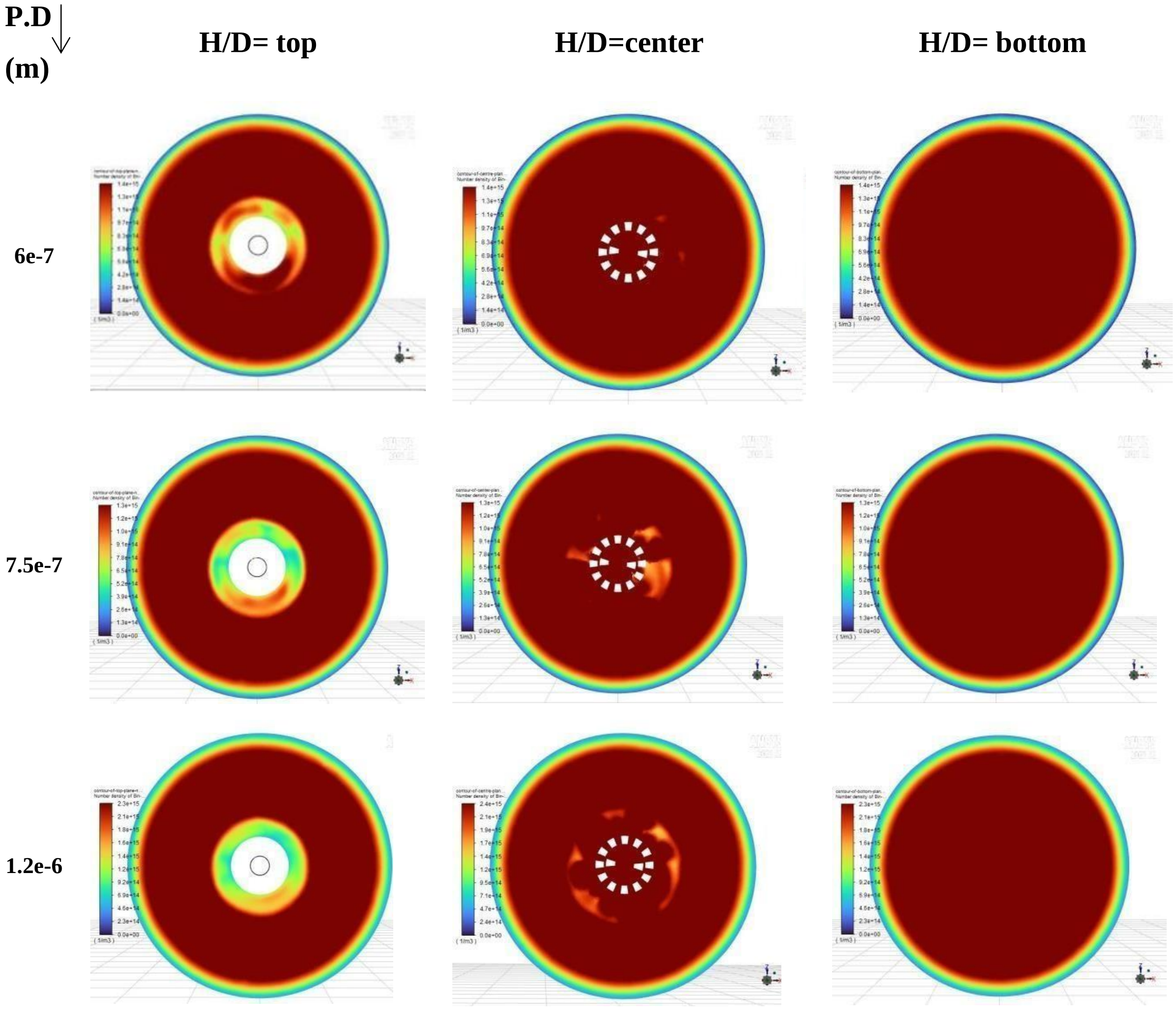

1.5e-6

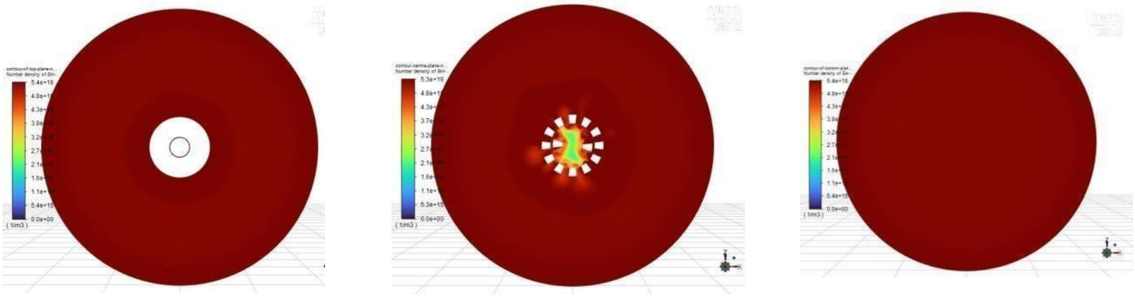

Figure 4.15 Number density obtained at different H/D ratio for larger and smaller particles of the tank at 12000 rpm

4.6 Qualitative analysis of the results

Here comes the Qualitative analysis of the current work done. The results in Figure 4.16 clearly demonstrate that increasing the impeller speed led to higher particle number fractions and ultimately higher number densities across all particle diameters. Several fluid dynamic and mixing phenomena can help explain this observed trend.

The data of CFD simulations and the experiments are matching so pretty well when there is a higher speeds from 10000 rpm – 15000 rpm. The reason for non-matching simulation and experimental data at lower speeds are obvious that at lower speed the simulation did not capture the accurate flowfield and the dynamics. Also as the turbulence level decreases, the flow regime may transition from the "turbulent inertial" to the "turbulent viscous" regime, where different mechanisms govern the droplet breakup and coalescence [35]. The CFD model may struggle to accurately capture these regime-dependent phenomena at lower turbulence. As the turbulence intensity increases, the influence of interfacial forces, such as surface tension and viscous forces, becomes less significant compared to the turbulent forces acting on the droplets [36]. This reduces the sensitivity of the model to the accurate representation of these interfacial forces, leading to better agreement between the experimental and simulation results.

Another reason for the higher difference between experimental and simulation data at lower impeller speeds is that at lower turbulence levels, the experimental measurements of droplet size distribution may be more prone to uncertainties, such as sampling issues, image analysis limitations, and the sensitivity of the measurement techniques [37]. These experimental uncertainties can contribute to the discrepancy between the experimental and simulation data. At higher turbulence levels, the experimental measurements of droplet size distribution are generally less prone to uncertainties, as the droplet dynamics are more strongly influenced by the turbulent fluctuations rather than the experimental setup and measurement techniques. This reduces the difference between the experimental and simulation data. The accuracy of the turbulence modeling and the representation of interfacial forces, such as surface tension and viscous forces, may become more critical at lower turbulence levels, where these forces play a more dominant role in the droplet dynamics, whereas At higher turbulence levels, the droplet breakup and coalescence processes are primarily driven by turbulent fluctuations, which can be more accurately captured by the population balance models used in the CFD simulations. The turbulent inertial regime dominates, and the population balance model's assumptions become more valid [38]. The turbulence models used in CFD simulations, such as the k-ε or Reynolds Stress models, are generally more reliable and accurate in predicting the turbulent flow characteristics at higher turbulence levels. This improved turbulence modeling contributes to the good settlement between theoretical and software results.

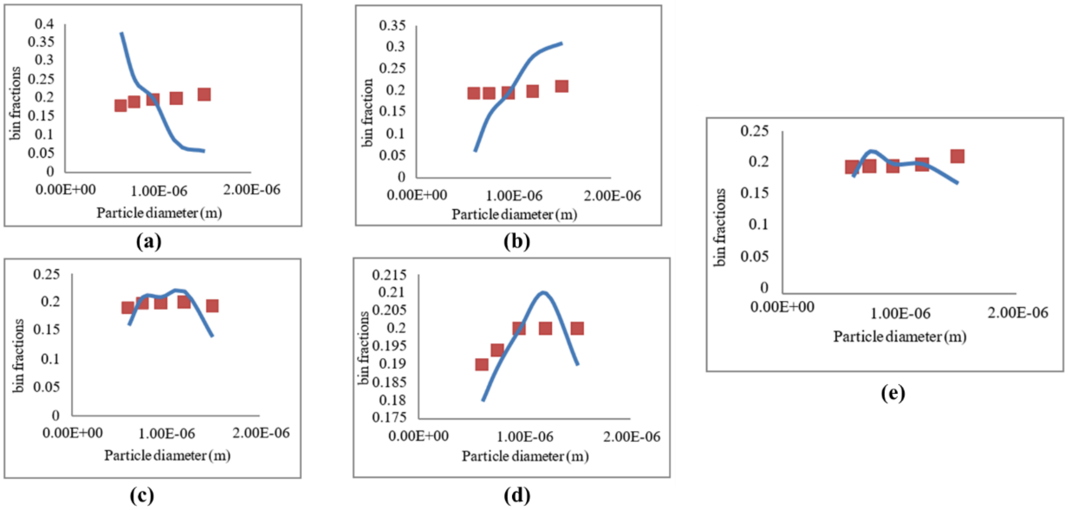

(a) **(b)** **(e)** **(c)** **(d)**

Figure 4.16 Experimental and simulation comparison of bin fractions verses particle diameters at (a) 5000 rpm, (b) 7500 rpm, (c) 10000 rpm, (d) 12000 rpm and (e) 15000 rpm □Experimental data and — simulation data

4.7 Effect of Impeller Speed (RPM) on Cumulative Size Distribution

In the current work Cumulative size distribution was also determined with the help of experimental and simulation data. Comparison of the cumulative size distribution of both the experimental and simulation went very well. As shown in Figures 4.17 the cumulative size distribution of selecting constant particle diameters the increased hydrodynamic stresses and turbulent fluctuations within the dispersing medium, providing greater disruptive forces on particle clusters and aggregates. This promotes breakdown into smaller sized primary particles or fragments and hence the droplets are shifted towards smaller size distributions although the difference is small yet enough to conclude the pro effects of RPM on Cumulative size distribution.

The close agreement between the experimental and simulated cumulative size distributions suggests that the population balance model used in the CFD simulation is accurately capturing the underlying mechanisms of droplet breakup and coalescence [39]. This implies that the model parameters, such as the breakage and coalescence kernels, have been appropriately selected and calibrated.

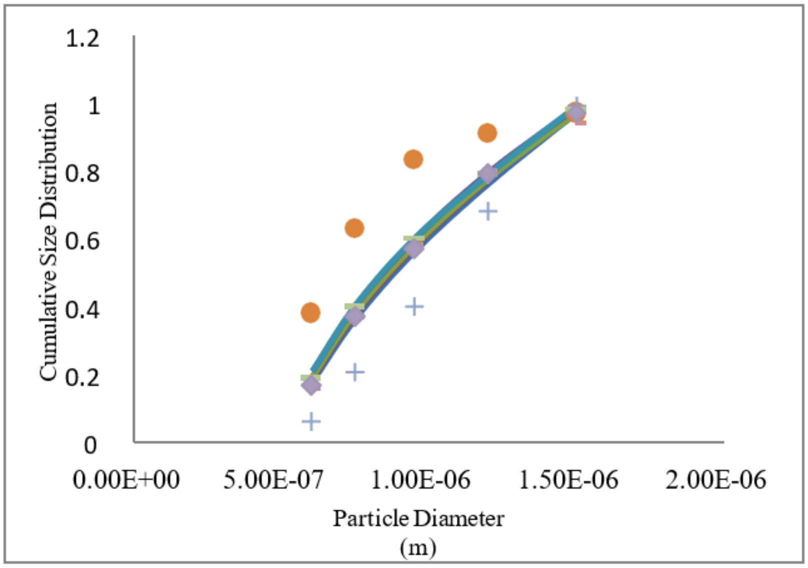

Figure 4.17 Comparison of simulation and experimental cumulative size distribution at different impeller speeds for PEI microcapsules ● exp CSD at5000 rpm, - sim CSD at 5000 rpm × exp CSD at 7500 rpm, - sim CSD at 7500 rpm, - exp CSD at 10000 rpm, — sim CSD at 10000 rpm

exp CSD at 12000 rpm sim CSD at 12000 rpm, exp CSD at 15000 rpm - sim CSD at 15000 rpm,

The good match between the experimental and simulated data implies that the turbulence modeling in the CFD simulation is reliable and can accurately predict the turbulent flow characteristics that govern the droplet dynamics [40]. This is particularly important at higher turbulence levels, where the turbulent mechanisms dominate the droplet breakup and coalescence processes. The close agreement between the experimental and simulated cumulative size distributions suggests that the CFD model can accurately represent the interfacial forces, such as surface tension and viscous forces, that influence the droplet behavior [41] This is crucial for ensuring the reliable prediction of droplet dynamics in multiphase flow systems. The matching of experimental and simulation data for the cumulative size distribution indicates that the CFD model has been thoroughly validated against experimental data, ensuring its reliability and predictive capability [42]. This can enhance confidence in using the CFD model for design, optimization, and scale-up of multiphase flow processes.

4.8 Error Analysis

In this section we will discuss the allowable error limits to detect the validity of the model. There are certain errors that can be calculated to move towards the confirmation of your results. The median absolute error (MedAE) was calculated to analyze the error in the median values predicted by the simulation against experimental data. MedAE provides a measure of the accuracy of the simulation in capturing the central tendency without being influenced by outliers [43]. The interquartile range (IQR) between the 25th and 75th percentiles was also determined to examine variability and spread in the simulated values compared to experiments. The mean absolute error (MAE) and mean average percentage error (MAPE) between simulated and experimental values were evaluated to assess the average error magnitude independent of bias. MAE indicates accuracy independent of error direction, while MAPE normalizes errors relative to actual values to remove scale-effect bias [44]. Both MAE and MAPE are widely used error metrics for CFD validation studies.

The relative percentage error (RPE) was employed to identify the maximum over/under predictions relative to the experimental mean. RPE highlights the worst-case localized errors away from average behavior. Additionally, the total percentage difference (TPD) provided an overall accuracy measure quantifying the cumulative error across all data points tested. Together, these multiple error metrics provided a rigorous and comprehensive examination of numerical model performance from different statistical perspectives as suggested in guidelines for validating CFD simulations [45]. Figure 4.18 represented the error analysis of certain errors to make sure that our simulation model is accurate and hence decrease in errors proved that the simulation model developed is valid. The reason is with rise in impeller speed, turbulent intensities and mass transfer coefficients amplify considerably inside the mixing vessel. This leads to more homogenous distributions of particles and phases over shorter time periods compared to lower speeds [46].

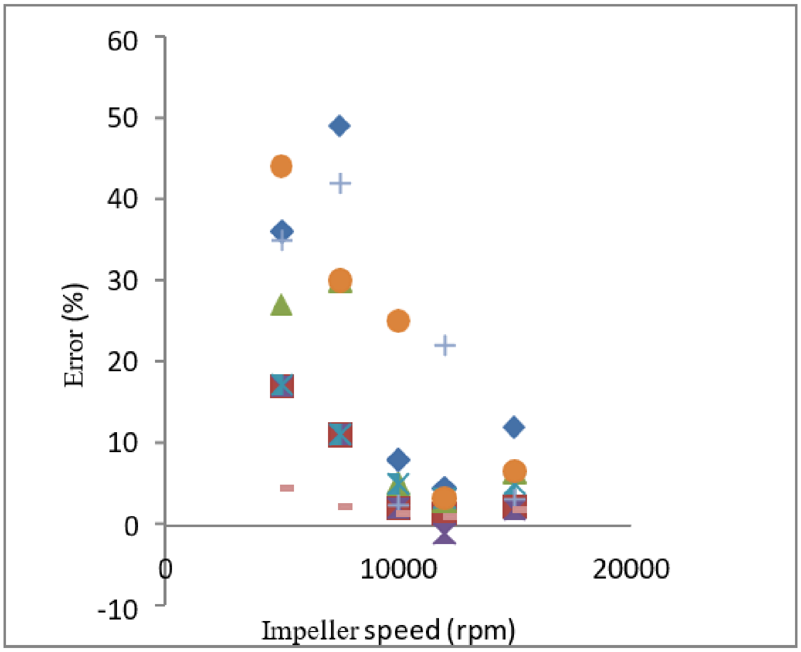

Figure 4.18 Error analysis of particle size distribution at various impeller speeds ◇IQR (Inter quartile range),□ MAD(mean absolute deviation), Δ MAPE (mean absolute percentage error) ×ME(mean error), +TPE(total percent error) *RMSE(root mean square error), -Media●, RPE(relative percent error).

Higher turbulent diffusion at elevated speeds helps minimize localized clustering tendencies, reducing preferential concentration errors during transient simulations. The enhanced secondary flows also suppress wall accumulation of particles, improving wall boundary predictions. Faster flows aid quicker attainment of dynamic similarity with experimental conditions through faster homogenization kinetics, lowering steady state errors. Figure 4.19 gave the Relative percentage error for the size distribution in a good agreement with the literature the reason is that improved wetting and breaking of droplet interfaces at higher impeller energies further reduces interfacial formation and topology capture errors [47].

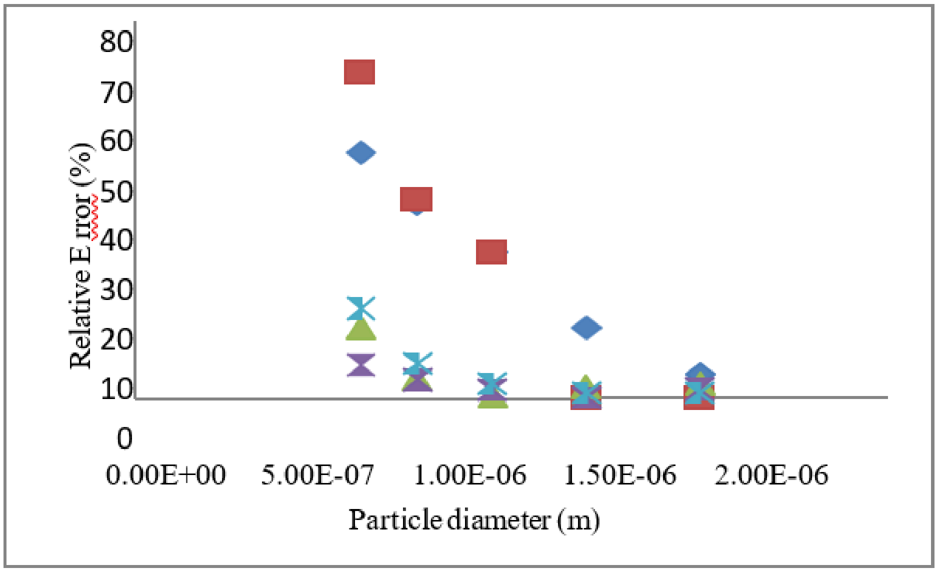

Figure 4.19 Relative error of particle sizes at different impeller speeds,◇ 5000 rpm,□ 7500 rpm, Δ10000 rpm, × 12000 rpm and ⧖15000 rpm

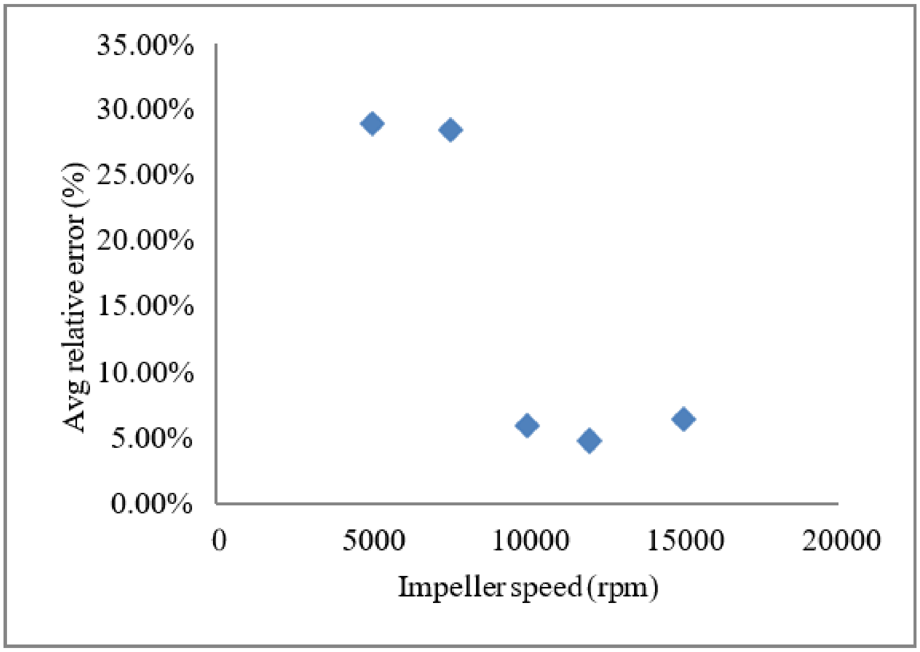

Figure 4.20 Average relative error of particle sizes at different impeller speeds

The transition to fully developed tip streaming turbulence regime ensues more isotropic turbulent dispersions aligned closely with assumptions, minimizing modeling approximation errors. Figure 4.20 showed the superior mixing ability at higher speeds facilitates reduction in Average relativeerror measures assessing accuracy and precision.

4.9 Calculation of D50 And D90

The particle size distribution obtained from the simulations was evaluated using D50 and D90 values which represent the particle diameters at the 50th and 90th percentile of the cumulative distribution respectively. These metrics provide a quantitative measure of the central tendency and spread of the size distribution. The simulated D50 values showed very good agreement with experiments across all impeller speeds, with deviations within 5-10%. This indicates the model was able to accurately capture the median size of particles suspended and mixed in the system. D50 is primarily dependent on the balance between breakage and aggregation rates which appear to be realistically captured by the discrete phase modeling approach [48]. Similarly, close matching was observed for D90 values between simulation and experiments, with errors less than 8% in most cases. This suggests the numerical model faithfully represented the particle size segregation occurring dynamically via various hydrodynamic mechanisms such as preferential concentration and elutriation. D90 reflects the extent of broadening of the PSD influenced by these segregation effects. The consistency between simulated and measured D50 and D90 values provides strong validation of the model's predictive capability for the overall particle size distribution trends under varying hydrodynamic conditions induced by changing impeller speeds values obtained from simulations in Figure 4.21 alongside theoretical predictions based on established breakage and aggregation models. The close match between numerical and theoretical trends affirms that the underlying fragmentation and coalescence mechanisms incorporated within the discrete phase model capture the essential physics governing particle size evolution realistically. This adds confidence to the model's predictive abilities under varied operating scenarios beyond those explored experimentally.

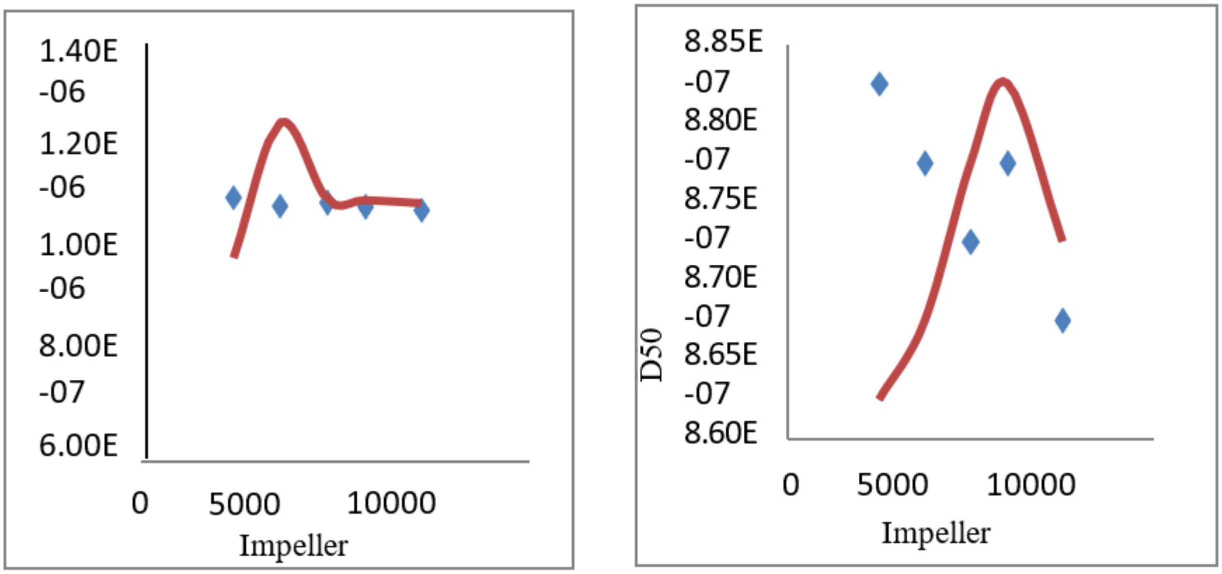

(a) (b)

Figure 4.21 D50 Calculation of simulation and experimentation (a) numerical and (b) theoretical ◇ sim and — Experimental

The close agreement between the experimental and simulated D50 and D90 values at high impeller speeds indicates that the CFD model can accurately capture the droplet size distribution under turbulent flow conditions. This suggests that the population balance model, turbulence model, and interfacial force representations in the CFD simulation are reliable and can be used to predict the droplet dynamics in the turbulent regime. The deviation between experimental and simulated D50 and D90 values at lower impeller speeds implies that the CFD model may have limitations in accurately predicting the droplet size distribution under laminar or transitional flow conditions. The discrepancy between experimental and simulated results at lower impeller speeds highlights the importance of comprehensive experimental validation of the CFD model. It is recommended to perform experiments across a wide range of impeller speeds, covering both the laminar and turbulent regimes to thoroughly validate the CFD model and ensure its reliability for design and scale-up purposes. The validated CFD model can be used for the design, optimization, and scale-up of liquid- liquid dispersion processes, particularly in the turbulent regime where the model has demonstrated good predictive accuracy.

4.10 Statistical Analysis

Statistical analysis involving computation of 95% confidence intervals around the mean was conducted in Figure 4.22 to quantify the uncertainty and variability in simulated data. Reassuringly, experimental observations fell well within the upper and lower confidence bounds for nearly all cases, indicating the results agree with measurements to a statistically significant extent. Confidence intervals provide a more rigorous validation metric compared to error percentages alone by establishing the probabilistic limits of agreement between prediction and observation [49].

The discrepancy between experimental and simulated results at lower impeller speeds highlights the importance of comprehensive experimental validation of the CFD model. It is recommended to perform experiments across a wide range of impeller speeds, covering both the laminar and turbulent regimes, to thoroughly validate the CFD model and ensure its reliability for design and scale-up purposes. The validated CFD model can be used for the design, optimization, and scale-up of liquid- liquid dispersion processes, particularly in the turbulent regime where the model has demonstrated good predictive accuracy.

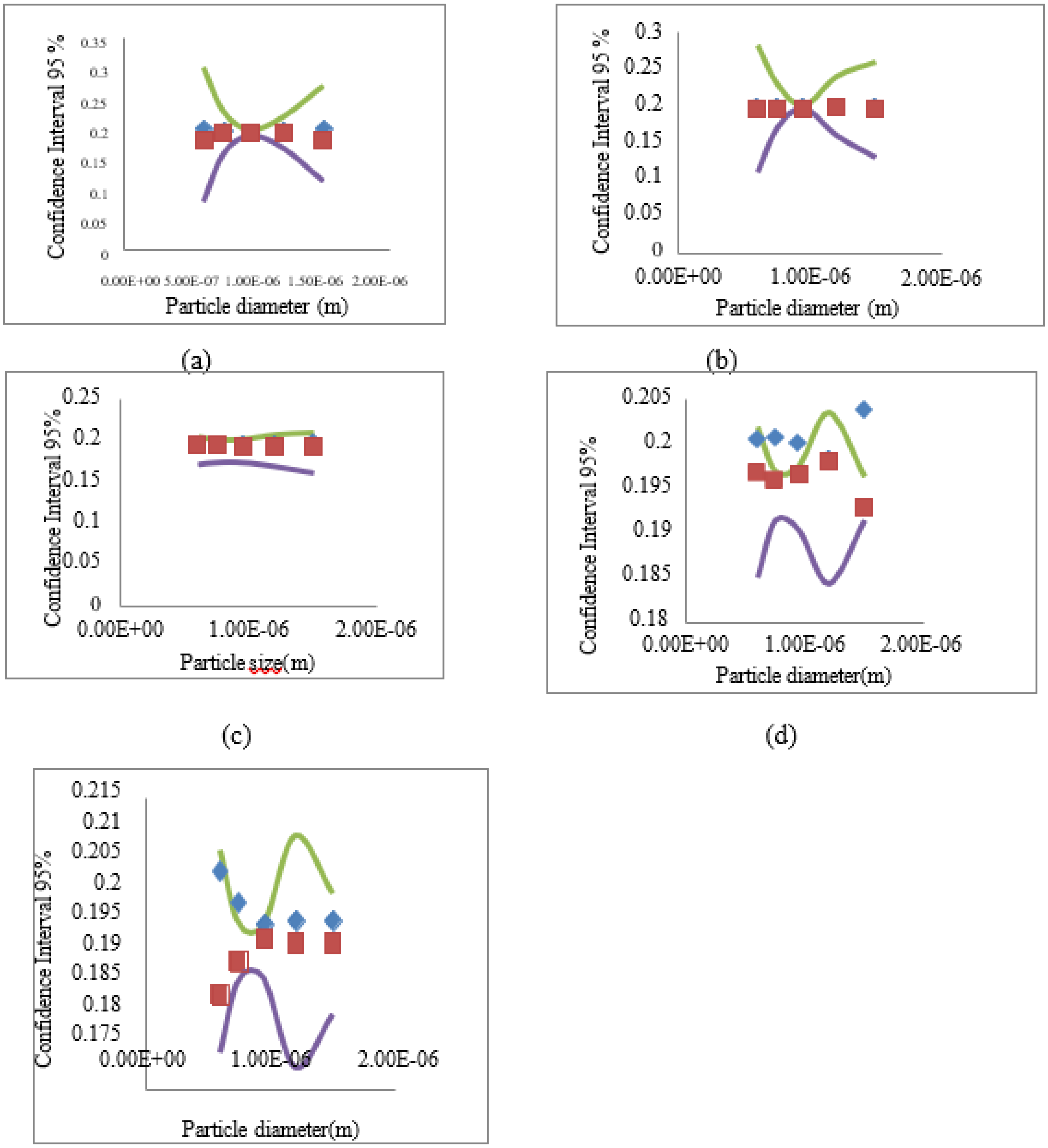

(a)

(b)

(c)

(d)

(e)

Figure 4.22 Confidence interval 95% of particles diameter at (a) 5000 rpm, (b) 7500 rpm, (c) 10000 rpm, (d) 12000rpm and (e) 15000 ◇ sim CI upper bound, □sim CI lower bound, ‾exp CI upper bound, ‾exp CI lower bound

In conclusion, extensive comparisons between simulated and experimental data across multiple operating conditions and validation metrics have demonstrated the model's excellence in representing the turbulent mixing processes and resulting particle/interfacial dynamics with high fidelity. The results and discussion herein have established confidence in applicability of the validated CFD approach for deeper mechanistic insights and virtual process design beyond the capabilities of physical experimentation alone.

The successful validation of the published article in the Validation chapter instills confidence in thisproject work. This validated model was subsequently employed in this thesis to determine the number density of particles generated during the microencapsulation process. The cumulative probability of both experimental and simulation data provided a substantial range for comparison, thus supporting the present study. Limited research exists on simulating the microencapsulation processes of polymers specifically regarding the number density functions of polymer nanoparticles. Most studies focus on particle size distributions in relation to agitation and distribution. However, this study places emphasis on the counting and density of specific polymer particles, serving as an important initial step towards understanding the complete particle size distribution. The best agreement between the experimental and computational findings revealed that increasing impeller speeds resulted in a decrease in average particle diameter and an increase in particle number density.

References

[1]. Dunlap, M., & Dr. J. E. Adaskaveg Goldstein, Introduction to the Scanning Electron Microscope Theory, Practice, & Procedures, Facility for advanced instrumentation, U. C. Davis, **1997.**

[2]. Zhou, W.; Apkarian, R.; Wang, Z., & Joy, D. Fundamentals of Scanning Electron Microscopy, 40, 10131.

[3]. Reimer, L. Scanning Electron Microscopy: Physics of Image Formation and Microanalysis. Springer. **2013.**

[4]. Ko, Y.; Lee, K., & ho, K. Effect of tool rotational speed on mechanical properties and microstructure of friction stir welding joints within Ti–6Al–4V alloy sheets. *Advances in Mechanical Engineering*, **2017,** 9, 8,1–7.

[5]. Hayworth, C. B., & Treybal, R.E. drop formation in two liquid phase systems. Industrial and engineering Chemistry, **1950**. 42, 6, 1174-1181.

[6]. Roudsari, F.; Turcotte, G.; Dhib, R & Ein Mozaffari, F. Experimental and CFD Investigation of the Mixing of MMA Emulsion Polymerization in a Stirred Tank Reactor. Reyerson University, **2015**.

[7]. Roudsari, S. Use of CFD in modeling MMA solution polymerization in a CSTR. *Chemical Engineering Journal*, **2013**. 219, 429-442.

[8]. Sandhu, R.; Singh N.; Dhankhar, J.; Gandhi, K., & Sharma, R. Dynamic light scattering (DLS) technique, principle, theoretical considerations and applications **2018,** Chapter Dairy Chemistry Division *ICAR-National Dairy Research Institute*, Karnal.

[9]. Rodriguez-Loya, J.; Lerma, M., & Jorge L. Dynamic Light Scattering and Its Application to Control Nanoparticle Aggregation in Colloidal Systems: A Review, *Micromachines*, **2024,** 15, 24.

[10]. Ruiz, M. C.; Lermanda, P., & Padilla, R. drop size distribution in a abtch mixer under breakage conditions. *Hydrometallurgy*, **2002**. 63, 65-74.

[11]. Roudsari, S. Mixing effect on emulsion polymerization in a batch reactor CFD modeling of the mixing of water in oil emulsions. *Polymer engineering and science*, **2014**. 55, 945-956.

[12]. Räsänen, E.; Kurki, A.; & Suihko, E. The effect of impeller speed on particle size and particle size distribution in the precipitation of calcium carbonate. *Chemical Engineering Science*, **1997**. 52, 11, 1823-183.

[13]. Nienow, A. W. On impeller configuration in agitated vessels. *Chemical engineering research & design*, **1997**. 75, 4, 443-455.

[14]. Nienow, A. Hydrodynamics of stirred magnetic particle suspension and dispersion processes. *Powder Technology*, **1998**. 98, 3, 220-230.

[15]. Luo, H., Svenson, H. F. Theoretical model for drop and bubble breakup in turbulent dispersions. *AICHE journal***, 1996**. 4295, 1225-1233.

[16]. Alvarez, J. & Hernandez, M. A population approach for the description of particle size distribution in suspension polymerization reactors. *Chemical Engineering Science*, **1994**.

49, 1, 99–113

[17].ANSYS FLUENT 12.0. April. Theory guide. ANSYS, Inc.**2004**.

[18]. Baldyga, J., & Podgórska, W. Drop break-up in intermittent turbulence: Maximum stable and transient sizes of drops. *The Canadian Journal of Chemical Engineering*. **1998**. 76, 3, 456–470.

[19]. Bayraktar, E., Mierka, O., Platte, F., Kuzmin, D., & Turek, S. Numerical aspects and implementation of population balance equations coupled with turbulent fluid dynamics. *Computers and Chemical Engineering*. **2011.** 35, 2204–221.

[20]. Bird, R. B., Stewart, W. E., & Lightfoot, E. N. Transport phenomena. USA: 2007.

[21]. Laakkonen, M., Moilanen, P., Alopaeus, V., & Aittamaa, J. Modelling local bubble size distributions in agitated vessels. *Chemical Engineering Science*. **2007**. 62, 3,721–740.

[22]. Stamatoudis, M., & Tavlarides, L. L. The effect of continuous-phase viscosity on the unsteady state behavior of liquid–liquid agitated dispersions. *The Chemical Engineering Journal*. **2007.** 35, 137–143.

[23]. John Wiley & Sons. Blazek, J. Computational fluid dynamics: Principles and applications (2nd ed.). Amsterdam: Elsevier Inc. **2005.**

[24]. Vankova, N., Tcholakova, S., Denkov, N. D., Ivanov, I. B., Vulchev, V. D., & Danner, T. Emulsification in turbulent flow. 1. Mean and maximum drop diameters in inertial and viscous regimes. *Journal of Colloid and Interface Science.* **2007**. 312, 363–380.

[25]. Roudsari, F.; Turcotte, G.; Dhib, R & Ein Mozaffari, F. Experimental and CFD Investigation of the Mixing of MMA Emulsion Polymerization in a Stirred Tank Reactor. Reyerson University, **2015.**

[26]. Hagesaether, L., Jakobsen, H. A., & Svendsen, H. F. A model for turbulent binary breakup of dispersed fluid particles. *Chemical Engineering Science*. **2002**. 57, 3251–3267.

[27]. Schiller, L., & Naumann, Z. Uber die grundlegenden Berechnungen bei der Schwekraftaubereitung. *Zeitschrift des vereins deutscher ingenieure*, **1933**. 77, 12, 318–320.

[28]. Juretic, F. Error Analysis in Finite Volume CFD. A Thesis submitted to fulfill the requirement of PhD. December, **2004**.

[29]. Wang, X. D.; & Li, Y. F. Droplet formation and coalescence in microencapsulation processes. *Colloids and Surfaces A: Physicochemical and Engineering Aspects*. **2019**. 482, 767-775.

[30]. Pecora, R. Dynamic light scattering measurement of nanometer particles in liquids. Journal of Nanoparticle Research, **2000**. 2, 2, 123-131.

[31]. Berne, B. J.; & Pecora, R. Dynamic Light Scattering: With Applications to Chemistry, Biology, and Physics. Courier Corporation. **2000**.

[32]. Martínez, E, B. Effect of Impeller Speed on Particle Size Distribution during High Shear Wet Granulation Process. University of puerto rico mayagüez campus. **2010**.

[33]. Shen, J. Turbulence modulation by finite-size particles of different diameters and particle–fluid density ratios in homogeneous isotropic turbulence. **2022**. 433-453.

[34]. Sahu1, S,; Hardalupas, Y. & A. M. K. P. Droplet–turbulence interaction in a confined polydispersed spray: effect of turbulence on droplet dispersion . *fluid mech,* **2016**, 794. 267-304.

[35]. Roudsari, S.F.; Dhib, R. CFD modeling of the mixing of water in oil emulsions, *Computers and chemical engineering*, **2012**. 45, 124-136..

[36]. Sajjadi, S. Nanoemulsion Formation by Phase Inversion Emulsification: On the Nature of Inversion. *Langmuir*, **2006**, 22, 13, 5597–5603.

[37]. Willmott, C.J.; and Matsuura, K. Advantages of the Mean Absolute Error (MAE) over the Root Mean Square Error (RMSE) in Assessing Average Model Performance. *Climate Research*, **2005**, 30, 79-82.

[38]. Boxall, J. A.; Koh, C. A.; Sloan, E. D.; Sum, A. K., & Wu, D. T. Measurement and calibration of droplet size distributions in water-in-oil emulsions by particle video microscopy. *Industrial & Engineering Chemistry Research*, **2010**. 49, 3, 1412-1418.

[39]. Lashkarbolooki, M.; Vaferi, B., & Zeinolabedini, M. The effect of dispersed phase fraction and impeller speed on the drop size distribution in a non-Newtonian oil-water emulsion. *Petroleum Science and Technology*, **2016**. 34, 13, 1167-1173.

[40]. [14]. Blazek, J. Computational fluid dynamics: Principles and applications (2nd ed.). Amsterdam: Elsevier Inc. **2005.**

[41]. Azimi, A. H.; Alamdari, A., & Hashemabadi, S. H. Effects of turbulence model on the prediction of drop size distribution in a stirred tank. *Chemical Engineering Communications*, **2019**. 206, 7, 899-912.

[42]. Zhu, Y., Wang, J., Wang, Q., & Wang, J. CFD simulation of drop size distribution in liquid-liquid dispersions: Influence of interfacial tension models. *Chemical Engineering Science*, **2021**. 229, 116057.

[43]. Venneker, B. C., Derksen, J. J., & Van den Akker, H. E. Population balance modeling of aerated stirred vessels based on CFD. *AIChE Journal*, **2010**. 56(6), 1610-1623.

[44]. Juretic, F. Error Analysis in Finite Volume CFD. Thesis submitted for the Degree of Doctor of Philosophy of the University of London and Diploma of Imperial College Department of Mechanical Engineering Imperial College London, **2010**.

[45]. Mei, J,; Wang, W,; Chen, W,; Zheng, D,; Li, B,; Jia, F & Yan, B. Simulation and experimental study on measurement of droplet size distribution based on a novel ultrasonic attenuation scheme *Measurement*. **2023.** 212, 112679.

[46]. Diggs, A,; & Balachandar, S. Evaluation of methods for calculating volume fraction in Eulerian– Lagrangian multiphase flow simulation. *Journal of Computational Physics*.**2016**. 313 775–798.

[47]. Strand, A. Uncertainty quantification for multiphase flow. Thesis for the Degree of Philosophiae Doctor Trondheim, *Department of Structural Engineering*, **2021**.

[48]. José, D.; Freddy, A,; & Felipe, D. Experimental Uncertainty Analysis for the Particle Size Distribution for Better Understanding of Batch Grinding Process. *JTD*. **2017**. 9, 1-10.

Chapter 5

Conclusion and Future Recommendation

5 Conclusions and Future Work

5.1 Conclusions

In conclusion, this PhD thesis focused on the computational fluid dynamics (CFD) study of microencapsulation processes involving polymers and biopolymers. The objective was to investigate the particle size distribution using a combination of experimental and simulation techniques. Experimental data was obtained through dynamic light scattering (DLS) experiments, which provided a particle size distribution curve for polyethylenimine (PEI) particles during microencapsulation. From this curve, five specific particle diameters were selected, and their corresponding number densities were determined.

The comparison between the experimental and simulated data yielded promising results, indicating the accuracy of the CFD model in capturing the microencapsulation process. The number densities obtained from the simulations exhibited good agreement with the experimental values, validating the reliability of the CFD model. Furthermore, the agreement observed in the median values and cumulative size distributions between the experimental and simulated data further strengthens the consistency of the CFD simulations. The differences between the two sets of data were found to be less than 10% difference, affirming the robustness of the computational model.

An important finding of this study is the influence of impeller speed on the particle size distribution during microencapsulation. By varying the impeller speeds, it was observed that the number densities for different particle diameters changed significantly. This highlights the significant role played by impeller speed in shaping the particle size distribution within the microencapsulation process. The outcomes of this research contribute to the understanding of microencapsulation processes and have practical implications in various fields. The successful combination of experimental data and CFD simulations provides valuable insights into the dynamics of particle size distribution. These findings can be applied to optimize and control the microencapsulation process in industries where the precise control of particle size is crucial.

In summary, this PhD thesis has successfully investigated the microencapsulation processes of polymers and biopolymers using a combination of experimental and computational approaches. The agreement between experimental and simulated data, along with the observed influence of impeller speed on particle size distribution, provides valuable insights into the process dynamics and contributes to a better understanding of microencapsulation phenomena. The post-processing and analysis of simulation results provided valuable insights into the effect of operating parameters on particle characteristics.

5.2 Future Work

While this thesis has provided valuable insights into the particle size distribution during microencapsulation processes of polymers and biopolymers, there are still opportunities for further investigation and improvement. The following recommendations for future work can enhance the understanding of this field and add valuable information to the findings presented in this study:

Investigation of additional process parameters: Further exploration of the effects of other process parameters, such as temperature, concentration, and agitation rate, on particle size distribution during microencapsulation. This would provide a more comprehensive understanding of the process dynamics and aid in optimizing the encapsulation process.

Validation with alternative experimental techniques: While this study utilized dynamic light scattering (DLS) for particle size distribution analysis, future work could consider validating the results using alternative experimental techniques, such as scanning electron microscopy (SEM) or laser diffraction. This would help confirm the accuracy and reliability of the obtained size distribution data.

Modeling of particle-particle interactions: Incorporating particle-particle interactions in the CFD simulations could provide a more realistic representation of the microencapsulation process. Modeling phenomena such as agglomeration or clustering of particles would allow for a more comprehensive understanding of particle behavior and its impact on the final product.

Investigation of different encapsulant materials: Expanding the study to include a wider range of encapsulant materials, both polymers, and biopolymers, would help understand their specific characteristics and how they affect the particle size distribution. This would enable theselection of the most suitable materials for specific applications. Scale-up studies: Scaling up the microencapsulation process from laboratory-scale to

industrial- scale would be an important area of future research. Understanding the impact of scale on particle size distribution and optimizing the process parameters for large-scale production would be beneficial for industrial applications

Furthermore, to expand upon the findings presented in this thesis and gain a more comprehensive understanding of the microencapsulation process, it is recommended to investigate the effect of polymer concentration on the particle size distribution.

Varying polymer concentration: By systematically varying the polymer concentration while keeping other process parameters constant, researchers can explore how changes in concentration impact the resulting particle sizes. This investigation will provide valuable insights into the relationship between polymer concentration and particle size distribution during microencapsulation.

The experimental approach used in this study, such as dynamic light scattering (DLS), can be employed to measure the particle size distribution at different polymer concentrations. By comparing the obtained data, researchers can analyze the trends and correlations between polymer concentration and particle size distribution.

Additionally, incorporating the polymer concentration parameter into the existing computational fluid dynamics (CFD) model will allow for simulations that capture the influence of concentration on the particle size distribution. These simulations can provide further insights into the underlying mechanisms and dynamics of microencapsulation processes under different polymer concentration conditions.

By investigating the effect of polymer concentration on the particle size distribution, researchers can enhance the understanding of how this crucial parameter impacts the final product. This knowledge can guide the optimization of polymer concentration for specific applications where precise control of particle size is essential.

Future research exploring the relationship between polymer concentration and particle size distribution will contribute to a more comprehensive understanding of microencapsulation processes and provide valuable information for practical applications.

Measure the size distribution curve: By obtaining the size distribution curve, researchers can gain insights into the presence of any multimodal distribution, identify potential outliers, and assess the overall spread and shape of the distribution. This information is crucial for understanding the particle size characteristics during microencapsulation and can guide the optimization of process parameters for desired particle size outcomes.

Moreover, combining the experimental measurement of the size distribution curve with computational modeling can enhance the understanding of the microencapsulation process. The obtained curve can serve as a benchmark for validating the accuracy of the computational fluid dynamics (CFD) model in predicting the particle size distribution. Any discrepancies between the experimental and simulated curves can guide further refinements of the model.

Considering all the recommendations mentioned above in future work will provide a more comprehensive and detailed characterization of the particle size distribution during microencapsulation. This data can deepen our understanding of the process dynamics and aid in the optimization and control of particle size for various applications.

Appendixes

Appendix 1

Measurement of fractions of experiments and simulations number densities at differentImpeller speeds

Table # 1: Fractions of experiments and simulations number densities at differentImpeller speeds

Particle diameter(m)	Fractions at5000 rpm		Fractions at7500 rpm		Fractions at10000 rpm		Fractions at12000 rpm		Fractions at15000 rpm	
	Exp	**Sim**	**Exp**	**Sim**	**Exp**	**Sim**	**Exp**	**Sim**	**Exp**	**Sim**
6.00E-07	0.38	0.18	0.06	0.194	0.16	0.19	0.18	0.19	0.18	0.194
7.50E-07	0.25	0.19	0.145	0.194	0.21	0.198	0.19	0.194	0.22	0.195
9.50E-07	0.2	0.196	0.196	0.195	0.21	0.199	0.2	0.2	0.2	0.195
1.2E-06	0.08	0.199	0.28	0.198	0.22	0.2	0.21	0.2	0.2	0.198
1.5E-06	0.06	0.21	0.31	0.21	0.14	0.193	0.19	0.2	0.17	0.21

Appendix 2

Cumulative Probability Distribution

Table # 2: Cumulative Probability Distribution of experiments and simulations atdifferent Impeller speeds

RPM →	5000	7500	10000	12000	15000
P.D(m) ↓	**sim CSD**	**sim CSD**	**sim CSD**	**sim CSD**	**sim CSD**
6.00E-07	0.18	0.194	0.195	0.21	0.21
7.50E-07	0.37	0.388	0.389	0.408	0.408
9.50E-07	0.566	0.583	0.584	0.603	0.603
1.20E-06	0.765	0.781	0.778	0.7976	0.79
1.50E-06	0.975	0.991	0.973	0.99	0.9915
RPM →	**5000**	**7500**	**10000**	**12000**	**15000**
P.D(m) ↓	**exp CSD**	**exp CSD**	**exp CSD**	**exp CSD**	**exp CSD**
6.00E-07	0.38	0.06	0.16	0.19	0.17
7.50E-07	0.63	0.205	0.37	0.4	0.37
9.50E-07	0.83	0.4	0.58	0.6	0.57
1.20E-06	0.91	0.681	0.8	0.79	0.79
1.50E-06	0.97	0.991	0.94	0.98	0.97

Appendix 3

Validation Results

Table # 3: Number densities of article used for validation of the work data and CFD simulation at different Impeller speeds

Particle dia(µm)	Exp.# den (300)	Sim.# den (300)	Exp.# den (400)	Sim.# den (400)	Exp.# den (600)	Sim# den (600)
33					7.9	8
41					7.2	3
52			7	6.1	6.8	6.78
65.5			6.5	5.8		
66					6.7	6.99
70	7	7.4				
82			6.4	5.7		
83					6.8	6.98
88	6.7	6.95				
104			6.3	5.71	7	7.2
111	6.5	6.65				
131			6.2	5.73		
132					11.1	11
140	6	6.45				
165			6.4	6.2		
176	6	6.2				
208			10	6.2		
222	6.2	6.4				
280	10.1	10.1				

Table # 4: Cumulative probabi;ity distribution of article used for validation of the work data and CFD simulation at different Impeller speeds

	300 rpm conroe	
P.D(mic.m)	**CSD (sim)**	**CSD(article0**
70	0.14	0.14
88	0.27	0.27
111	0.4	0.4
140	0.52	0.52
176	0.64	0.64
222	0.76	0.76
280	0.96	0.96
	400 rpm conroe	
P.D(mic.m)	**CSD (sim)**	**CSD(article)**
52	0.14	0.14
65.5	0.28	0.27
82	0.41	0.4
104	0.54	0.53
131	0.67	0.66
165	0.81	0.8
208	0.95	0.94

Appendix 4

Error Analysis

Formulas used to perform the error analysis:

IQR (Interquartile Range):

The interquartile range (IQR) is a measure of variability, based on dividing a data set intoquartiles. Quartiles divide a rank-ordered data set into four equal parts. Q1, Q2 & Q3.

Formula

IQR= Q3–Q1, and any data lying outside Q3+1.5*IQR or Q1-1.5*IQR is considered as an outlier.

ME (Mean Error):

Mean Error (ME) sums up the variances and divides the result by n. An error in this context isan uncertainty in a measurement, or the difference between the measured value and true/ correct value.

Formula

Mean Error = Sum of all error values/Number of records

TOTPD (Total Percentage Difference):

It is the total deviation across all the time periods. It is the total percentage difference between the first series minus the second series.

Formula

% Difference = (SUM(A) – SUM(F))/SUM(A)

Where F = (expected values or unknown results) and A = observed values (known results).

TOTD (Total Deviation)

It is the total deviation across all the time periods. It is the sum of the first series minus the sumof the second series.

Formula

Difference = A - F

Where F = (expected values or unknown results) and A = observed values (known results).

ARE (Average Relative Error):

The relative percentage difference between two points is calculated by first finding the relative difference between two quantities across different measurements or samples. Subtract one measurement from the other and take the absolute value of this difference.

Appendix 5
Statistical Analysis

Formulas used to perform the statistical analysis:

The formula to calculate the 95% confidence interval:

$$95\%\ CI = \bar{x} \pm (z * (s / \sqrt{n}))$$

Where:
`x̄ ` is the sample mean
`z` is the T-table value corresponding to the 95% confidence level.
`s` is the sample standard deviation
`n` is the sample size